Dynamic manipulation of ultra cold atoms using spatially controlled optical potentials

By

Aaron Smith

A thesis submitted to
the University of Birmingham
for the degree of
DOCTOR OF PHILOSOPHY



Cold Atoms Research Group
School of Physics and Astronomy
College of Engineering and Physical Sciences
University of Birmingham
December 2022

UNIVERSITY OF
BIRMINGHAM

University of Birmingham Research Archive

e-theses repository

This unpublished thesis/dissertation is copyright of the author and/or third parties. The intellectual property rights of the author or third parties in respect of this work are as defined by The Copyright Designs and Patents Act 1988 or as modified by any successor legislation.

Any use made of information contained in this thesis/dissertation must be in accordance with that legislation and must be properly acknowledged. Further distribution or reproduction in any format is prohibited without the permission of the copyright holder.

ACKNOWLEDGMENTS

I want to say thank you to my parents, whose support over this 12 year journey of physics has been invaluable. I want to say a special thanks to mum for all the stuffy toys and care packages when I was down, and for tidying up my mess at home, you always manage to give me a laugh. To dad, I say a special thanks for being the steady voice of reason when needed and for being Billy bobs walker for all these years, he very much appreciated it, as did your waist line. I also want to give a special mention to Billy himself, although he is no longer with us, he was my best friend all these years, always bringing a smile to my face when needed, always wagging his tail till the end. And finally, but by no means least I want to say thank you to my partner, Nicole, whose proof reading of this thesis has been invaluable, you have supported me through the process, putting up with all the ups and downs (mostly downs) that come with writing this. So from the bottom of my heart, I say thank you.

From my friends, I think we all know who will be here. Jay and Kal, you are both such important parts of my life, always there when I need a friend and that's simply it. In addition, Matt and Tom, thanks for all the Saturday nights games sessions. You are all important to me.

Finally, the people at work. I think first and foremost I should say thanks to G. You have supported me in many ways over the years. Be it support with personal matters, or with things I was struggling with at work, you have always been a hand to help and someone I can turn to. Even if it was weird British matters you couldn't understand. Secondly, spin up Tom, your contribution to the lab and work we did

together should not be overlooked, always dealing with code that I didn't want to deal with, and always holding the power meter, that's about it right? Finally from the lab we have spin down Tom, I do miss being there, as I know you so miss me. We also have all the people on the cold atoms floor + Stuart - our adopted physicist, thank you for all the pub trips, they help keep this old one sane.

I would like to also have a special mention to the people that have left the group, Jorge and Ellie. Both of you have been great friends and mentors over the time I knew you at work. I miss you both.

LIST OF PUBLICATIONS

FULL PAPERS IN REFEREED JOURNALS

1. Generation of optical potentials for ultracold atoms using a superluminescent diode

   doi: 10.1103/PhysRevResearch.3.033241.

   A.Smith et al. In: Phys. Rev. Research 3 (3 Sept. 2021), p. 033241.

PRE-PUBLISHED PAPERS

2. Bloch Oscillations Along a Synthetic Dimension of Atomic Trap States

   https://doi.org/10.48550/arxiv.2112.10648

   C.Oliver, **A.Smith**, T.Easton, G.Salerno, V.Guarrera, N.Goldman, G.Barontini and H.M.Price. Arxiv (2021).

ABSTRACT

In this thesis I present my work on the manipulation of atomic Bose-Einstein condensates using optical dipole potentials that are shaped and controlled with a digital micromirror device. I provide an overview of the experimental apparatus used, highlighting the components that I have added during my thesis work. In particular, I concentrate on the implementation of a superluminescent diode as a source to create optical potentials. I show that, in comparison to lasers, this kind of diodes deliver higher fidelity and higher quality optical patterns when used in combination with a digital micromirror device. I also demonstrate, for the first time, that the resulting optical potentials can be used to shape and dynamically manipulate ultracold atomic gases. Further exploiting the capabilities of the digital micromirror device, I report on the successful implementation of a long synthetic dimension along harmonic trapped states. I show that by suitably manipulating the atomic cloud with well-controlled spatial and temporal optical potential patterns, it is possible to drive Bloch oscillations along this synthetic dimension. I provide an extensive characterisation of the Bloch oscillations for a range of parameters, including laser power and detuning, and I compare the experimental results with the theoretical predictions.

Contents

1 Introduction **1**

1.0.1 Attractive and repulsive optical potentials: Dipole trap and imprinting . . . 4

1.1 Dynamic potentials . . . 9

1.2 Synthetic dimensions . . . 12

1.2.1 Motivation for the use of Synthetic dimensions . . . 14

2 Experimental apparatus **17**

2.1 Overview of the Basic System and Components . . . 18

2.2 Vacuum system . . . 18

2.3 Laser systems . . . 22

2.3.1 Principles of a magneto optical trap . . . 23

2.3.2 2D and 3D Cooling . . . 24

2.3.3 Dipole trap . . . 27

2.3.4 Evaporative cooling . . . 28

2.3.5 Locking . . . 30

2.4 New optical setup at the science cell . . . 35

2.5 Optical imaging system . . . 40

2.6 Digital micromirror device . . . 41

2.7 Flattened Optical Dipole Trap 42
2.8 Control system 45
2.9 Sequence 46
2.10 Sources of light for atomic manipulation 47
2.10.1 Laser 47
2.10.2 Super-luminescent Diode 49
2.10.3 LED 50
2.10.4 Comparison 50

3 SLD Generated Optical Potentials 53

3.1 The System 54
3.2 Image Characterisation 59
3.2.1 Fidelity and Contrast Analysis 60
3.3 SLD-generated Optical Potentials for Cold Atoms 63
3.3.1 Static Potentials 64
3.3.2 Dynamic Potentials 66

4 Bloch Oscillations 67

4.0.1 Theoretical Overview 68
4.0.2 Experimental Set Up 72
4.1 Experimental Results and Real Space Analysis 72
4.2 Experimental and Theoretical Methods 79
4.2.1 Real-space Experimental Data Analysis 79
4.2.2 Numerical Simulations and Data Analysis 81
4.2.3 Analytical Results 82
4.2.4 Synthetic-dimension Experimental Data Analysis and Theoretical Results 84

4.3 Creation of Highly-excited Harmonic Oscillator States 84

5 Conclusion **91**

List of Figures

1.1 Modulated Potential 16

2.1 Experimental Components 19
2.2 Vacuum System 21
2.3 3D MOT 26
2.4 BECpicture 28
2.5 Dipole Trap Beam Propagation 29
2.6 Laser Box 31
2.7 Rubidium Spectroscopy 32
2.8 Cooling Lock Signal 33
2.9 Locking Electronics 34
2.10 Science Cell 37
2.11 Flat Trap Optics 38
2.12 Imprinting beam path 39
2.13 Close up image of a DMD mirror 42
2.14 Flat trap lenses 44
2.15 Flat trap 45
2.16 Sequence 48
2.17 Laser, SLD and LED graphic comparison 52

3.1 Schematic representation of our optical system, TA gain spectrum and laser/SLD light comparison 55
3.2 SLD and Laser Residuals 56
3.3 Fidelity and Contrast of square wave 58
3.4 Talbot effect 62
3.5 Disordered SLD Potentials 65
3.6 Dynamic potential with the SLD 66

4.1 Potential Schematic, Cloud after driving and experimental oscillations . 70
4.2 Bloch oscillation frequency and real space amplitude as a function of detuning 75
4.3 Varying the shaking power to control the dynamics 77
4.4 Example Bloch oscillation in synthetic space 78
4.5 Bloch oscillation amplitude in synthetic space 80
4.6 Time evolution of the integrated synthetic space density for a thermal cloud 85
4.7 Column density distribution 86
4.8 Cloud density 89

Chapter 1

Introduction

Cold atoms have been used for many applications over the decades [1], developing from the first magneto optically trapped (MOT) atoms [2], to the ultra cold Bose-Einstein condensate (BEC) [3]. The methods of controlling and trapping ultra cold atoms have also changed and developed over time. They have moved on from basic harmonic traps seen in the first experiments to more fluid shape-able traps [4, 5, 6, 7, 8, 9, 10] and even more recently dynamic potentials [11, 12]. In the work carried out for the achievement of the results in this thesis, we use an all optical BEC experiment that is equipped to dynamically manipulate the ultra cold atoms for the purpose of atomic manipulation and quantum simulations using optical potentials. The physics studied encompasses the analysis and comparison of the Superluminescent diode as an alternate light source to the laser to be effectively used for the creation of optical potentials for use in atomic manipulation. Separately the study and implementation of long synthetic dimensions using our ultra cold atom sample was carried out. With further analysis on the properties of Bloch oscillations within this synthetic dimension, confirming the creation of long and controllable synthetic dimension.

Thesis overview

The goal of this thesis is to deliver the results achieved within my research, and to give an overview of the experimental apparatus used the achieve the results. Describing both the pre-existing experimental apparatus, the modifications and additions that have been made. The original goal of the project was to create study the dynamics of solitons within an elongated BEC by using the Digital Micro Mirror Device and a laser light source to imprint a phase shift onto part of the atom cloud. With the goal of moving onto imprinting and studying the dynamics of vortices. It was decided after many attempts that with the current set up, this phase imprinting would not work. So the decision was made to make modifications to the system, by changing the light source used for the phase imprinting from a laser, to a more temporally incoherent light source, as it was suspected that the aberrations in our imprinting image were the cause of the imprinting not creating solitons as expected within the theory and simulations, and a less coherent light source would naturally help with reducing aberrations caused by interference effects. Firstly a LED was tested, however whilst this produced images with no visible optical monochromatic aberrations due to the lights broadband nature, the lack of spatial coherence caused high losses of power in our optical system. This meant that we either needed a much higher power LED to compensate, or an alternate light source that was still temporally incoherent but more spatially coherent. This eventually led us to the 'discovery' of the superluminescent diode, a light source that is spatially coherent but temporally incoherent. In getting this light source and using it within the system, we found that it did produce much clearer patterns imprinted onto the position of that atoms than the laser did, with significantly reduced aberrations. This led to our first technical piece of research that was the comparison of the image quality of these light sources, that finalised with a demonstration of the ability of the SLD to manipulate and hold the atoms within an optical potential.

In addition to this, we carried out a collaboration project in which we implemented the experimental component of the creation of long controllable synthetic dimensions within an ultracold atom system. This is a project working directly with the authors of "Synthetic Dimensions for Cold Atoms from Shaking a Harmonic Trap" [13] in their theoretical work in this paper. The first goal of this project was simply to find an experimental system that worked practically and could create the Bloch oscillations as predicted. After modifications to the original theoretical design, Bloch oscillations were achieved. This was naturally followed by confirming the initial Bloch oscillations, with analysing the system dynamics under different parameters, including laser power and detuning, confirming that the results matched the theory as expected.

Chapter 1 introduces the three fundamental concepts of what is used within the experiment. Describing basic principles of optical potentials and dipole forces, how dynamic potentials are implemented and the options of light source and spatial light modulation techniques. Finally the chapter covers what synthetic dimensions are and how they can be useful, providing motivation for the work.

Chapter 2 gives a complete description of the physical apparatus used within the experiment, starting with the core components, including the Vacuum and laser systems, with a more detailed description on how the laser system is implemented. After this the more specific key components and tools of the experiment are described, including the imaging system, the Digital Micro Mirror device and flat optical dipole trap.

Chapter 3 covers the first experiment carried out, "SLD Generated Optical Potentials", which compares the potentials created by light from a super luminescent

diode and a laser. It starts with a specific overview of the experimental parameters, apparatus and equipment used, in addition to the technical details that were used to carry out the study of the light potentials created. This leads onto the analysis and results achieved in the comparison, including image characterisation techniques used to compare images created by different the light sources. Finishing with the results of using the Superluminescent Diode light to produce static and dynamic optical potentials for use in cold atoms.

Chapter 4 covers the second experiment, "Bloch Oscillations in Synthetic Dimensions Within Ultracold Atoms", which creates Bloch oscillations between the harmonic oscillator states of our atoms sample in an optical trap. the section starts with a theoretical overview of the physics, followed by a brief overview of the experimental setup. After this, the main body of the experimental real space results and analysis is given, followed by real-space and numerical data analysis and finally the results, with the addition of an overview of the creation of highly excited harmonic oscillator states.

Chapter 5 contains the conclusion of both works that were carried out. Summarising what was achieved in both areas of research carried out and where this work can have an impact. Finalising with the directions the experiment is planning to take in the future.

1.0.1 Attractive and repulsive optical potentials: Dipole trap and imprinting

The concept of creating optical potentials is key to many cold atoms experiments, for example, attractive optical potentials are often used to trap atoms in optical tweezers

[14, 15, 16], or to hold and cool atoms at a focused point in a dipole trap [17, 18]. Alternatively, repulsive potentials can be used to create a flat atomic sample by compressing atoms between two repulsive sheets of light [19], or to make a dipole trap, but one where atoms are pushed to an intensity minimum [20], as a couple of examples. The experiment used for the results in this thesis is heavily focused on using both attractive and repulsive light sources to manipulate and cool the atom sample, which will be covered in detail in this thesis. Firstly the physical principles behind the optical dipole force, which is the effect used, will be introduced, followed by how it is used to cool our atoms, and finally how we use it to manipulate them.

The key concept of the optical dipole force is that it's an interaction between an induced dipole moment in an atom and the intensity gradient of a light field. The electric field component from laser light induces an oscillating atomic dipole moment in atoms that are within the light field. The oscillating dipole moment interacts with the electric field causing the atom to experience a change in potential energy. Optical dipole potentials have two main components that we must consider, the interaction potential and the scattering rate. "Optical dipole traps for neutral atoms" [21] has an excellent complete description of these components, however we will focus on the main results from this review paper. We see that the induced dipole moment p in a driving electric field E is given by

$$U_{dip} = -\frac{1}{2}\langle pE \rangle = \frac{1}{2\epsilon_0 c} Re(\alpha) I \tag{1.1}$$

where $\langle pE \rangle$ is the time average, I is the field intensity given by $I = 2\epsilon_0 c|\tilde{E}|^2$, and α is the atomic polarizability. The interesting point of note here, that is of importance in experimental implementation, is that the potential energy is proportional to

the intensity of the light field. Naturally the dipole force is given by the gradient of this potential $F_{dip}(r) = -\nabla U_{dip}(r)$, from this a second important point can be determined that the dipole force is proportional to the intensity gradient of the light field.

To understand the scattering rate we can begin by thinking about it in terms of photon emission and re-emission cycles. Again [21] goes into more detail on page 3, however taking the result of the scattering rate is given by

$$\Gamma_{sc}(r) = \frac{P_{abs}}{\hbar\omega} = \frac{1}{2\hbar\epsilon_0 c} Im(\alpha) I(r) \tag{1.2}$$

where P_{abs} is the power absorbed by our oscillating dipole and ω is our driving frequency. This important result shows that the scattering rate is proportional to the intensity of the light. Looking at both of these effects, we see that whilst higher intensity of light increases the dipole force and potential depth, it also increases the rate that the atoms absorb a photon from the trapping beam, which in the case of cold atoms is enough to destroy the atomic sample due to the energy transferred to the atom. This is not the complete picture though as it doesn't take into account the quantum mechanical effect of saturation of the excited state of the atom. However this can be ignored as in our experiment, as in most other cold atoms experiments when using the dipole force, lasers that are far detuned from resonance are typically used, leading to low saturation, and in our case more physically, low scattering rates. So whilst the increase in intensity of the laser increases the scattering rate, this is offset and controlled by using a laser that is far detuned such that the scattering rate is negligible.

The above expressions provide an initial representation to the main parts of the

optical trapping system. In real experimental systems like ours, multi level atoms are used. In our case, we use alkali atoms of Rubidium 87, because alkali atoms have closed transitions and this species has transitions at a useful optical range near the readily available 780nm wavelength laser. Thus the derivation of the expressions of the dipole potential and scattering rate becomes more complicated once all factors have been taken into account; however, taking the results from [21] we see that for alkali atoms that are used we have

$$U_{dip} = -\frac{\pi c^2 \Gamma}{2\omega_0^3}\left(\frac{2+\mathcal{P}_{g_F m_f}}{\Delta_{2,F}} + \frac{1-\mathcal{P}_{g_F m_f}}{\Delta_{1,F}}\right) I(r) \tag{1.3}$$

for the dipole potential and

$$\Gamma_{sc}(r) = \frac{\pi c^2 \Gamma^2}{2\hbar\omega_0^3}\left(\frac{2}{\Delta_{2,F}^2} + \frac{1}{\Delta_{1,F}^2}\right) I(r) \tag{1.4}$$

for the scattering rate. Where $\mathcal{P} = 0$ or ± 1 for linearly or circularly polarised light respectively, g_F is the Lande factor. Where each term has taken into account the detunigs for both the D1 and D2 transition lines of ^{87}Rb in $\Delta_{1,F}$ and $\Delta_{2,F}$ respectively. Here we see more clearly the above point, that whilst both the dipole potential and scattering rate are proportional to the intensity of the light, the potential scales as $\frac{1}{\Delta}$ whereas the scattering rate scales as $\frac{1}{\Delta^2}$. Thus the counter play between the detuning and the intensity can be seen, and that if a sufficiently detuned laser is used the scattering rate can be kept low and the trapping potential high. In addition to this, the sign of the detuning plays an important role. The detuning can be either positive or negative, if the detuning is positive the potential becomes repulsive. This reverses the effect the light has on the atoms, however this does have uses and is in fact used through the experiment, so is a key feature that is taken advantage of.

Uses of potentials in the experiment

The final stage of cooling that takes the 3D MOT and cools it to a Bose-Einstein condensate uses a dipole trap to carry out forced evaporative cooling using an attractive optical potential created from the 1070nm laser (IPG YLR-20W) and the 1550nm laser (IPG ELR-20W). These are both far red detuned from the transitions of ^{87}Rb, thus photons from this light source cannot be absorbed by the atoms. We have an attractive dipole force acting on the atoms that 'pulls' the atoms towards the highest intensity (deepest potential) part of the laser beam.

All of the above also applies to the atom manipulation applied using our DMD. We use both blue and red detuned sources, depending on what experiment we are running. We can either make repulsive 'barriers' to block the atoms from a certain region using blue detuned light, or we can make attractive 'wells' that the atoms reside in. As an example of each, if stirring the BEC or cutting it half, a blue detuned source would be used to create a stirring beam or a barrier, respectively. However if containing the atoms in a localised region or inside of a moving potential was the goal, or channel them through a specific region, typically used in our experiment is a red detuned laser to contain them in shaped potentials, however in both cases red and blue potentials can be interchanged with a bit of thought on how to apply them.

When using high quality sources of lasers, the wavelength is often very controllable to within a narrow range ($<$0.1nm), with a linewidth of the order of 10kHz. Thus, the detuning of the laser can be precisely chosen. When using our SLD source however, we have to deal with a 3dB bandwidth of 20nm. This can cause problems if any parts of this spectrum overlap with transitions, especially if a small frequency detuning to a transition is desired to increase the potential depth. However this does not hinder

the SLDs ability to produce red or blue detuned potentials significantly, making them a viable source for the production of potentials.

1.1 Dynamic potentials for use in atomic manipulations and quantum simulations

The introductory material in this section includes parts that have been published in the paper: A. Smith, T. Easton, V. Guarrera, and G. Barontini. "Generation of optical potentials for ultracold atoms using a superluminescent diode", which was published in Physical Review Research. Some of this material remains largely unchanged, others has been made more appropriate for the thesis.

Spatial light modulation is widely used in photonics as it allows for precise manipulation of light to form static or dynamic patterns [22, 23, 24, 25, 26, 27, 28, 29]. Whilst the work in this thesis uses a Digital Micro Mirror device (DMD), other light shaping technologies exist, such as liquid crystal spatial light modulators (LC-SLMs), ferroelectric liquid crystal modulators and deformable mirrors. All of these may have pros and cons over the others in the creation in various applications. In [30] we see a comparison of the fidelity of potentials created by a DMD and LC-SLM, which are two common configurable light modulators. This highlights a desire in the community to achieve high fidelity in the patterns/potentials created for applications in photonics. In our case, a DMD is chosen because of the high modulation rate that is achievable by this tool. This is desirable for creating fast dynamic potentials for use in quantum simulations. In [30] it is also highlighted that the DMD can create higher fidelity shaping of light than a LC-SLM. The biggest drawback for the use of the LC-SLMs for our use and one of its main overall drawbacks is the low modulations speed, which

is typically in the range of 10-200Hz. Whereas the DMD used in our experiment has a modulation rate of 10KHz, which is more appropriate for the creation of dynamic potentials for use in atomic physics and quantum simulations.

Quantum simulations with cold atoms is one of the most productive areas in quantum technology, and has provided us with important insight in condensed matter physics [31, 32], the physics of disordered systems including the observation of Anderson localisation [33, 34], low dimensional systems [35], the use of synthetic fields [36] and dimensions [37], high energy physics including Higgs modes [38] and black holes [39], topological effects [40] and many more. The main feature of quantum simulators based on cold atoms is the exquisite control that is nowadays possible to achieve on these systems, either by engineering the atomic internal states or by producing potentials to alter the shape, position, temperature and momentum of the samples [41]. This has been largely enabled by the rapid development of laser technology, that provides light with the ideal combination of high spatial and temporal coherence, high intensity and narrow line width. Such a combination allows one to precisely address atomic transitions with one or more photons, implement atoms traps with a large variety of shapes, produce optical lattices and dynamical potentials, and even address and manipulate single atoms [42, 43].

Lately, laser light combined with spatial light modulators is also emerging as a new avenue for the production of arbitrary and even time varying potentials [44, 45, 46, 47], including non-trivial phase engineering of Bose-Einstein condensates [48] and applications in atomtronics [49, 50]. While the coherence of laser light is a key feature for the vast majority of the applications discussed, it could represent a hindrance in the generation of complex patterns using digital micromirror devices (DMDs). In

these kinds of systems, the pattern produced on the DMD is imaged on the atoms and interference effects caused by the large temporal coherence can cause aberrations in the image. To mitigate this, one could use very complex and expensive optical systems or implement a feedback loop [51], modifying the pattern in real time on the DMD so as to minimise the difference between the projected image and the desired one.

The methods described above attempt to mitigate the detrimental effects of temporal coherence. An alternative approach is to eradicate the problem by using light sources with reduced coherence properties. Since high spectral specifications are not required to produce optical potentials, as long as the whole spectrum of the source is far detuned, one could choose to use incoherent light sources such as LEDs to obtain pristine patterns. The main issue in this case is that the absence of spatial coherence makes it very difficult to reach intensities that allow one to produce sufficiently high optical potentials to manipulate the atomic samples. In section 3 of this thesis, this problem is addressed by using super luminescent diodes (SLDs) in combination with a DMD to produce optical potentials with significantly reduced aberrations. A SLD is similar to a standard laser diode, except that it strongly suppresses feedback through a combination of a tilted waveguide and anti-reflection coatings applied to the facets. This lack of feedback means that lasing is not achieved and instead the diode performs amplified spontaneous emission, with a spectrum that is not narrowed by the effects of a cavity. SLDs are therefore temporally incoherent [52, 53] but feature high spatial coherence [54]. It is later shown that the low temporal coherence of SLDs allows us to produce images with significantly reduced interference effects compared to a laser. At the same time, due to its high spatial coherence, the device is capable of producing sufficiently high intensities in a well behaved Gaussian beam shape, allowing us to manipulate ultra cold atomic clouds with arbitrary patterns.

1.2 Synthetic dimensions

The introductory material in this section includes parts that have been published in the paper: C. Oliver, A. Smith, T. Easton, G. Salerno, V. Guarrera, N. Goldman, G. Barontini and H. M. Price "Bloch Oscillations Along a Synthetic Dimension of Atomic Trap States". This has been submitted for publication in physical review X. Some of this material remains largely unchanged, others has been made more appropriate for the thesis.

In physics it is common practice to use systems of higher dimensionality to simulate systems of lower dimensionality. For example even with simulations in BEC systems it is common to create an effective 1D or 2D sample of atoms to simulate dynamics of 1D or 2D in a 3D system [48, 55]. However it can be harder to visualise simulating a higher dimensional system within a lower dimensional system, as the extra dimension would not be a real spatial dimension. This is where synthetic dimensions come in. Synthetic dimensions are in essence a method of studying a higher dimensional system by using a lower dimensional set-up, in effect enabling a lower dimensional set-up to effectively simulate the behaviour of a higher dimensional system. The first step in this is to identify a set of uncoupled degrees of freedom in within the system and reinterpret these as lattice sites along an extra spatial dimension. We then add in effects from an external coupling between these uncoupled degrees of freedom that for example allows the particle being looked at to hop along the lattice sites in this extra dimension. This is often applied to atomic systems, exploiting internal degrees of freedom of an atom as the extra spatial dimension.

Firstly, I will explain what is meant by a synthetic dimension in our case. Simply put, we have reinterpreted an external degree of freedom of our atomic ensemble as an extra dimension. In this case we use discrete states of the atoms within the harmonic trap potential, these are re-labelled as lattice sites along the synthetic dimension. The states are externally manipulated and coupled, causing the atoms to hop between states and move along this extra dimension. In more physical terms, the atoms occupy a different harmonic oscillator state. In the work within this thesis we control the motion of these states by applying an intensity modulated potential that varies in time. In this approach, the standard 1D harmonic oscillator states serve as lattice sites in the synthetic dimension, with a weakly anisotropic 'hopping'. This could provide the framework to create very long synthetic dimension, limited only by the anharmonicity of the trap.

One important thing to note is difference between real and synthetic dimensions in the context of condensed matter physics, is the difference in inter-particle interactions. In materials, atoms that are spatially-close to one another interact stronger than those that are far apart, which means the inter-particle interaction has some degree of locality. Conversely, in many implementations of synthetic dimensions, particles that are far apart in the synthetic dimension interact as strongly as those that are close together. This is because particles that are far apart in synthetic space are still nearby in real space, and so can still strongly interact.

1.2.1 Motivation for the use of Synthetic dimensions

Synthetic dimensions are opening up many new avenues for simulating and exploring exotic physics, including quantum Hall ladders [56], [57], [58], non-Hermitian topological bands [59], topological Anderson insulators [60], and even lattice physics in four dimensions or higher [61, 62, 63]. A key reason that the framework of synthetic dimensions is so powerful is that it is very general, and can be applied and used in a wide range of very different physical systems. For example, synthetic dimensions have so far been realised experimentally in cold atoms with hyperfine [62, 56, 57], magnetic [64], Rydberg [65, 66], and clock states [67, 68], as well as with momentum [58, 61], orbital [69] and superradiant states [70]. However, in these experiments, the size of the synthetic dimension has been so far limited by the number of states that can feasibly be coupled.

Notably, it has been recently realised that such limitations can be lifted if external degrees of freedom associated with trapping potentials are used to generate the synthetic dimensions [13, 71, 72]. Indeed, trapping potentials typically allow for tens or hundreds of trapped states in each direction, and by suitably coupling them one could implement very 'long' synthetic dimensions that access these high numbers of trapped states, unleashing the full potential of this technique. Additionally, this kind of synthetic dimension is extremely appealing because it provides an intuitive framework for how to manipulate and control trap states. A range of applications including quantum simulations in optical lattices [73, 74, 75], trapped and guided atom interferometry [76, 77, 78] and quantum thermodynamics [79, 80, 81] require the use of highly excited trapped states, which are generally difficult to realise with a good degree of precision and control.

In the work shown in chapter 4, we experimentally engineer a very long synthetic dimension of many tens of atomic trap states by dynamically modulating the harmonic trap of an ultracold atomic sample using a DMD [13, 71], seen in figure 1.1. By controlling the driving frequency we generate a force along the synthetic dimension that induces Bloch oscillations. Such oscillations were first famously predicted for electrons moving in a crystal under an electric field, and have since been observed in various setups, including optical lattices for cold atoms [82], as well as synthetic dimensions of photonic frequency modes [83] and of room-temperate molecular angular momentum states [84]. However, Bloch oscillations in our experiment are physically very different from previous realizations, as they correspond to atoms periodically oscillating between low and high energy states of the harmonic trap. As we show, the synthetic dimension Bloch oscillations implemented here allow us to explore highly excited harmonic states, and thus can lead towards a novel approach for quantum engineering of external atomic states. This work paves the way for the exploration of higher dimensional quantum Hall physics with artificial magnetic fields, and opens new opportunities in quantum simulations and quantum control.

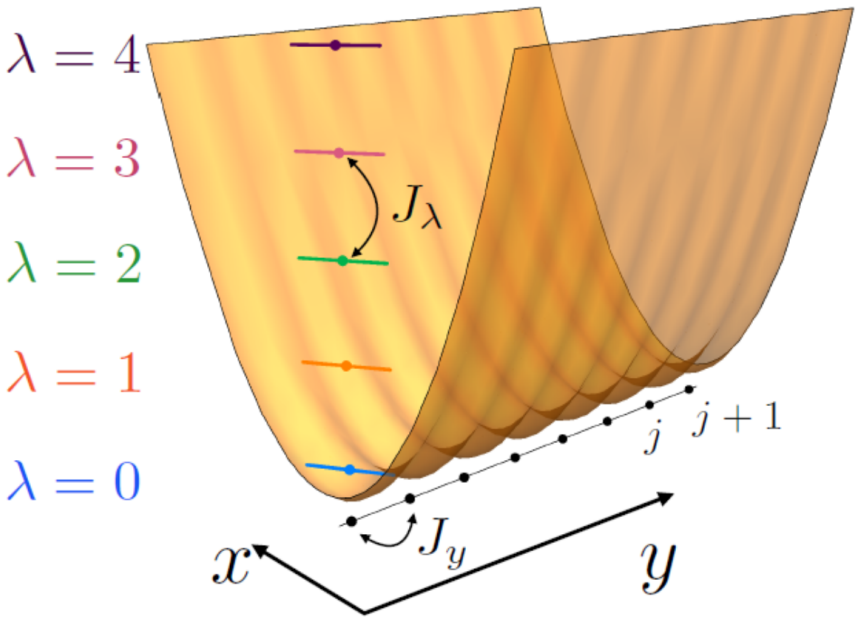


Figure 1.1: **Modulated harmonic potential.** Representation of the harmonic potential that undergoes potential depth modulation where we have also indicated the idea between the quantised harmonic oscillator states (lambda states, λ), where $\lambda = 0$ is the ground state, $\lambda = 1$ is the first excited state, etc. J_λ denotes the hopping amplitude between excited states, J_y denotes the hopping amplitude between lattice sites, j denotes the 'lattice' site location, and x and y the horizontal plane.

Chapter 2

Experimental apparatus

In this chapter the experimental setup on and off the table will be described, starting with a basic overview of what the experiment does. Next the core components of the experiment, starting with the vacuum system and how the lasers work in conjunction with this vacuum system to achieve cold atoms are covered. This encompasses describing the physical components used in the creation of a 2D MOT, 3D MOT and the BEC we finally produce in our dipole traps, as well as how the lasers are locked to set frequencies so they are at/near the correct transitions. Following this, the optics around the science cell and components that control and manipulate the atoms is described. This includes the optics for the main dipole trap used for the creation of our BEC, the optics for the imaging system, the DMD light projection system and the flat trap. Following this, the system that controls the timings and powers of all equipment in the experiment will be briefly covered, along with the sequence that is used day to day to produce our BEC samples. Finally this chapter ends with a technical comparison of the difference sources of light used for atomic manipulation. Covering Lasers, SLDs and LEDs, and how they are incorporated into our experiment and effect the atoms.

2.1 Overview of the Basic System and Components

This section will give brief description of the apparatus used in the experiment. Ranging from the control software and hardware used to run the experiment, to the physical system on the optical bench. The experiment used in the work throughout this thesis is an all optical Cold atoms experiment which produces a BEC of 87Rb atoms. Key components of this experiment, as in any all optical BEC apparatus are the 2D and 3D magneto optical traps and an optical dipole trap. These are seen and described in the following sections of this chapter. The features that makes this experiment more unique compared to many other cold atoms experiments are the digital micro-mirror device, which allows us to interact with the BEC using dynamic or static optical potentials, and the microscope objectives used to focus imaging light and optical potentials onto the Rubidium Bose-Einstein condensate. Both of these components are key to the research, allowing precise, high resolution manipulation of atomic samples. In figure 2.1, we see a schematic diagram of the main components of the experiment and how they interact with one another. Within the vacuum system are the Rb atoms and the laser light for the cooling and trapping of the atoms (the optics are outside of the vacuum system). The control system interacts with and controls all parts of the experiment that receive the sequence of electric signals while cold atoms are being produced. Also shown is how the imaging and DMD systems directly interact with the atoms, cooling and trapping lasers.

2.2 Vacuum system

Since the energy scale of cold atoms is at a very low level, the experiment requires the use of a vacuum system. The experiment produces an atom sample as low as 20nK, whereas the temperature of air is about 300K, which means that any interac-

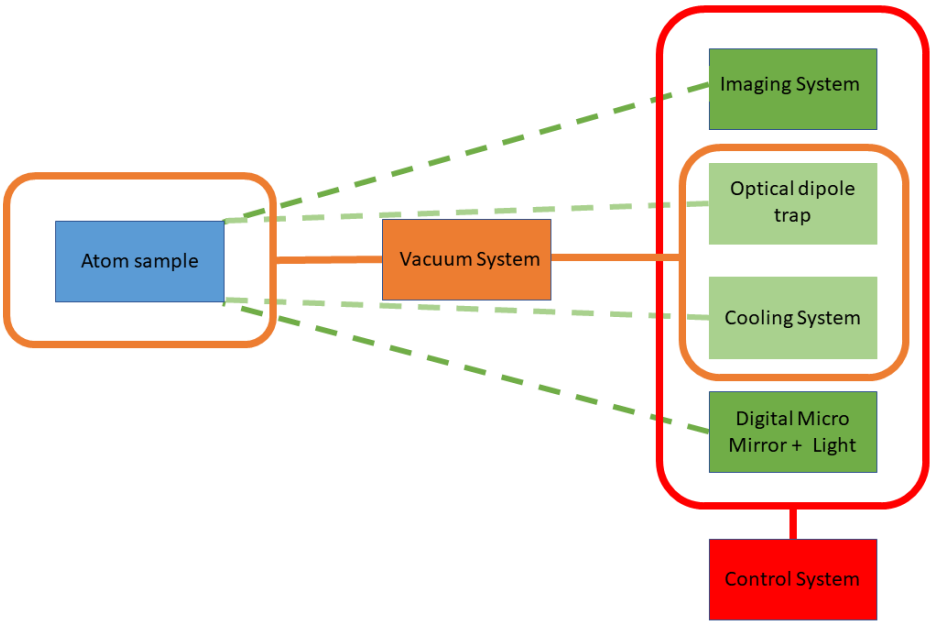


Figure 2.1: **Outline of the main components of the experiment and how and where they interact.** In red we have the control system which controls the atom cooling and trapping (in light green) and the atom probing and manipulation (in green). We also have the vacuum system (orange) which is passively kept at a stable vacuum, within this is where the atom sample (blue) is formed from the cooling and trapping systems.

tion between an air particle and one of the cold atoms in the system would destroy the system by transferring unwanted energy through collisions to the rubidium atoms causing the cold atoms to stop being produced. To achieve this low energy regime with a low chance of these destructive collisions, an ultra high vacuum of approximately 10^{-10}mbar in the science chamber is used. The 2D MOT chamber has a vapour pressure of approximately 10^{-7}mbar, which is higher than in the science chamber due to the presence of the rubidium vapour that is needed to achieve sufficiently good loading into the 2D MOT. The chamber is separated from the science cell by a differential pumping stage, which consists of a hole that is 1.1mm in diameter and 2.1mm in length. This differential pumping stage allows the 2D MOT chamber and the science cell to keep a difference in pressure of three orders of magnitude with the use of the ion pump, whilst allowing us to transfer the atoms from one chamber to another with a push beam.

The 2D MOT chamber is composed of titanium and is rectangular. It has $4.8cm \times 2.5cm$ ovular windows on the sides to allow the wide 2D MOT beam to pass through and then to retro reflect back from a mirror with a quarter waveplate on the face of it. The horizontal and vertical axis in the 2D MOT both have a beam and mirror pair. There is a window on the back end of the chamber to allow optical access of the push beam that pushes the atoms down the length of the vacuum system from the 2D MOT to the 3D MOT and through the differential pumping stage which is at the opposite end of the titanium chamber to the back window. A picture of this can be seen in figure 2.2.

The titanium chamber is connected to a 30cm long glass tube with a rectangular science cell at the end, that has external dimensions $10cm \times 2.5cm \times 2.5cm$. The center of the science cell is where the 3D MOT beams and dipole trap beams intersect, thus the cell is coated in anti reflection coatings to minimise reflections of the 780nm and

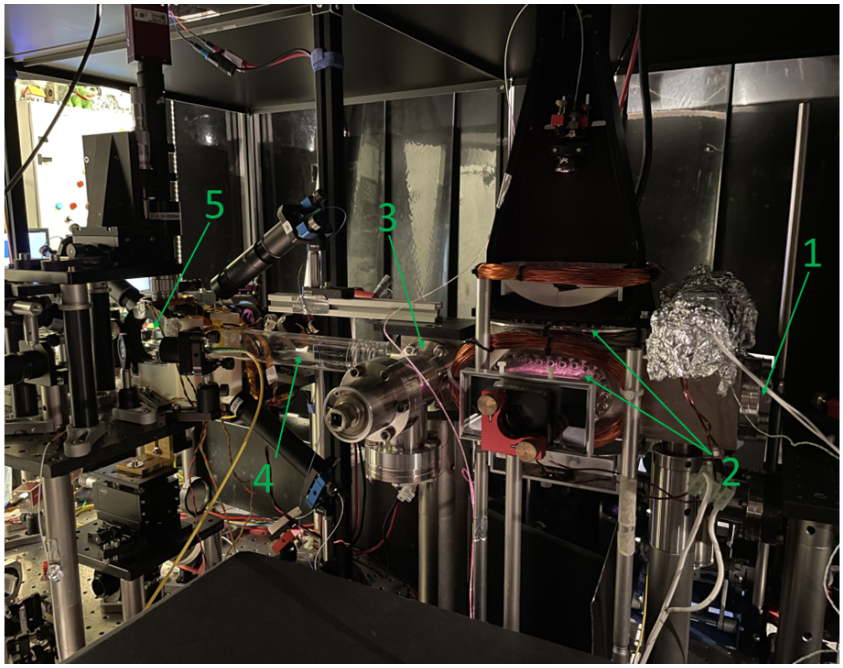


Figure 2.2: **Image of the Vacuum system with surrounding components.** 1) Window at the back of the chamber that is used for access of the push beam. 2) Windows in the Vacuum system that allows access of the 2D MOT beams, one of which can be seen to have its output fibre above the top window. 3) The connection between the glass cell and the titanium chamber, also where the ion pump and differential pumping stage is. 4) Glass cell that connects the 2D MOT chamber to the science cell. 5) Science cell, surrounded by optics for the 3D MOT, imaging system, and dipole traps.

1550nm light, the cell is not coated for 1070nm light however losses are minimal and power here is not an issue. As mentioned before, this is where the BEC is formed, so the pressure in this part of the vacuum system is approximately 10^{-10}mbar.

2.3 Laser systems: The stages of cooling, trapping, shaping and laser locking

After all stages of cooling, the experiment produces a BEC in which we maximise condensate fraction and atom number whilst shaping to the desired shape. To produce the BEC, different cooling stages are needed. The first stages of cooling we have are the 2D then the 3D MOTs, from which atoms are transferred from the 3D MOT into the optical dipole trap, upon which evaporative cooling takes place. This process can be seen and is summarised in [85], the thesis of the original builder of the experiment. The research we undertake relies upon the shape of the properties of the BEC. Each project we undertake generally requires a different shape, size and condensate fraction/temperature of the BEC. These parameters can be controlled in different ways. The temperature/condensate fraction is dominantly controlled by the final potential given by the dipole trap. The trap depth and temperature of the atoms can be raised by ending the evaporation ramp at higher powers, subsequently evaporating fewer atoms. The shape of the trap can be altered by changing the end ratio of the powers of the dipole trap beams. An elongated BEC can be created by having one beam contribute much more dominantly to the potential depth than the other, or a more circular condensate by having each beam give more equal contribution to the trap potential depth. The shape of our trap is also controlled by the focal width of the lasers, with narrower laser widths causing tighter trapping and deeper potentials with the same laser power. In our system we use a 1550nm laser with a focal width of 50μm and a 1070nm laser

with a focal width of 35μm. All of these systems will be described in the following sections. Starting with first two stages of cooling, the 2D and 3D cooling, followed by the dipole trap system that is used to create ultra cold atom from the 3D MOT sample.

2.3.1 Principles of a magneto optical trap

Magneto optical traps use the principle of laser cooling to cool down atoms to the order of 100s of microkelvin. Laser cooling uses specifically selected internal atomic transitions as a means to allow for the absorption of a photon. For this we will say that the transition is between the ground state of an atom and an excited state. However this only works when the light is tuned to be slightly off resonance with this transition to allow for the doppler shift that the atoms see in the frequency of the light they are traveling towards. An incoming photon can only be absorbed when its energy matches that of the transition and interacts with the atom, raising the atoms from ground state to this excited state. Photons carry energy $\hbar\omega$ and momentum $\hbar k$, thus when the photon is absorbed by an atom, that momentum is transferred to the atom. The light is red detuned in such a way that only atoms that are travelling towards the light source absorb the light. When an atom is in its excited state, there is a probability it will decay back into its ground state within a certain time. Decay causes a photon that matches the energy of the incoming photon to be emitted, but in a random direction. This imparts momentum back to the atoms but again, in a random direction (opposite to that of the re-emitted photon). Over many absorption and re-emission events this randomness cancels out and we have a net slowing force. If this system is implemented, but with 3 pairs of counter propagating beams, covering all 3 spatial dimensions then atoms will be slowed (cooled) in all directions. This is only part of whats needed, the atoms also need to be trapped at the crossing point of these beams. To trap the atoms

at the intersection, coils are used in the anti-helmholtz configuration. This produces a position dependent shift in the zeeman energy levels of the atoms due to the linear zeeman effect that in combination with the chosen polarisation of light, creates an effective force that acts towards the centre of the trap due to radiation pressure. The force/radiation pressure is stronger for the atoms furthest from the centre of the trap (the faster the atoms), due to an increased probability of absorption of a photon at larger radial distances from the centre of the trap.

2.3.2 2D and 3D Cooling

The first stage of cooling is the 2D MOT. The primary function of the 2D MOT is to increase the loading speed and the number of atoms that are loaded into the 3D MOT by providing the 3D MOT with an increased rate of cooler atoms to be trapped. In the 2D MOT system we have one MOT laser in the horizontal axis and one in the vertical axis, which are both similarly circularly polarised directly out of the fibre. The laser passes through the chamber and retro reflects off of a mirror that has a quarter wave-plate in front of it, back through the glass windows and through the 2D MOT vacuum chamber again. These horizontal and vertical beams are a mixture of two lasers. One is set to the cooling transition and one to the repumper transition. The repumper uses 20mW of power and the cooling uses 40mW of power, in each axis. This chamber has a set of anti-helmholtz coils, with one coil around the top and one around the bottom of the chamber that creates a quadrupole field centered at the center of the chamber and along the symmetry axis (length) of the chamber. This field has a gradient of 10G/cm at the centre of the chamber whilst running 5A of current. The mixture of the light, fields and rubidium vapour leads to the creation of a 2D MOT from which there is minimal confinement in the third axis (down the length of the chamber). This allows cooled/cold atoms to be pushed by our push beam into the next science cell. The push

beam is a 350uW beam that is linearly polarised. It is taken from the output beam of the cooling tapered amplifier (TA), shifted by 160MHz using an AOM in double pass configuration, taking the first order beam, and fibre coupled such that the output is at the back window of the vacuum chamber. The beam is split before this coupling and is used for the absorption imaging. Using this 2D MOT in combination with the push beam, the 3D MOT reaches saturation in our system in approximately 5s, with an atom transfer rate from the 2D MOT to the 3D MOT of $\sim 10^9$atoms s^{-1}.

These atoms are then recaptured by the 3D MOT which operates under the same principles as the 2D MOT except in 3 spatial dimensions achieving complete confinement in all axis; therefore, creating a MOT confined in all directions. This allows for complete cooling achieving the creation of the 3D MOT, which is achieved by using 3 pairs of 1 inch wide collimated counter propagating beams of circularly polarised light, the polarisation of the beams along the direction of the magnetic coil axis is opposite compared to the polarisation of the beams in the orthogonal plane, it will be sigma + in magnetic coil axis, and sigma – in the orthogonal axis. The horizontal beam pair used 3mW of cooling power and 2mW of repumper power and the vertical beams are both 7mW cooling beam. Each pair is at right angles to one another: two pairs are 45 degrees off the horizontal plane, and the other is in the horizontal plane. These MOT beams are in combination with another anti-Helmholtz coil, which is 50 turns of copper wire, wound to have two 6.5cm diameter coils, 5cm apart from one another, creating a field of 10G/cm whilst running at 2.3A of current. In this case with the coils oriented vertically round the sides of the chamber, but rotated about the symmetry axis, same as the 2D MOT coils. In addition to these vertically oriented coils, we have a second pair of coils, in Helmholtz configuration in order to compensate for vertical background magnetic fields (earths magnetic field). This field has a strength of 3.83G/A at the

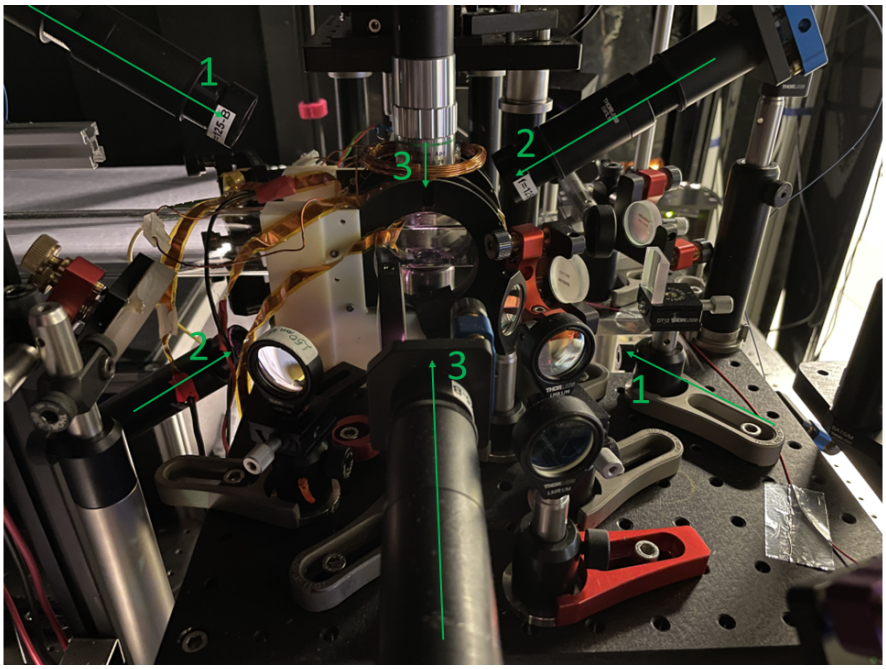


Figure 2.3: **Image of the 3D MOT system and coils around the science cell.** Marked as 1 and 2 are the vertical MOT beams, and Marked as 3 are the horizontal MOT beams. All 3 pairs are pointing to the center of the glass cell which is in between the anti-helmholtz coils.

centre of the cell. The final product of this stage of cooling is a MOT of temperature $\sim 350\mu$K, $\sim 10^{-9}$ atoms and a phase space density of 7×10^{-8}. A picture of this set up can bee seen in figure 2.3.

One major intentional difference between the 2D MOT and the 3D MOT systems is the construction of the vacuum system in each. It is seen that the 2D MOT is formed using a large titanium chamber with glass windows for the beams to pass through, and the 3D MOT is in a glass cell. This allows easier access to the atom sample in the 3D MOT, allowing us to probe the atoms from a closer distance and allowing more free positioning of beams, such as the imaging microscope objectives and the dipole trap beams.

2.3.3 Dipole trap

The third main cooling component is the crossed dipole trap. The dipole trap consists of two lasers far detuned from resonance. Both lasers use different wavelengths to avoid interference between them. To not cause any heating effects in the atom sample, the lasers are far detuned from the atomic transitions of ^{87}Rb. One laser is at 1550nm and the other is at 1070nm. These two lasers are focused and crossed at the center position of the MOT, which is roughly in the center of the cell. There is a 35 degree angle between the dipole lasers making the trap is only symmetric about two axis. The lasers follow the optical path as shown in figure 2.5. Here we see that both lasers are focused by a 15cm lens that cross at the center point of the MOT. Each laser has a final beam waist of 35μm for the 1070nm laser and 50μm for the 1550nm laser at the crossing point.

The atoms are loaded into this dipole trap stage from the 3D MOT by first undergoing a dark MOT stage that transfers $\sim 10^8$ atoms into the ground state. This increases the number of atoms loaded into the trap due to an increase in phase space density (PSD) from 7×10^{-8} to 3×10^{-6}, and a decrease in temperature from 350μK to 50μK. Once loaded, the atoms undergo forced evaporation in the dipole trap, from a potential depth of 556μK to a potential depth of 404nK, by exponentially ramping down the power of the dipole trap beams over a period of 8s. The atoms are first loaded into the 1070nm beam which has a power of 12.4W. Evaporation begins after atoms are loaded into the dipole beam. The 1550nm beam is turned on after the 1070nm beam has been ramped down in power and the max potential depth created by the 1550 is approximately equivalent to that of the 1070 (approximately 5s before the end of evaporation) to help continue the cooling and shape the trap, this can be seen in more detail section 2.9. The final product is a BEC of Thomas-Fermi radi $R_{tfx} = 9.9 \times 10^{-6}$m $R_{tfy} = 8.4 \times 10^{-6}$m $R_{tfz} = 35 \times 10^{-6}$m. The final tapping beam powers are 45mW

in the 1550nm laser and 100mW in the 1070nm laser, with trap frequencies of 115Hz, 135Hz, 33Hz and 2×10^5 atoms. A picture of our final condensate can be seen in figure 2.4, from both the horizontal and vertical axis.

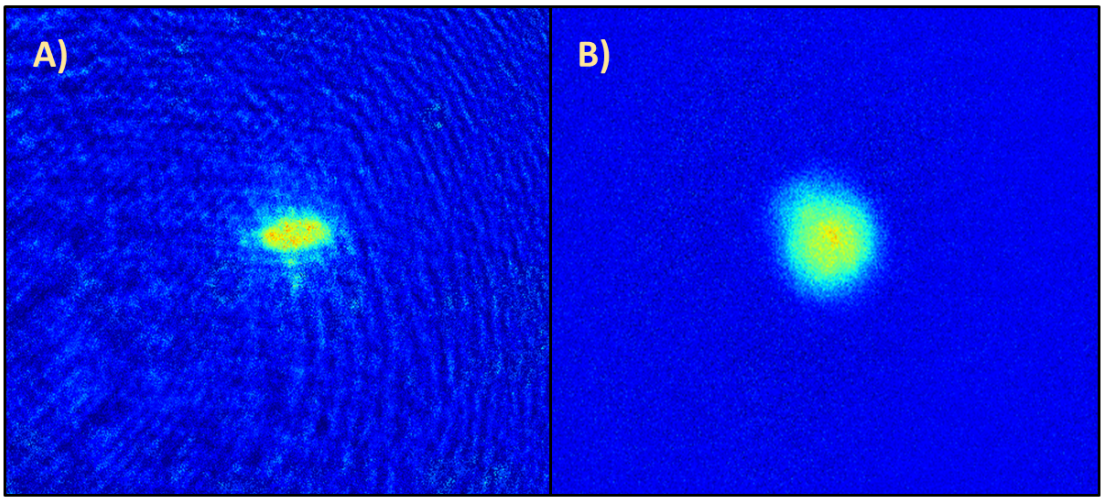


Figure 2.4: **Images of our BEC.** A) Image from the vertical axis with a magnification of 20×. B) Image from the horizontal axis with a magnification of 2.7×.

2.3.4 Evaporative cooling

In the experiment, to reach the BEC we use our crossed dipole trap to evaporatively cool the atoms that are transferred into the dipole potential from the 3D MOT. As part of the loading of the dipole trap, the 3D MOT first undergoes a dark MOT stage where the repumper beam is turned off, meaning the atoms stop being pumped back to the excited state and naturally fall to the ground state. This is done quickly, shrinking and cooling the cloud for more efficient loading of the dipole trap. Evaporative cooling is conceptually simple as it is something we see in everyday life. For example a cup of tea cooling whilst being left alone. It's the process of the hottest atoms leaving the

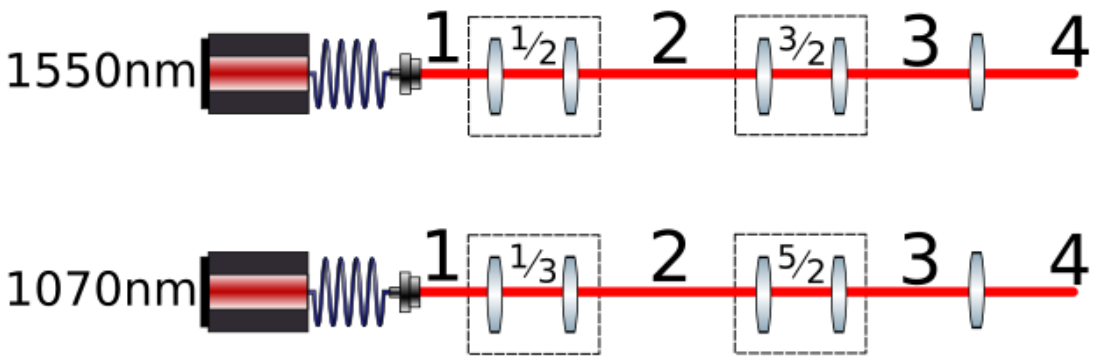


Figure 2.5: **Main cooling dipole trap beam paths.** For the 1550 at positions 1-4 we have beam waists respectively of 4mm, 2mm, 3mm and 50μm at the focus. For the 1070 we have waists of 2.58mm, 0.86mm, 1.95mm and a focal waist of 35μm, again respectively. Where the dashed boxes show the ratios of the telescopes used to control the beam waist

object that is cooling, leaving the remaining substance cooler over all. In this case this is forced with the dipole trap. The atoms are in an attractive red detuned dipole trap potential and the hot tail of atoms is removed from the sample by slowly lowering the power of our laser (and thus the potential depth). As the potential depth reduces the hotter atoms can escape. This process has to be done slow enough so the remaining atoms can re thermalise, repopulating the higher energy tail, thus maintaining the equilibrium of the sample. If the sample is not allowed to re equilibrate, the high energy tail of atoms wont continuously be produced, which consists of a comparatively small number of atoms, minimizing losses during evaporation. If it evaporates too quickly, a larger portion off the distribution of energies we will be evaporated as the sequence progresses, leaving us with no atoms by the end of the evaporation sequence. The evaporation sequence used in our experiment is described in section 2.9 and can be seen in fig 2.16.

2.3.5 Locking

The locking system that is currently implemented is a two laser dither lock that modulates the voltage to a piezo-transducer in the external cavity diode lasers, thus allowing the frequency to be scanned. This two laser lock replaced the three laser dither locking system in the original experimental setup [85]. The new system has the benefit of being more simple in design in comparison to the the old one, however it is also more restricted in terms of tunability. The system is comprised of 2 frequency scanning cavity lasers. One that provides laser light for the rempumer transition and one laser for the cooling transition, both of these lasers are seen in figure 2.6. The repumper laser has a small amount of its power directed into the spectroscopy setup for use in the absorption spectrum of our rubidium 85 and 87 sample. The expected spectroscopy and actual spectroscopy from the experiment are shown in figure 2.7$A\&B$ respectively. The system allows us to see the absorption spectrum created by the D2 line of Rubidium 87 which corresponds to the 1st and 4th major peaks in the frequency scanned absorption spectroscopy signal of our sample. For the repumper we look at the 4th peak within which we choose the hyperfine peak that corresponds to the remumper transition of F=1 $\rightarrow$ F'=2, which is also shown in figure 2.7c, circled at the peak.

The locking system fixes the frequency of this laser at this transition by providing feedback to the laser controller. To get the lock for the cooling the system uses the repumper laser that's now fixed at the repumper transition and mixes it with a second frequency scanning cavity laser to create a beat note. This is detected by a photodiode that picks up the frequencies of the beat note that correspond to both the difference and the sum of the frequencies between the two lasers. It is known that the cooling transition is 6.8GHz away from the repumper transition, so the aim of the lock is to set the frequency difference between the two lasers to be such that the overall difference,

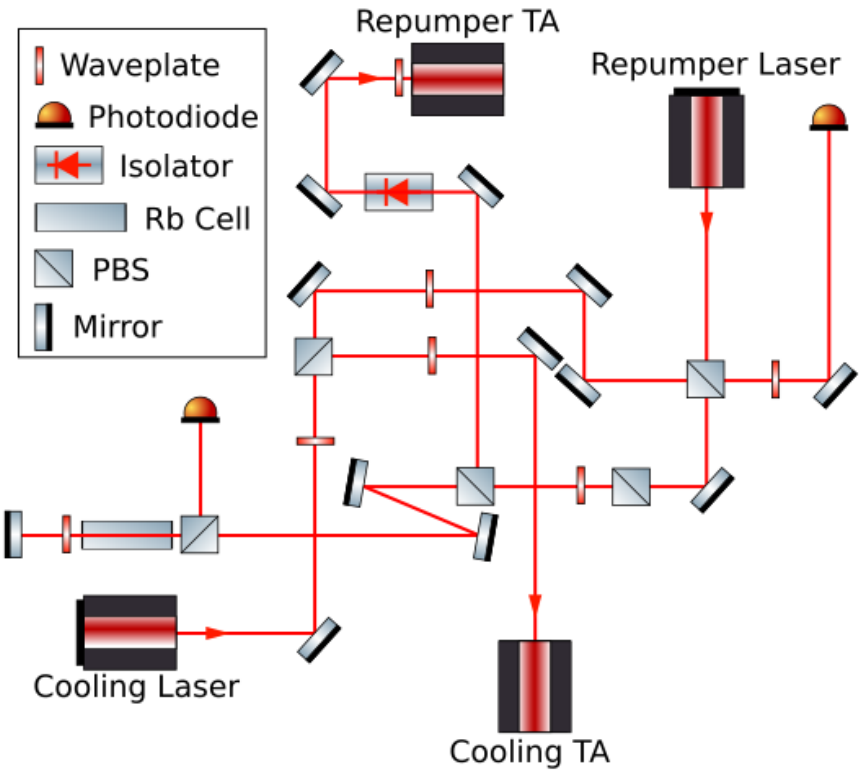


Figure 2.6: **Diagram showing the optical layout of the box housing the repumper and cooling lasers, plus the laser locking and amplifying systems.** This box houses 2 lasers and 2 tapered amplifiers, one for the cooling light, and 1 for the repumper light. The amplified light from each of the amplifiers is passed through AOMS before being injected into fibres that take light to other parts of the experiment.

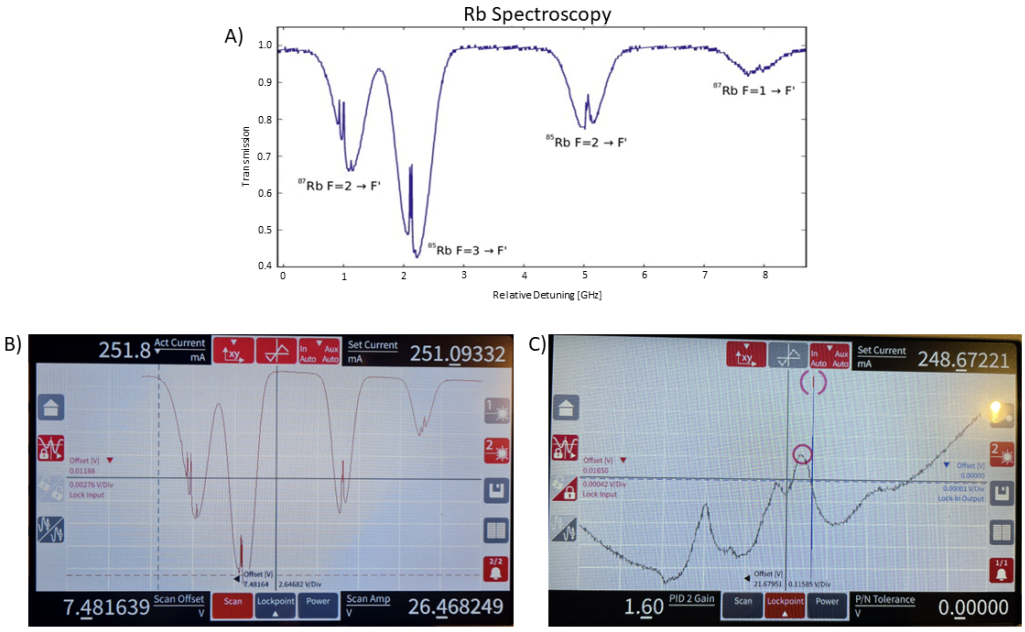


Figure 2.7: **Rubidium spectroscopy signals.** A) Expected signal, showing which transition is which within the spectrum. [86] B) Experimental absorption spectrum c) Position we lock the repumper laser to in the 4th peak

taking into account shifts in frequency caused by subsequent AOMs in the system, is 6.8GHz. The locking works by taking the signal of the beat note from the photo-diode and mixes it with a second signal with a set frequency. The combined signal then passes through a low pass filter, to allow only the signal that is the difference between the beat note difference an the second signal to pass through. This combined and filtered signal then goes into our error signal circuit board which splits it into two branches, a fixed attenuation in one branch that converts to a DC signal and high pass filter that creates a frequency dependent attenuation that is again DC and of opposite sign. The combined signal is fed into the lock box and shows a signal with a trace shown in figure2.8 (changing amplitude of voltage as a function of frequency). This locking system has been chosen such that when the lock is locked on the slope at the zero crossing point (the point where the board outputs no voltage cause both arms cancel

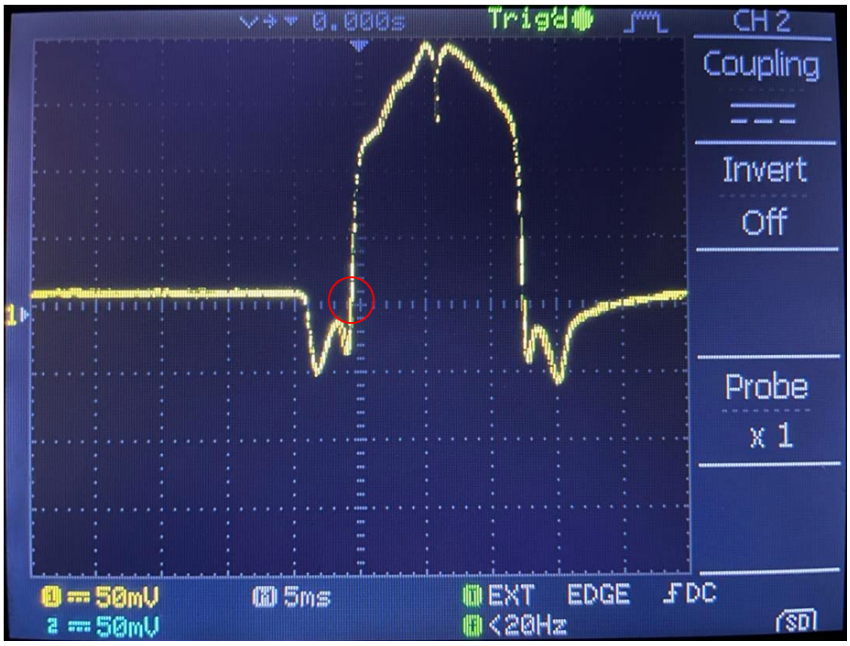


Figure 2.8: **Cooling lock signal.** Error signal used for the locking of the cooling laser frequency, where the lock point is shown by the red ring.

out) the frequency of the locked laser is at the cooling transition, taking into account all other components.

This system gives us lasers at two different frequencies: One that is locked to the repumper at a fixed non-tuneable frequency, and one laser that is locked to the cooling frequency but can be tuned by altering the mixed frequency supplied by the synthesizer. This tunability is needed in the experimental sequence where we need change the frequency of the cooling laser from and back to resonance during the cooling process, dark MOT and imaging stages. A diagram of the locking electronics setup is given in figure 2.9

After the lasers have been locked to the correct frequencies they need to be amplified to an appropriately useful power because the lasers used are not of sufficient power for

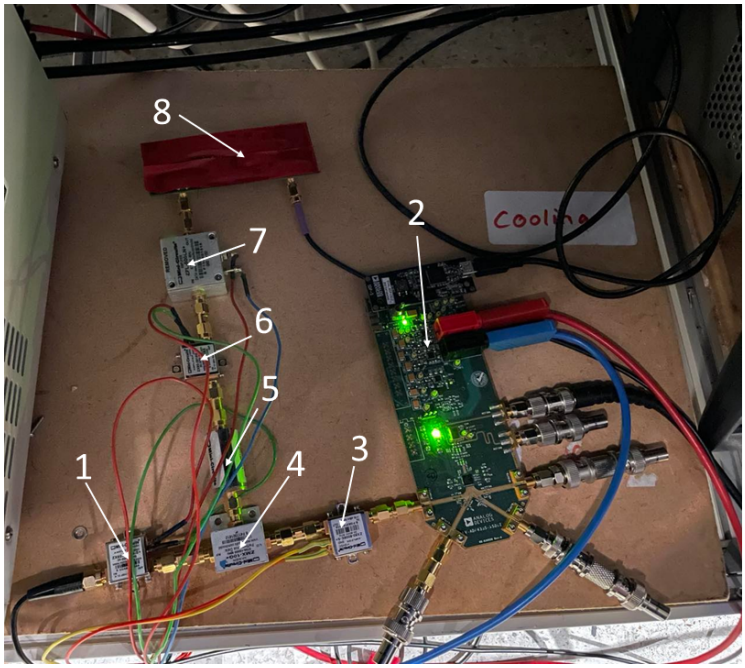


Figure 2.9: **Picture of the electronic circuit that produces the signals to lock to.** It is made from Minicircuits components (1 and 3-7) with a synthesizer (2) and a PCB (8). The components are as follows, from signal input to output. Two signals are input: the Beat signal from the photodiode input into amplifier 1, and the signal from the the synthesizer (2) input into amplifier 3. These two signals combine at the mixer (4) then pass through the low pass filter (5) then through two amplifiers (6 and 7) and into the error signal PCB (8) which the error signal passed out of and into the lock box.

the production of a decent sized MOT. For this task we use three tapered amplifiers, two in house customised Newport tapered amplifiers and self built Tapered amplifiers using eagleyard tapered amplifier chips. For the laser locked to the cooling transition, we use a modified Newport TA (TA-7613) with the amplifier chip (EYP-TPA-0780-01000) inside. This provides an output power of 600mW, which provides laser light for the imaging, push beam, 3D cooling and the input to a second customised Newport TA that has an output power of 400mW, which powers both the horizontal and vertical cooling lasers of the 2D MOT. All of these are at the same frequency and are all equally effected by tuning of the frequency by changing the synthesizer frequency. The third in house built TA that has an output power of 600mW and is used for the repumper laser and provides sufficient amplification to feed the repumper into both the 2D and 3D MOTs.

2.4 New optical setup at the science cell

This section gives a description of the optical setup close to the science cell, as this was implemented and developed recently. As previously stated the MOT system is comprised of two pairs of counter propagating beams in the vertical axis and one pair in the horizontal axis marked 1, 2 and 3 respectively in figure 2.3. This setup was implemented in this orientation to allow for optical access of the vertical imaging and imprinting systems that use high NA microscope objectives of 20× zoom for the top objective and 20× or 50× for the bottom objective. These can be seen in figure 2.10 marked as 1(top) and 2(bottom) respectively. Also implemented is a new imaging system in the horizontal axis. This system uses a dichroic mirror to combine imaging light in the same plane as the 1550 trapping beam to allow us to view the horizontal axis from that plane and to implement a system that is more magnified and cleaner than

the previous system, using larger optical components where able. This can also been seen in figure 2.10 labeled as 3) dichroic mirror and 4) new larger imaging lens. The newest part of this set up is the implementation of the flat trap, which is comprised of an optical setup that takes the zero order beam from the AOM that controls the main 1070 dipole trap beam. We are able to use this beam because when the flat trap is turned on, the 1070 beam power in the first order is already near minimum as the power has already been ramped down during evaporation, meaning that the zero order at near max power. The beam is injected into a fibre after passing through the AOM, cleaning up the mode and increasing the stability of the system. The beam then passes though the optical system, shown in figure 2.11. This system is comprised of of optics that flatten and widen the beam in the horizontal axis. Lens 1 expands the collimated output, lens 2 re-collimates the beam after expanding to, lens 3 focuses one axis of the beam, and lens 4 is responsible for the final width of the flat trap beam, which re-collimates the output beam. The final mirror pair is for directing the position of the flat trap and the final lens is a 10cm lens that focuses to the position of the dipole trap.

The final part of the system that was implemented is the imprinting system, which includes the DMD and the focusing optics. A picture of this system is seen in figure 2.12. The imprinting system uses light output from a fibre, either from the SLD or the laser. This is expanded and collimated by lens 1 to approximately 3cm wide, so the entire beam covers the DMD active area. The DMD (marked by 3) is rotated at approximately 24 degrees from the horizontal to maximise reflection, as this is the working angle of the DMD. The desired reflected part of the DMD image is passed through a telescope (marked my lenses 4 and 5) to reduce the size of the image, in most cases a 0.25$\times$ telescope was used. The image subsequently passes through a dove prism (marked by 6) which rotates the image produced. Rotating the the prism allows

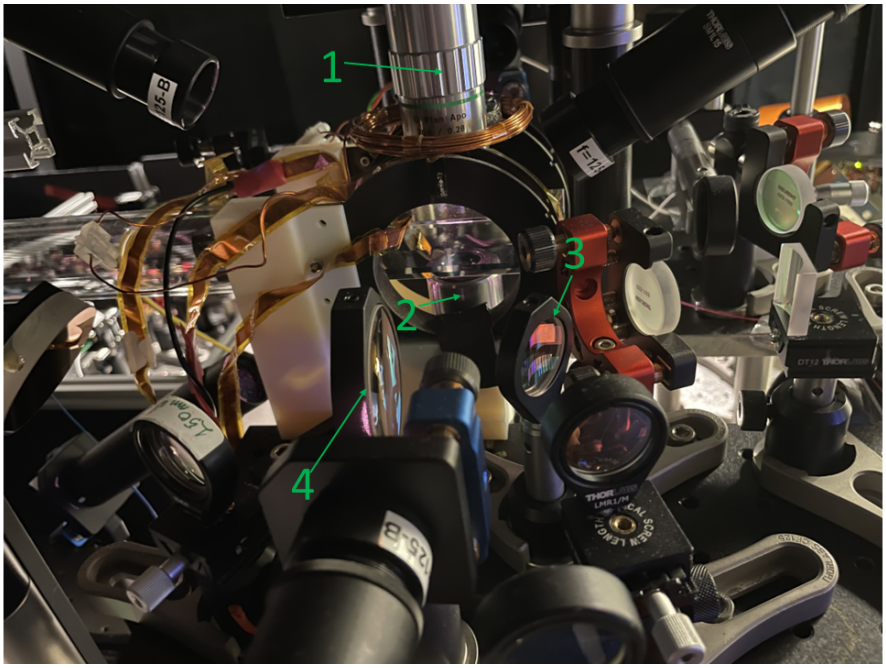


Figure 2.10: **Image of our science cell.** This includes the surrounding optics, here we are looking at: 1) The top 20× microscope objective that sends light onto the CCD. 2) The bottom microscope objective, which is either 50× or 20×, this focuses vertical imaging and imprint light onto the position of the atoms. 3) The dichroic mirror that combined the paths of the 1550nm laser and the horizontal imaging beam. 4) The new larger imaging beam lens for the horizontal imaging system.

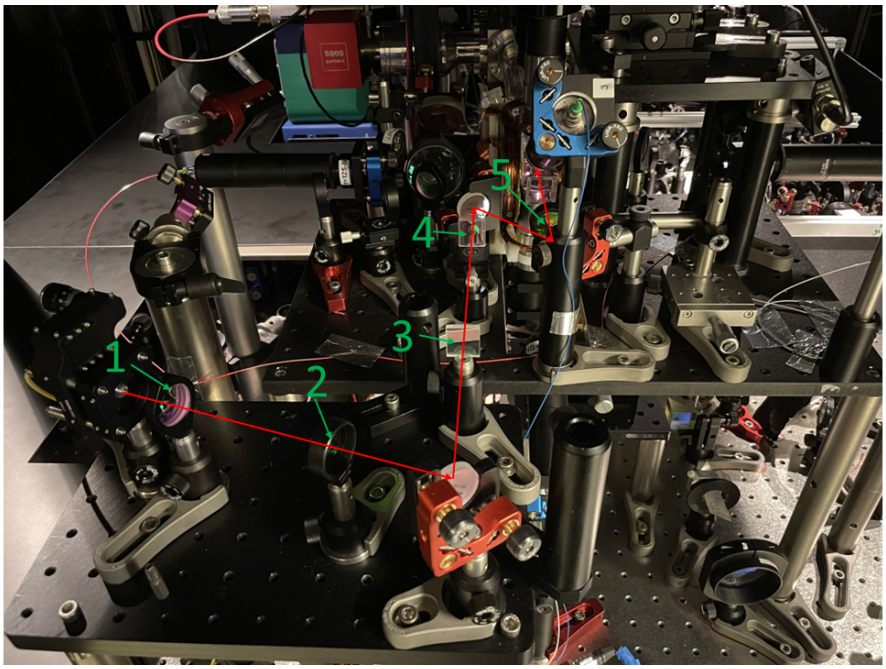


Figure 2.11: **Image of the flat trap optics.** The red arrows originate from the the fibre output and mark the beam path. 1 and 2) is a telescope that expands the beam waist by a factor of 3. 3 and 4) Telescope in the horizontal axis that reduces the horizontal beam waist by a factor of 5. 5) 10cm lens used to focus onto the atoms.

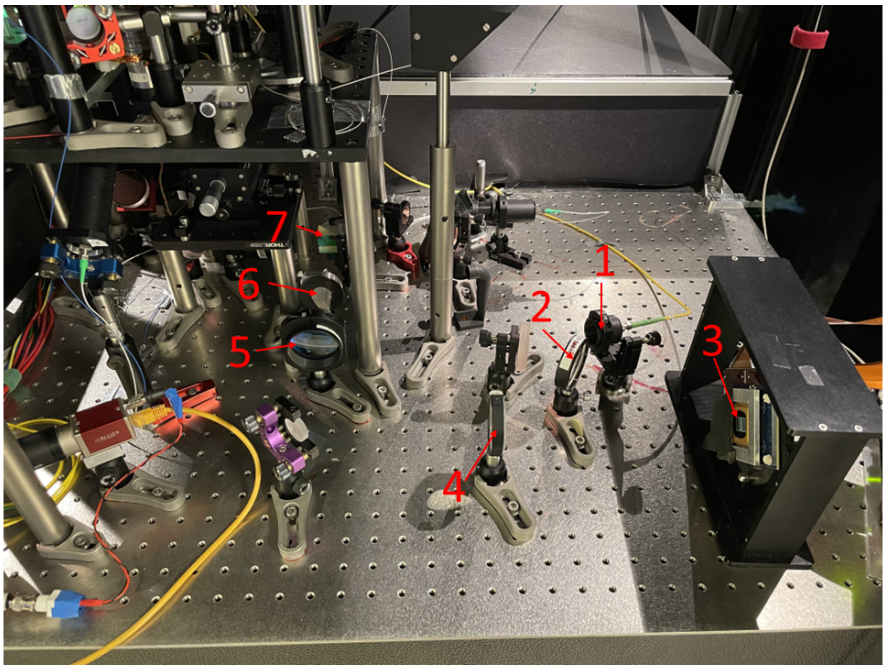


Figure 2.12: **Imprinting beam path.** Starting from fibre output (1), passing through the collimation lens (2), reflecting off the DMD (3), through the telescope (4 and 5), through the dove prism and finally combines with the imaging beam in the 90:10 beam splitter.

the image to be rotated the full 360 degrees range. The ability to rotate the image allows alignment of the DMD image to the desired axis, usually aligning the length of the image along the direction of the 1070 trapping beam. After passing through the dove prism, the imprinting beam combines with the imaging beam in a 90:10 splitter (marked at 7) that reflects 90 of the imprinting light into the system and dumps 90% of the imaging beam. The splitter allows us to create the deepest potentials possible and maximize the imprinting power that reaches the atoms since we have excess image power. The beam passes through bottom microscope objective, as seen previously in fig 2.10 labeled number 2, the objective focuses both the imprint and the imaging light onto the position of the atoms, creating an overall demagnification of 80× as standard, though we can sometimes change the system to use a 50× objective and a 0.5× telescope to reach 100× demagnification.

2.5 Optical imaging system

We use absorption imaging as our imaging technique. An in depth description can be seen here [87], however as a summary of what we use, absorption imaging is a destructive process where light resonant to the cooling transition is absorbed by the atoms increasing their energy state, destroying the BEC that is residing in a minimum energy state, having been initially repumped into the closed cycle. This absorption of light leaves behind a shadow that is picked up by the CCD (Mako G-125B) and analysed by our software to produce a colourised scale image of the cloud. In the experiment there are two such systems. One for each the horizontal and vertical axis. Both of these systems serve different purposes and are very different from one another. The imaging in the horizontal axis has a magnification of only 2.7×, which is not effective for seeing fine dynamics within the cloud due to low resolution, therefore is mainly used for quantitatively probing the parameters of the whole cloud and not internal dynamics. The cloud is usually probed only after allowing for expansion once the cloud of atoms has been dropped from the trap and allowed to expand for 25ms, reducing the density of the atom cloud in the process. From this imaging we take measurements of position, condensate fraction, atom number, temperature, shape, and optical density.

The vertical imaging system is more complex. It is comprised of a 20× mitutoyo microscope objective, seen in figure 2.10 which focuses onto the position of the cloud of atoms and sends the collected light to the CCD (Manta G-235B). This gives us a high resolution imaging system that probes the atoms in trap, with small amounts of expansion allowed due to the long working distance of this microscope objective and the translation stage it is mounted on. This is the system used to study specific dynamics within the cloud for our projects. Using this imaging system, we also

can image potential applied to the position of the atoms from the DMD, this is useful to check the potentials that are applied to the position of the atoms are well focused.

As a pair to this microscope objective we also use a partner mitutoyo objective of 50× or 20× magnification on the opposite side of the atoms, which serves two purposes, firstly to send imaging light onto the atom cloud and secondly, to send our shaped potentials onto the atoms. These potentials are magnified from the DMD size, either by a factor of 80× or 100× depending on the combination of optics chosen.

2.6 Digital micromirror device

The DMD is the most distinctive part of the experiment. It allows us to create arbitrary, dynamic and static potentials with which we use to manipulate our atom sample. The DMD is an array of 1080 × 1920 micro mirrors, each being $10.8\mu m \times 10.8\mu m$, giving a total size of $1.1cm \times 2.1$cm. The pixels can flip between two positions, 'on' which allows light to pass along the beam path aligned to the optical system, or 'off' which flips the mirrors so the light hitting those mirrors no longer follow the correct beam path and is dumped elsewhere. Images loaded onto the DMD are Bitmap(bmp) format images, where each pixel corresponds to one mirror. A black pixel means the mirror flips to the 'off' position, and a white pixel means the mirror flips to the 'on' position. Figure 2.13 shows a close up image of a DMD mirror flipped into either the off or on state, from the neutral state (neutral isn't experimentally used). Using this, images can be built to create our patterns of light that we send to the BEC. This can also be extended to grey scale images, using the method of dithering. Dithering takes an image and sets the local spatial densities of black or white pixels so we can create images that produce intensity gradients in the reflected light. When in use, the entire

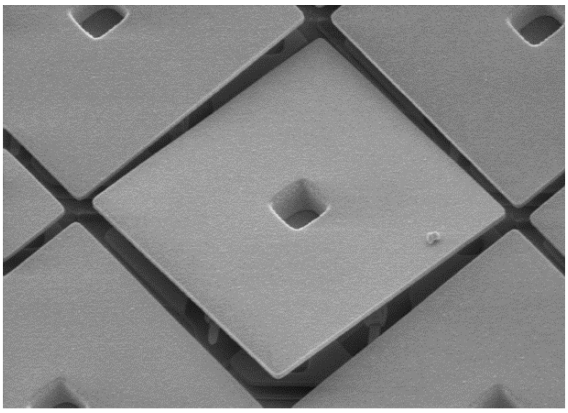


Figure 2.13: **DMD Mirror.** Close up image of a DMD mirror flipped from the neutral state.[88]

DMD is illuminated by a expanded and collimated beam of light, which is shaped by the DMD and reflected into the optical system, demagnifying the image and causing it to focus onto the atoms (this is described in section 2.1.6 above). The DMD has a max refresh rate of 10kHz which means we can chance images on the DMD once every 100μs. This limits us to being able to apply dynamic potentials on the order of $>$ 1ms accurately.

2.7 Flattened Optical Dipole Trap

Here we discuss in extra detail the trap system we use and how we have expanded upon the traditional dipole trap system that is normally used in our experiment. As a recap, we have our 1550nm laser crossed with the 1070nm laser at their focal points creating a trap with trap frequencies of approximately 115Hz, 135Hz, 33Hz and a cloud of dimen-

sions Thomas-Fermi radii $R_{tfx} = 9.9 \times 10^{-6}$m $R_{tfy} = 8.4 \times 10^{-6}$m $R_{tfz} = 35 \times 10^{-6}$m. This can be tuned by changing the ratio of potential depth provided in the final trap by each laser, simply by adjusting the power of each laser to keep the same potential depth but different shape. Clouds of this elongated cylindrical shape are typically ones we use for our experiments, as it allows for looking at dynamics along its long axis, however being roughly cylindrical in shape, it is naturally three dimensional, thus not thin in the axis that is visualised and has the DMD potential applied to. The cloud being 3D can cause a few problems when we are applying potentials and carrying out the experiment. Depending on the experimental goal, projects can either look at dynamics in 1, 2 or 3D. If we want to try to look at 2D dynamics, we would require a more 2D shape in the axis of the applied potential and imaging. Flattening the trap has benefits including: The narrowing of the cloud perpendicular to the direction the applied potential means that the atoms remain in the 'focused' part of the potential, also the atom cloud becomes a more equally distributed and less dense, meaning some dynamics are easier to visualise and analyse.

To enable this flattening of the trap we installed a new 1070nm dipole trap beam. This beam has waists of approximately $11\mu m$ and $390\mu m$ at the focal point, with a wide shape in the horizontal and narrow in the vertical. A simplified beam diagram is shown in figure 2.14, which shows how both axis of the beams are treated to create a flatter beam. This allows us to look down at the 2D plane that has been created from the vertical camera. The beam crosses with the 1550nm laser at the corresponding focal points creating a wider and 'flatter' atom cloud with trap frequencies of approximately 20Hz and 300Hz. The 1550nm laser is still used as we want to keep confinement down the length of the flat 1070 beam so the atoms don't flow away from the center of the trap down the flat beam. When implementing the flat trap in the experimental

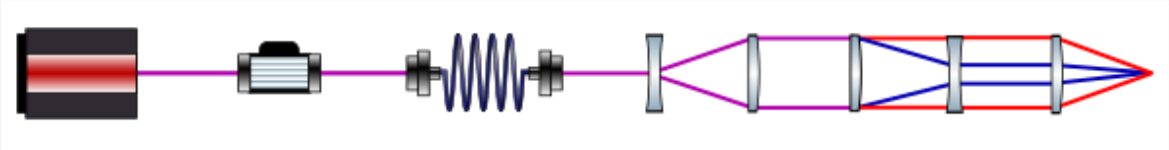


Figure 2.14: **Flat trap lenses.** The same lens system that is pictured in figure 2.11, where each axis can be seen, purple splits into red (vertical axis) and blue (horizontal axis).

sequence, the normal 1070 beam is ramped down to an off state whilst the 1070nm flat beam is ramped up, allowing a smooth transfer of atoms from one trap to another.

Whilst this flat trap system was implemented and parameterised during my time. It was not used in any published work, however it was used in some of our initial results in other projects that are not discussed in detail in this thesis. However the trap is intended to be used for furthering these projects and for future projects. One such project is the study of the superfluid fountain effect in a BEC and another is studying turbulence in a BEC with phase imprinted vortices. The goals of both of these are discussed on more detail in the conclusion, however they are both projects that would benefit from using a 2D BEC. The vortices that we wish to study are simulated in a 2D plane, thus a BEC that can be more 2D than our standards BEC is needed for achieving and comparing any results achieved. The superfluid fountain effect experiment needs a narrow channel between the atomic samples, so we need confinement in the vertical plane that our DMD cannot achieve. By comparing the trapping frequencies of the final flat trap and the normal, it can be seen that we achieve a trap that is approximately 2-3 times higher frequency in the vertical plane and 0.66 times the max frequency and is circular in the horizontal. This leads to a cloud of atoms that has Thomas-Fermi radii of $R_{tfx} = 1.5 \times 10^{-6}$m $R_{tfy} = 22 \times 10^{-6}$m $R_{tfz} = 22 \times 10^{-6}$m and total atom number of $N_{Flat} = 50 \times 10^{-3}$. Figure 2.15 shows the condensate from our imaging beams. In

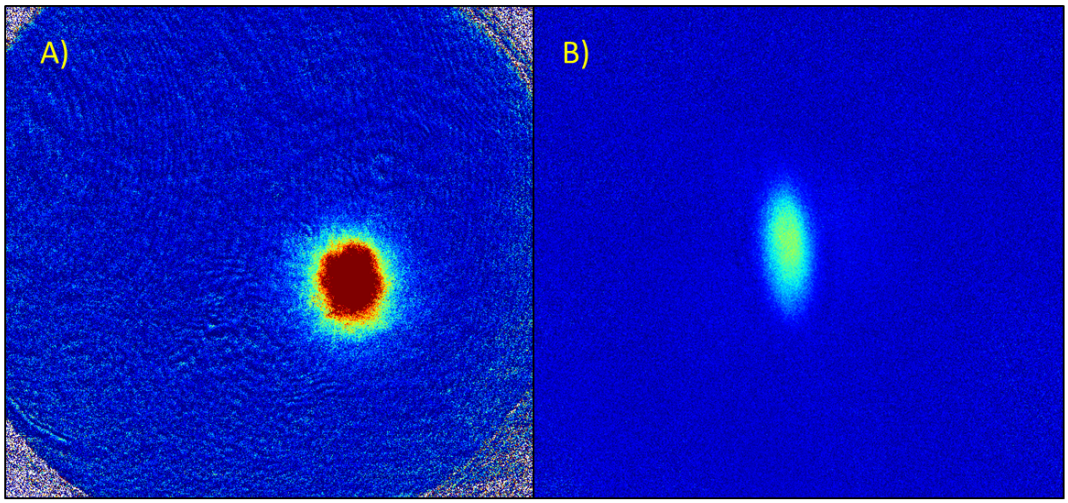


Figure 2.15: **Images of the Condensate produced by the flat trap.** A) Image of the condensate produced taken from the vertical axis in trap. B) Image of the condensate in 25ms time of flight from the horizontal axis.

fig 2.15A) the condensate is seen from above, as a flat 'disk' shape. Figure 2.15B) is where we note the flatness, it can be seen that the aspect ratio has inverted in time of flight, this is a signature of an asymmetric trap occurs due to increased repulsive forces in compressed axis of a BEC in trap expand faster once released, this effect can be seen in more detail in [89]

2.8 Control system

The system we use to control experimental parameters, such as laser power and timings, outputs both digital and analogue signals. These signals are timed in an experimental sequence that is run to create a BEC in our science chamber. We use a program called Cicero as the control software for this task. It interacts with the control system which outputs fixed 3.5V digital signals and analogue signals that vary between $-10V > 10V$.

These signals are used to control shutters that can close or open to allow laser light through, controlling AOMs to finely control the power of a laser going to the desired location and to trigger items, such as the DMD and the camera, at times given in the sequence.

2.9 Sequence

The sequence to control the experiment has many components. Here the most simple sequence for creating a BEC will be discussed. The key components of the sequence are shown in figure 2.16. The sequence can be summarised in the following stages. The mot loading stage, where the atoms are loaded into the Magneto optical trap from the 2D MOT in the first 5 seconds of the sequence, making a MOT at the location of the dipole trap crossing point. The next stage is the Dark MOT, where the repumper power is reduced to allow the atoms to drop into the ground state. This again is at the location of the dipole trap which is turned on after the atoms are in the ground state, so hold the atoms with dipole forces in these laser beams. The final stage of cooling is done with evaporative cooling, where the dipole trap lasers have their power ramped down, following an exponential reduction of reduction of laser power causing a reduction of intensity and therefore reduction in potential depth, creating a BEC that is held within a trap. In addition can be manipulated by our optical potentials and is also imaged by triggering the camera three times to acquire three separate images that are combined to make one. The manipulation is provided by triggering on our imprinting light source, in combination with triggering the DMD at the end of evaporation after the cloud has thermalised and then probed/imaged with our imaging system, in trap or with expansion time added for increased clarity of features or internal structure of the BEC.

In the situations where we use the DMD with a dynamic pattern we need use a function generator to provide triggering to the DMD at a chosen frequency so the DMD cycles through the 'images' at the correct rate that produces the sequence that manipulates the atoms in the desired fashion, the same as making a video.

2.10 Sources of light for atomic manipulation

Due to the unique properties of the light produced by super luminescent diodes (SLD) it has become an active, intriguing and novel part of our experiment, used as an alternative light source to create optical potentials. To understand its properties more, analysis was carried out that focused on the quality the potentials created by this light source and that of the Laser, which is more commonly used. Before looking at the analysis between these sources it is important to understand how the light sources discussed work, thus the following section will describe the physical properties of these sources and compare them, highlighting how the SLD bridges the gap between the LED and the laser.

2.10.1 Laser

Lasers are the most commonly used light source in the field of atomic physics as the can address specific atomic transitions. They operate by stimulated emission in an optical cavity. Inside of the optical cavity is a gain medium that is put into an excited state by an external source of energy. A pump beam is injected into the cavity where the gain medium is. This pump beam interacts with atoms by either causing atoms in a lower energy/ground state to excite, or by causing atoms in a higher energy state to emit a photon and de-excite. In the example case of a solid state laser, when the

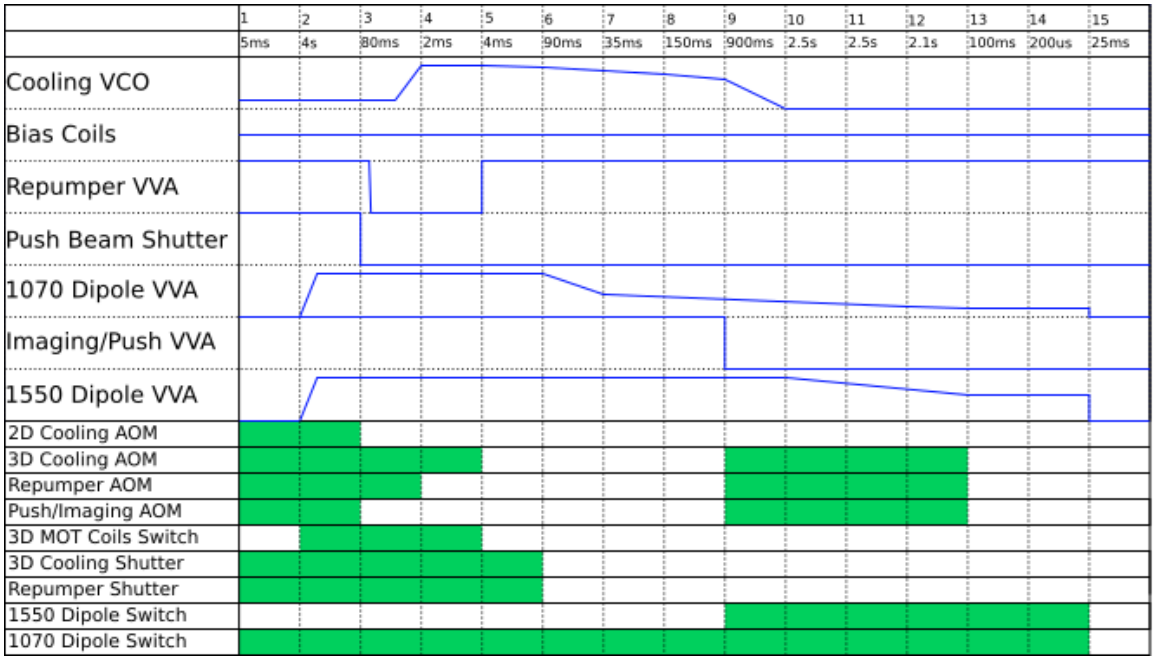


Figure 2.16: **Experimental sequence to create a BEC.** The timing of each analogue and digital channel in the sequence to create a Bose Einstein condensate, where the blue lines show the voltages between 0V-10V, and the green segments indicate on/open, each segment is a separate step in the sequence. Each VVA used effectively controls the power passing into the system from the respective AOM, where higher voltage leads to increased power transmission. The cooling VCO adjusts the frequency of the cooling light between the MOT loading, dark ramp and imaging steps. The Bias coils require a fixed voltage and the push beam shutter just needs switching off after the MOT loading stage. The digital channels shown underneath the analogue channels show more specific on/off timings. It can be seen that segments such as the 1550 laser which has both analogue and digital channels, that the AOM is only switched on in stage 9, even though the VVA is on at max power much earlier, this is due to a lag in response time from the VVA. Some AOMs are also kept on in stages 9-12 to keep the temperature stable throughout the course of multiple sequence runs.

gain medium has a population inversion (more atoms in the excited state than in the ground state) caused by optical pumping of the gain medium by a pump beam that is injected into the cavity, the result is a rate of stimulated emission which is greater than the rate of absorption of photons, which causes amplification of the pump beam in the cavity, producing photons of the same properties as the input beam (which matches the absorption lines of the gain medium). In lasers the cavity length is tuned to fit in an exact number of wavelengths into the cavity, selecting and amplifying the output wavelength within the cavity, filtering out undesired wavelengths of light. As a result, this creates light that is both temporally coherent and spatially coherent with a narrow bandwidth.

2.10.2 Super-luminescent Diode

SLDs are similar in construction to laser diodes, in that they contain a forward biased P-N junction and an optical waveguide. The light produced by a SLD is also similar to that produced by a standard laser diode, except that in the SLD it intentionally has a strong suppression of feedback through a combination of a tilted waveguide and anti-reflection coatings applied to the facets. This suppression of feedback means that the formation of resonator modes or spectral narrowing in the optical spectrum of the SLD does not happen, like it does in the laser. The lack of feedback means that lasing is not achieved and instead the diode performs amplified spontaneous emission, with a spectrum that is not narrowed by the effects of a cavity. SLDs therefore produce light that is temporally incoherent but features high spatial coherence. The broadband nature and peak wavelength of SLDs is designed and chosen from the construction pf the semiconductor material in the P-N junction. it is chosen to have holes and electrons have a large number of possible energy states/bands. Therefore when we get electron hole recombination within the device a broad range of optical frequencies is produced.

2.10.3 LED

LEDs are perhaps the simplest of the three systems. They are a P-N junction that when forward biased the electrons move from the N doped region to the P doped region where they combine with the holes. The recombination process causes emission of a photon in a random direction. The light created is incoherent spontaneous emission that is emitted over a large solid angle and has a wide range of optical frequencies. Unlike the SLD and the laser, there is no gain medium in an LED.

2.10.4 Comparison

In the previous section the construction of each device was covered. Within those devices the important properties of the light produced are the phase/temporal coherence, spatial coherence, bandwidth and intensity. These are properties that atomic physics and imaging techniques rely heavily upon. Figure 2.17 displays a simple depiction of each source, the laser with its gain cavity gain medium, producing a narrow high intensity spectrum. The SLD with its single pass amplification producing a less intense but broader spectrum. Finally the LED where we have no amplification producing a broad and relatively low intensity spectrum. Atomic physics often requires addressing specific atomic transitions that absorb specific wavelengths of light, meaning that due to the narrow bandwidth of the light produced, the laser is the chosen source for manipulating internal states of an atom. On the other hand due to the broader bandwidth of the light produced by the SLD and especially the LED, addressing specific atomic transitions in most common systems like ours would be impossible as multiple transitions would be excited, destroying the system. However the spectral properties of all three of these sources have minimal effect in the creation of far detuned optical potentials. Therefore all three of these sources, in the far detuned case can in theory

achieve an optical potential to trap atoms. The laser benefits over the SLD and LED in that you can more precisely choose the desired wavelength, giving more freedom to choose the value of the detuning from any desired optical transition, giving the ability to create a deeper potential with minimal heating effects that are caused by any overlap in the spectrum of the laser light with the atomic transition. Following from this, the SLD is the mid ground between the laser and LED, its produces a less broadband spectrum of light than the LED, thus its peak wavelength can get closer than the LED to a desired transition without causing heating effects. Considering the spatial coherence of the three sources, the laser and SLD light is formed in cavities or waveguides respectively and as a result, the light is produced with a high spatial coherence. Conversely, the LED light forms from a surface and is emitted in a large solid angle, meaning that spatially incoherent light is produced. This becomes important when the sources are integrated into an optical setup, as spatially coherent light is controllable with conventional optical systems. Whereas spatially incoherent light is very difficult to manipulate with conventional optics and losses in power are to be expected.

Another property of the three sources to consider is the temporal coherence. This feature is related to bandwidth of the light produced, it is essentially a measure of how monochromatic a light source is, thus how much the light will interfere with its self. Looking at the three light sources again, the laser which produces light with a very low bandwidth has a very high temporal coherence, in optical systems that can lead to monochromatic aberrations in images produced with this light. However the SLD has a larger bandwidth, thus a lower temporal coherence, and the LED an even lower temporal coherence. This means that images produced with these light sources should have fewer monochromatic aberrations than their laser counterpart due to fewer

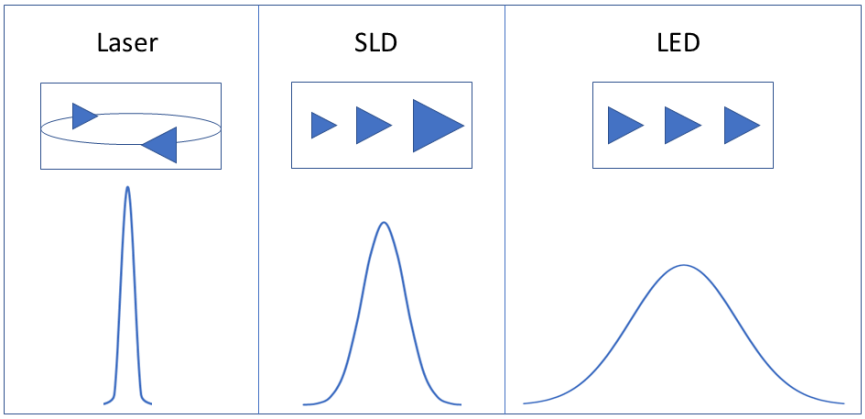


Figure 2.17: **Graphic depicting the differences between the laser, SLD and LED.** Here we see that the laser produces a narrow spectrum of light, from a cavity with amplification, the LED produces a broadband spectrum of light with no gain medium or amplification, and the SLD produces a spectrum between the two and it amplified one way by a gain medium.

interference effects.

Chapter 3

SLD Generated Optical Potentials Applied in Cold Atoms

The material in this chapter includes text, images and data that have been published in the paper: A. Smith, T. Easton, V. Guarrera, and G. Barontini. "Generation of optical potentials for ultracold atoms using a superluminescent diode". Which was published in Physical Review Research. Some of this material remains largely unchanged, others has been made more appropriate for the thesis.

This chapter reports on the realization and characterisation of optical potentials for ultracold atoms using a superluminescent diode. The light emitted by this class of diodes is characterised by high spatial coherence but low temporal coherence. On the one hand, this implies that it follows Gaussian propagation similar to lasers, allowing for high intensities and well collimated beams. On the other, it significantly reduces those interference effects that lead to severe distortions in imaging. By using a high-resolution optical setup, we produce patterned optical potentials with a digital micromirror device and demonstrate that the quality of the patterns produced by our superluminescent

diode is consistently and substantially higher than those produced by our laser. We show that the resulting optical potentials can be used to arrange the atoms in arbitrary structures and manipulate them dynamically. Our results can open new opportunities in the fields of quantum simulations and atomtronics.

3.1 The System

Details about our experimental sequence and methods can be found above, but also in [48, 90]. For this experiment the experimental parameters and sequence in brief are, loading ^{87}Rb atoms from a 3D MOT into a crossed dipole trap and then perform evaporative cooling for 6 seconds to produce a Bose-Einstein condensate (BEC). For this work the final trapping frequencies are $f_r = 150$Hz and $f_x = 10$ Hz, resulting in an elongated BEC with $N = 2 \times 10^4$ atoms at $\simeq$20nK.

To manipulate the atomic sample, we use the optical setup shown in figure 3.1a. Our SLD light source is a Thorlabs SLD830s-A20, emitting 23mW over a spectrum that has a full-width at half maximum of $\Delta\lambda$ =20.3nm, which is centred at λ_c =836nm, as shown in fig 3.1b. From the spectrum it is estimated that the coherence length of the SLD is $l = 2\ln 2\lambda_c^2/n\pi\Delta\lambda \simeq 15$ μm. The light produced by the SLD is amplified to 300mW using a tapered amplifier that has a gain centered at 840nm (Eagleyard EYP-TPA-0830). The spectrum of the amplified light is a convolution between the gain curve of the TA and the SLD spectrum. This is also shown in fig 3.1b, where it can be appreciated that after the amplification, the spectrum is centered at λ_c' =840nm and its full-width at half maximum is $\Delta\lambda'$ =9.4nm. Therefore the effect of the amplifier as well as increasing power output, also shifts the peak and centre of the spectrum and the full-width at half maximum is smaller than that of the bare SLD. This results in a

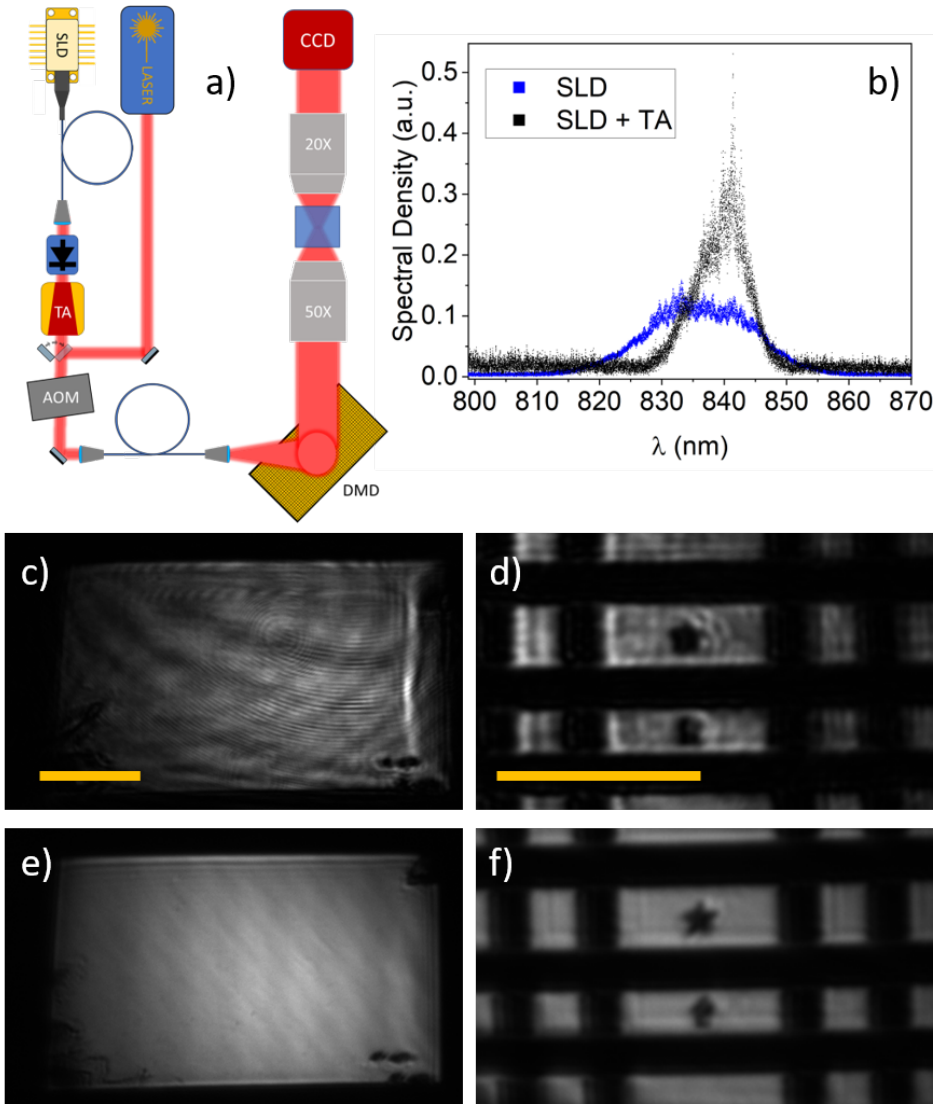


Figure 3.1: **Schematic representation of our optical system, TA gain spectrum and laser/SLD light comparison.** a) Schematic representation of our optical system. The SLD light is first amplified by a TA and then injected into an optical fibre to clean the mode. An AOM is used to control the power injected in the fibre. The output of the fibre is reflected by a DMD that imprints arbitrary patterns on the intensity profile. The patterned intensity profile is then imaged on the atoms using a 100× demagnification system that includes a 50× objective. The plane where the image is produced, that corresponds to the plane where the atoms are trapped, is then imaged on a CCD camera using a 20× magnification system. We can use the same path for the laser source by activating a flip mirror. b) Emission spectrum of the SLD (blue) and spectrum after the SLD emission has been amplified by a TA (black). The spectra are normalised to have the same area. c) Image produced by the laser at the position of the atoms with the DMD fully *on*. d) Same as c) but with a 2× zoom on a pattern containing an irregular mesh, a star and an arrow. Both the bars in c) and d) correspond to 50 μm. e) and f), same as c) and d) but using the SLD as light source.

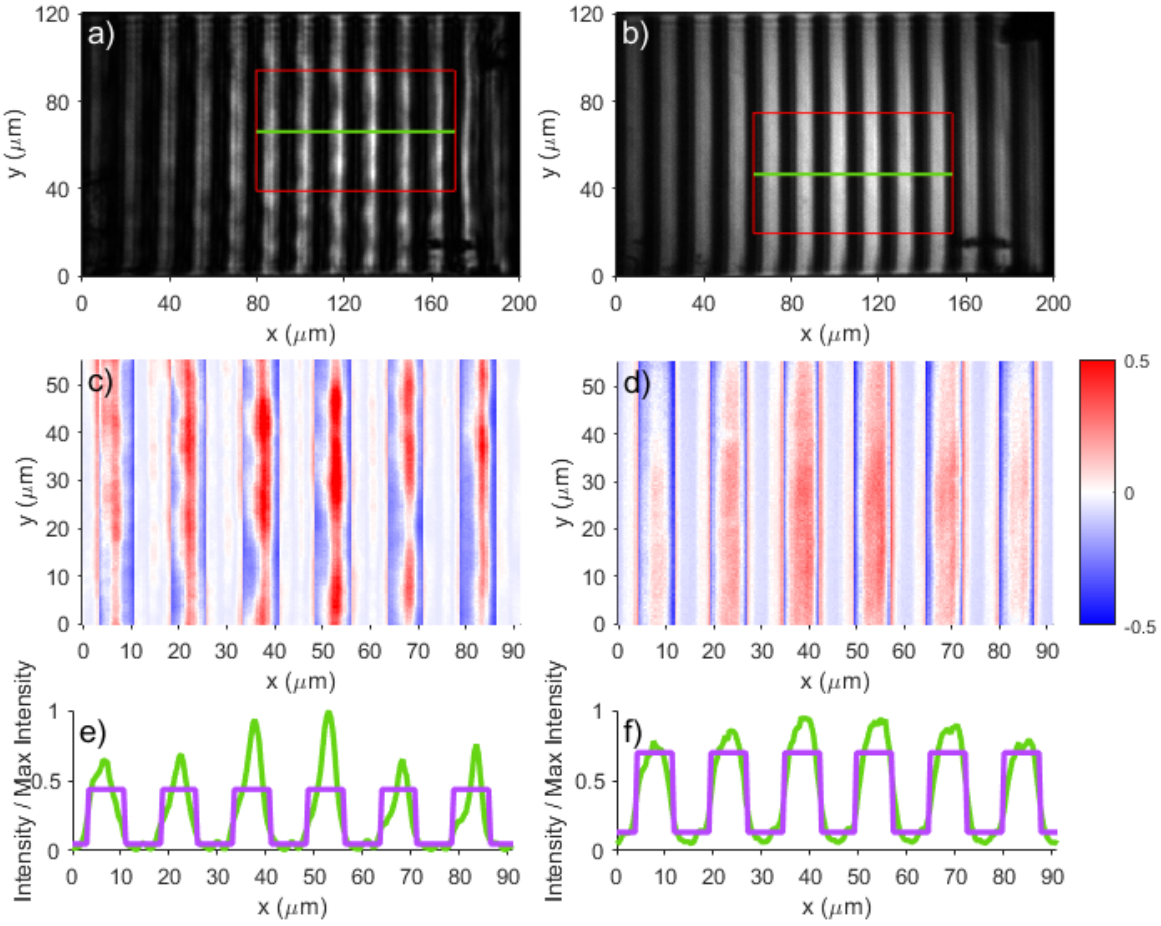


Figure 3.2: **SLD and Laser Residuals.** a) Image produced on the plane of the atoms using the laser source and a square-wave pattern on the DMD with period 1512 μm, corresponding to a period of 15.12 μm in the imaging plane. b) The same as a) but using the amplified SLD as the source. c) And d) are the residuals obtained by fitting with a square-wave grating the regions within the red rectangles in a) and b) respectively, which correspond to the beams peak intensity regions. The colour bar indicates the values of the residuals. The green curves in e) and f) correspond to 1D cuts along the green lines in a) and b) respectively. The magenta curves are the fits to the data using eq. (3.1).

doubly longer coherence length of $l' \simeq 33\mu$m. Care must be taken to provide 30 dB of optical isolation between the TA and the SLD to prevent damage to the latter caused by the TA spontaneous back emission. The amplified light passes through an acousto-optic modulator which allows us to control the power of the light that is then injected into a single mode optical fibre. A flip mirror allows us to use the same acousto-optic modulator and fibre system with a laser tuned at 800nm, simply by flipping the mirror and aligning the fibre. This simple system enables a direct and easy comparison between the two light sources. We do not observe any difference in the acousto-optic modulator efficiency between the two light sources. The light coming out from the optical fibre is reflected by a DMD and eventually directed onto the atoms, hitting the atoms in the vertical axis. The light passes through an optical system that demagnifies by a factor 100 and includes a 50× high-resolution optical microscope objective as the final lens focusing onto the atoms. The DMD has 1920×1080 micromirrors of size 10.8μm. Each micromirror can be individually set *on* or *off* every 100μs. After reflection by the DMD and transmission through the optics, we typically obtain $1mW$ of power at the position of the atoms. We note that the reflection from our DMD is only $\simeq$10%, although we expected $\simeq$50 % reflectivity according to the specifications of the device.

The images produced by our system are focused on the position of the atoms and imaged on a CCD mounted in the vertical direction, using a 20× magnifying objective, resulting in a resolution of $\simeq 2\mu$m. The same imaging system is used to perform high-resolution absorption imaging of the atoms. In Fig 1c-f four examples images are shown, c & d being laser, and e & f being SLD. it can be qualitatively seen that the SLD-generated images present sensibly reduced interference fringes, are overall more uniform and feature finer details than those of its laser counterpart.

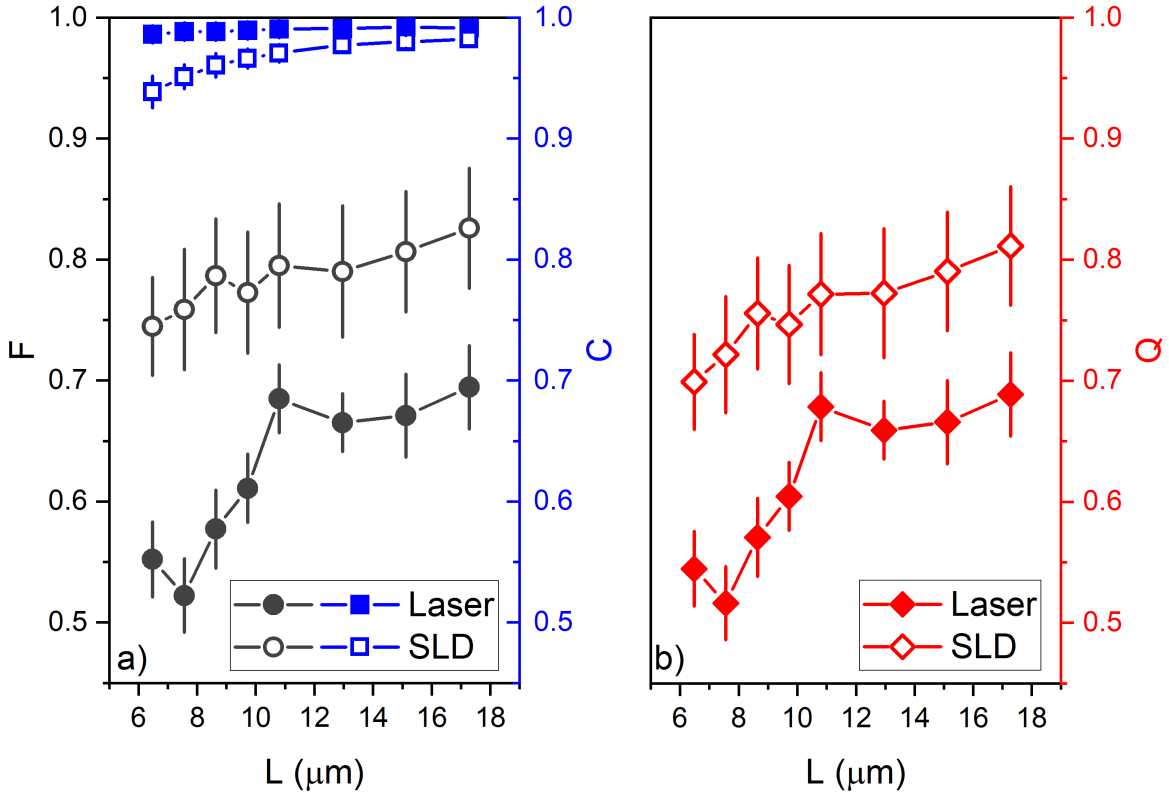


Figure 3.3: **Fidelity and Contrast of square wave.** a) Fidelity (circles) and contrast (squares) of the SLD images (open symbols) and laser images (filled symbols) as a function of the semi-periodicity of the square wave L. b) Quality of the image as a function of L for the SLD images (open symbols) and the laser images (filled symbols).

3.2 Image Characterisation

In this section we quantitatively compare the images produced using the SLD and the laser. For simplicity and clarity, we constrain the analysis to only one-dimensional structures, as our findings can be easily extended to two dimensions, for example by using grid of squares and analysing in both the x and y axis. In particular, we investigate the ability of the two sources to produce square-wave gratings with our optical system, as in the examples in figure 3.2a & b. In order to quantitatively compare the images produced by the two sources, we use two parameters: the *fidelity* and the *contrast*. We have chosen to separately evaluate these two parameters to highlight the superior quality of the square-wave patterns produced by SLDs, regardless of their amplitude or residual background. To compute the fidelity, we perform two-dimensional fits of the images, I, captured by the CCD with the "target image",

$$I_0(i,j) = A + B\theta[\cos(\pi id/L + \phi)] \tag{3.1}$$

i.e., a perfect square-wave grating, with $\{i, j\}$ the pixel coordinates in the horizontal and the vertical of the image, d the pixel size, θ is the heavyside step function and L the semi-period of the square-wave. A, B and ϕ are free fitting parameters. The fidelity is then defined as:

$$F = 1 - \frac{1}{BN}\sqrt{\sum_{i,j}(I(i,j) - I_0(i,j))^2} \tag{3.2}$$

where N is the number of CCD pixels in the region of interest. As an example, figures 3.2 c & d are the residuals $I(i,j) - I_0(i,j)$ obtained by fitting the outlined regions in figure 3.2a & b with the same square-wave function. We consistently observe that for SLD-generated images the values of the residuals are lower all across the images, and

also that the images have fewer aberrations. This is also evident in Fig. 3.2e and f, where we show the 1D cuts across the green lines in Fig. 3.2a and b together with the fits done using eq. (3.1). To evaluate the contrast, the images have been integrated along the y direction obtaining one-dimensional arrays $\tilde{I}$ which are then computed by

$$C = \frac{\max(\tilde{I}) - \min(\tilde{I})}{\max(\tilde{I})}. \tag{3.3}$$

3.2.1 Fidelity and Contrast Analysis

The fidelity quantitatively estimates how close the image produced is to the target image, while the contrast accounts for the ability of a certain source to effectively produce dark regions, indeed it varies linearly with $\min(\tilde{I})$. For the implementation of accurate optical potentials for cold atoms we require both these quantities to be as close to 1 as possible. Indeed, low values of F indicate aberrations in the optical potential and therefore a limited capacity to accurately manipulate the atoms. Low values of C imply instead that higher intensities need to be used to reach the desired potential depth, causing an increase in the scattering rate that makes the potential increasingly less conservative. To account for both these effects we use the *quality of the image* $Q = F \times C$ as our figure of merit. An image with $Q = 1$ would perfectly produce the desired optical potential.

In figure 3.3 we show the results of analysis for the behaviour of F, C and Q as a function of L. With L we indicate the semi-periodicity in the imaging plane, therefore L is a factor 100 smaller than the semi-periodicity of the pattern on the DMD. The SLD

images are characterised by a slightly lower contrast than the laser images, especially for low values of L. Our measurements therefore confirm that temporal coherence plays a minor role in the contrast of an image [91], but also suggest that as the size of the features is reduced, such role becomes increasingly important. Notably, SLD images consistently feature a significantly higher fidelity, as the reduced temporal coherence of the SLD almost completely eliminates interference effects. The main source of loss of fidelity for the SLD images is the underlying Gaussian distribution of the intensity, as can be seen for example in figures 1e and 2b&d. The overall effect is that the SLD generates images with values of Q higher by at least 0.1 than those generated by the laser over the whole range explored. Our imaging system does not allow us to perform quantitative measurements for $L < 5$ μm. To provide a qualitative estimate below the limits of our imaging system, we fit C and F with second order polynomial functions. By doing this we infer that the SLD images should feature a higher Q down to sub-μm structures.

Another important feature stemming from the partial incoherence of SLD-generated light is that it is free from the Talbot effect, that alters the periodicity of regular structures as the beam propagates. This can be observed in Fig. 3.4, where we report the quality of the image Q as a function of the distance from the focal plane D for $L = 7.56\mu$m. We observe that for SLD-generated images Q is a smooth function of D, while for laser-generated images Q presents some local maxima and minima. The minima are due to the Talbot effect, that at integer fractions of the Talbot length $\Lambda = 2(2L)^2/\lambda$ causes the appearance of images with $L/2$ semi-periodicity. This in turn causes a degradation both in F and C. SLD-generated images feature also higher values of Q over a broad range of D. The fact that the images produced by the SLD are free from the Talbot effect can be relevant for the implementation of high-quality

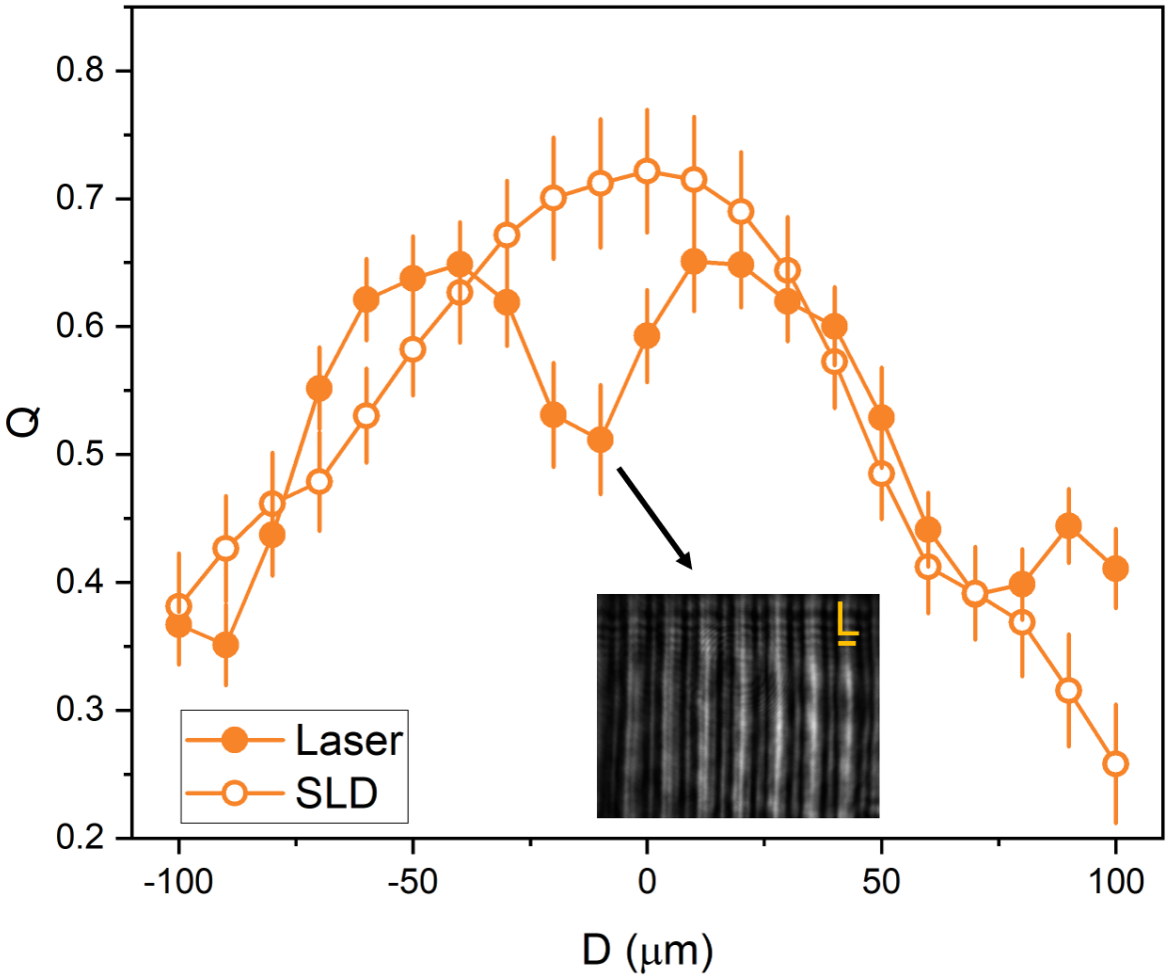


Figure 3.4: **Talbot effect.** Quality of the image generated by the SLD (open symbols) and the laser (filled symbols) for L=7.56μm a function of the distance from the focal plane D. For SLD-generated images Q is a smooth function of D, while for laser-generated images Q is modulated by the Talbot effect, that every $\simeq$80μm generates images with semi-periodicity $L/2$, as shown in the inset.

3d-patterns, lattices and holograms using two perpendicular beams that carry periodic or near-periodic structures.

3.3 SLD-generated Optical Potentials for Cold Atoms

Besides the low temporal coherence that enables the generation of optical potentials with higher quality than lasers, SLDs feature high spatial coherence, that in turn implies Gaussian propagation. On the one hand this represents a problem in reaching very high values of Q, as demonstrated in the previous section. On the other, this is a crucial feature to reach sufficiently high intensities and generate optical potentials that can be used to manipulate ultracold atoms.

Using the SLD, with our setup we can achieve 1mW of power over an area of $207\times117\mu$m at the position where the atoms are trapped. To evaluate the corresponding optical potential, we fit the amplified spectrum of Fig. 1b with a double-Gaussian obtaining the power spectrum $G(\lambda)$, with λ the wavelength, and then we calculate

$$U(x,y) = -\frac{\pi c^2}{2}\Gamma \int \left(\frac{2}{\Delta_2\omega_2^3} + \frac{1}{\Delta_1\omega_1^3}\right) J(x,y,\lambda)d\lambda \tag{3.4}$$

with Γ the linewidth and $\omega_{1,2}$ the frequencies of the D1 and D2 lines of ^{87}Rb, $\Delta_{1,2} = \omega_{1,2} - 2\pi c/\lambda$ the corresponding detunings, and

$$J(x,y,\lambda) = \frac{2P}{\pi w^2}\frac{G(\lambda)}{\int G(\lambda)d\lambda} e^{-2\frac{x^2+y^2}{w^2}}, \tag{3.5}$$

where P is the total power at the position of the atoms and w is the waist of the beam obtained with a Gaussian fit of the intensity profile of Fig. 1e. Similarly, we calculate

the heating rate as

$$\Gamma_h(x,y) = \frac{\pi c^2 \Gamma^2}{2\hbar} \int \frac{E_r}{k_B} \left(\frac{2}{\Delta_2^2 \omega_2^3} + \frac{1}{\Delta_1^2 \omega_1^3} \right) J(x,y,\lambda) d\lambda, \tag{3.6}$$

with $E_r = 2\pi^2\hbar^2/m\lambda^2$ the recoil energy, where m is the mass of the atoms, and k_B the Boltzmann constant. With our setup we can obtain a maximum intensity of $2P/(\pi w^2)$ =14.3W/cm^2, corresponding to a maximum potential depth $U/k_B \simeq 90$nK. This red-detuned potential is therefore sufficiently strong to efficiently manipulate our ultracold sample. The associated maximum heating rate is instead $\simeq$1nK/s. For comparison, the heating rate for a laser at 840nm with the same intensity is $\simeq$ 0.5nK/s. Indeed, we could not observe any measurable heating in the typical time scale of our experiments (hundreds of ms) even when illuminating the atomic cloud with the DMD fully on.

3.3.1 Static Potentials

We demonstrate that the combination of the good quality of the images produced by the SLD and the arbitrary patterns produced with a DMD can be used to arrange ultracold atoms in non-periodic structures. We have implemented two arbitrary 'disordered' 1D potentials seen in figure 3.5 by setting unequally spaced gratings on the DMD, as displayed in the back panels. The white vertical lines, corresponding to regions of high intensity, cross with the dipole trap potential creating a series of neatly-separated, sharp squared dimples of different sizes and with different spacing. The dimples are sufficiently deep to trap the atoms, indeed their density profile in absorption nicely retraces the patterns imprinted on the DMD, including the sharp edges. Evaluating the fidelity and contrast directly on the the atomic sample can therefore also be used to characterise the potential.

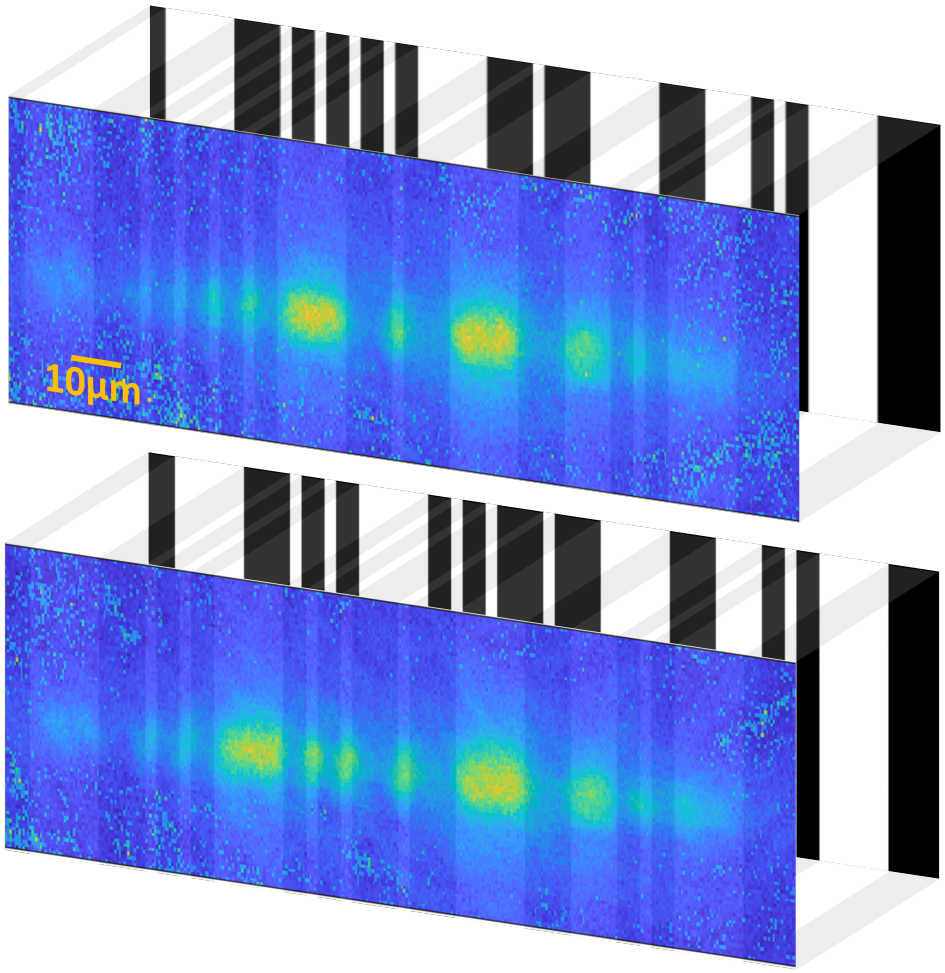


Figure 3.5: **Disordered SLD Potentials.** In-situ absorption imaging of our ultracold atoms under the action of two distinct 'disordered' potentials. The temperature of the atoms is 20nK. The patterns imprinted on the DMD are reported in the back panels, and we indicate with black (white) the regions of the DMD where the micromirrors are set to off (on). Regions where the micromirrors are on correspond to regions with full intensity on the atoms, and therefore to attractive potentials. The depth of the potential is 90nK. The atoms re-arrange in such 'disordered' potentials, nicely retracing the patterns set on the DMD.

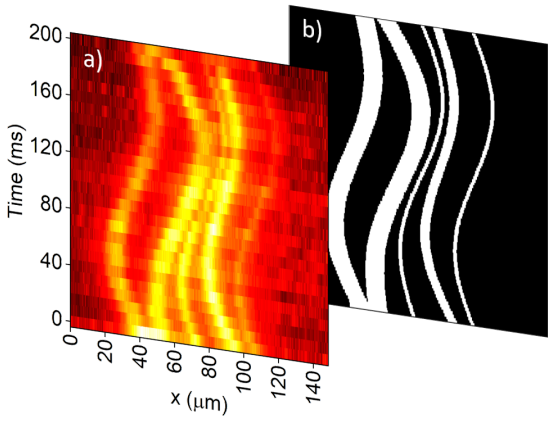


Figure 3.6: **Dynamic potential with the SLD.** a) Evolution of the atomic column density, integrated along the y direction, as a function of time under the action of the dynamical potential (also integrated along the y direction) displayed in panel b). The time frames are taken every 8 ms. The black (white) regions in b) correspond to micromirrors set off (on) on the DMD.

3.3.2 Dynamic Potentials

We finally demonstrate the implementation of dynamical potentials with SLDs. The possibility to rapidly reconfigure the pattern on the DMD is particularly appealing as it allows us to dynamically and arbitrarily modify the potential on the atoms a fast as one frame every 100μs. For dynamical potentials, good image quality is especially desirable as it ensures a good uniformity of the potential across the whole illuminated area, potentially reducing losses of atoms, spurious excitations and heating. In Fig. 3.6a we report the evolution of the density profile of our ultracold atomic sample under the action of the dynamically varying 'disordered' potential of Fig. 3.6b. For every frame we have integrated the density profiles along the y direction. In this case, the pattern on the DMD was modified every 500μs. We observe that the atomic density is dynamically modified following the trajectory of the optical potential. After 200ms of evolution, we retain $\simeq$75% of the atoms.

Chapter 4

Bloch Oscillations in Synthetic Dimensions Within Ultracold Atoms

The material in this chapter includes text, images and data that have been submitted for publication in the paper: C. Oliver, A. Smith, T. Easton, G. Salerno, V. Guarrera, N. Goldman, G. Barontini and H. M. Price "Bloch Oscillations Along a Synthetic Dimension of Atomic Trap States". This has been submitted for publication in physical review X. Some of this material remains largely unchanged, others has been made more appropriate for the thesis. The experimental work and data analysis was carried out by T. Easton and I, and the numerical data was produced by C. Oliver, with a lot of the theoretical work carried out by C. Oliver, a lot has been excluded from this thesis, but some material included for relevance.

This chapter will cover the theory, experimental and theoretical results of the experiment carried out, and the methods and analysis used to reach such results. As a recap, the goal of this experiment was to experimentally engineer a very long synthetic dimension of many tens of atomic trap states by dynamically modulating the harmonic

trap of an ultracold atomic sample. This is experimentally confirmed by showing that by controlling the driving frequency a force can be generated along the synthetic dimension that induces Bloch oscillations.

In addition to the brief motivation in the introduction we see that synthetic dimensions can provide a powerful approach for simulating condensed matter physics in cold atoms as seen in [62, 93, 56, 57, 67, 68, 64, 65, 66, 58, 61, 70, 92, 69] and photonics [72, 94, 95, 96], whereby a set of discrete degrees of freedom are coupled together and re-interpreted as lattice sites along an artificial spatial dimension. However, atomic experimental realisations have been limited so far by the number of artificial lattice sites that can be feasibly coupled along the synthetic dimension. Here, we experimentally realise for the first time a very long and controllable synthetic dimension of atomic harmonic trap states [13, 71]. To create this, we couple trap states by dynamically modulating the trapping potential of the atomic cloud with patterned light. By controlling the detuning between the frequency of the driving potential and the trapping frequency, we implement a controllable force in the synthetic dimension. This induces Bloch oscillations in which atoms move periodically up and down tens of atomic trap states. We experimentally observe the key characteristics of this behaviour in the real space dynamics of the cloud, and verify our observations with numerical simulations and semiclassical theory. This experiment provides an intuitive approach for the manipulation and control of highly-excited trap states, and sets the stage for the future exploration of topological physics in higher dimensions.

4.0.1 Theoretical Overview

To introduce our scheme, let us consider an atomic cloud in a cigar-shaped harmonic trap with trap frequencies $\omega_x = \omega_z \gg \omega_y$. In order to realise the synthetic dimension,

we couple together the atomic trap states of the strong trapping potential along x with the spatially and temporally varying driving potential given by:

$$V_D(x,t) = -V_0\Theta(x\sin(\omega_D t + \varphi)) \tag{4.1}$$

where V_0 is the driving amplitude, $\Theta(x)$ is the Heaviside step function, ω_D is the driving frequency and φ is the initial driving phase. Physically, this corresponds to illuminating the upper half of the atomic cloud with constant power for the first half of the period, $T_D = 2\pi/\omega_D$, before illuminating the lower half with the same constant power over the second half of the period (see Fig. 4.1(a)).

Combining Eq. 4.1 with the 1D harmonic oscillator Hamiltonian along x gives the time-dependent Hamiltonian:

$$\hat{H}(t) = \hbar\omega_x \sum_\lambda \lambda \left|\lambda\right\rangle \left\langle\lambda\right| + V_D(x,t), \tag{4.2}$$

written in the eigenstate basis of the "strong" trap along x, as indexed by $\lambda = 0, 1, 2....$

The stroboscopic dynamics of this system is captured by an effective time-independent Floquet Hamiltonian, which we can approximate over a large number of trap-states by:

$$\hat{\mathcal{H}} \approx \hbar\Delta \sum_\lambda \lambda \left|\lambda\right\rangle \left\langle\lambda\right| + J\sum_\lambda \left[ie^{i\varphi}\left|\lambda+1\right\rangle \left\langle\lambda\right| + \text{h.c}\right] \tag{4.3}$$

where $\Delta \equiv \omega_x - \omega_D$ is the (small) drive detuning and J is a uniform hopping amplitude, which itself depends on V_0 and ω_x and is calculated using Floquet theory. Note that this description is valid for near-resonant driving in a deep harmonic trap, i.e. such that $\omega_x \simeq \omega_D \gg \Delta, J/\hbar$. As depicted in figure 4.1(a), equation 4.3 describes a

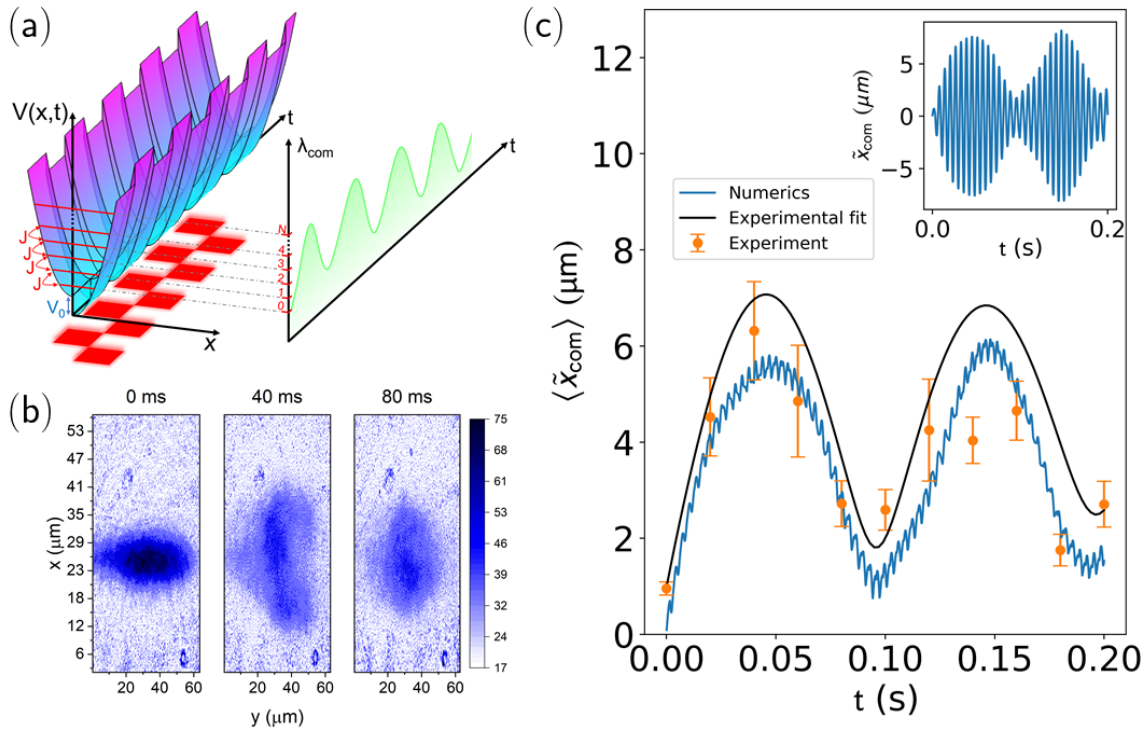


Figure 4.1: **Schematic of the experiment and signatures of the synthetic-dimension Bloch oscillations in real space.** (a): Schematic of the DMD pattern (*red*), which shakes the harmonic trap (*blue/purple*) and couples together nearest-neighbour trap states by inducing Bloch oscillation in the trap states (*green*) (b): Experimentally, the cloud is imaged after a short time-of-flight expansion, as demonstrated here for a detuning of $\Delta = 9.84 \times 2\pi Hz$. The colour scale is the column density in arbitrary units. The full dynamics includes micromotion within each driving period, so the experimental data are averaged over several values of φ. (c): The real-space center-of-mass position, x_{com}, of the atomic cloud is extracted, as shown here for the same data as in (b).

particle hopping between nearest-neighbour sites along a 1D tight-binding lattice with unit spacing in a synthetic dimension. The detuning plays the role of a constant force, $F \equiv -\hbar\Delta$, which therefore can induce Bloch oscillations. Note that the shaking phase φ appears in the effective Hamiltonian as a hopping phase, which we will exploit below to average over unwanted micromotion effects.

In the absence of a force along the synthetic dimension, i.e. when $\Delta = 0$, the effective model in Eq. 4.3 is translationally invariant along the synthetic dimension and has a single energy band in the Brillouin zone. Applying a nonzero force (i.e. $\Delta \neq 0$) accelerates a semiclassical wavepacket formed in the synthetic dimension bulk, such that it undergoes Bloch oscillations across the Brillouin zone, with a center-of-mass (COM) position along the synthetic dimension, λ_{com}, that varies as [13]:

$$\lambda_{\mathrm{com}}(t) = \lambda^0_{\mathrm{com}} + \frac{2J}{\hbar\Delta}(1 - \cos(2\pi f_B t)), \tag{4.4}$$

from the initial position $\lambda_{\mathrm{com}}(t=0) = \lambda^0_{\mathrm{com}}$ and where f_B is the Bloch oscillation frequency. As we can set the spacing between the fictitious synthetic lattice sites equal to one, the periodic Brillouin zone covers $[-\pi, \pi]$. The Bloch oscillation frequency is then set by the magnitude of the applied force divided by the length of this Brillouin zone, i.e. $f_B = |\Delta|/2\pi$, and so is entirely controlled by the detuning. Conversely, the amplitude of the Bloch oscillations is proportional to the bandwidth divided by the force, i.e. $4J/\hbar\Delta$, and so depends on the detuning but also, through J, on the trap frequency and shaking power. The Bloch oscillations therefore provide a way to transport atoms between different trap states, with independent control over both the timescale and number of trap states explored.

4.0.2 Experimental Set Up

In our experimental sequence we load ^{87}Rb atoms from a 3D MOT into a crossed optical dipole trap and then perform forced evaporative cooling [97].The final trapping frequencies are $f_x = f_z \simeq 160Hz$, and $f_y \simeq 10Hz$, where z is the vertical axis, resulting in a cloud elongated along y, with $N \simeq 2 \times 10^4$ atoms at $\simeq 20nK$. The optical setup to realise the dynamical potential and high resolution imaging is described in detail in [98]. In brief, the light produced by a 800nm laser is reflected by a DMD and then sent onto the atoms along the vertical direction, using an optical setup that produces a demagnification of a factor of 100. The DMD is a 2D array of 1920×1080 micromirrors, each with size $10.8\mu m$. Each micromirror can be individually tilted every $100\mu s$, allowing us to produce dynamical optical potentials.The atoms are imaged on a CCD mounted in the vertical direction using a $20\times$ magnifying system with a resolution of $\simeq 2$ μm.

4.1 Experimental Results and Real Space Analysis

Used in the experiment was a rapid evaporation ramp to prevent the sample of atoms described in section 4.0.2 from condensing, thus reducing the effect of mean-field interactions [13], which may complicate the dynamics and will be of interest in future investigations. To realise the driving potential of Eq. 4.1, a digital micromirror device (DMD) that allows dynamic and spatial control the intensity profile of a laser beam with wavelength $800nm$ (see section 4.3.1) is used. It was verified that the trapping and driving potentials are aligned to within $\simeq 1\mu$m. To image the atomic cloud absorption imaging was used, this was done after a very short time-of-flight (TOF) expansion of $t_{\text{tof}} = 5$ms, to increase the visibility of the dynamics. This is demonstrated in figure 4.1(b) for a detuning of $9.84Hz$, where the real space cloud density as a function of time

for an example Bloch oscillation is plotted, showing the cloud COM being displaced away from the origin. Note that the density is averaged over several values of φ in order to reduce the effect of micromotion. As such, the cloud appears to widen along x in time, although the cloud width is actually approximately constant. The initial temperature of $T \simeq 20$nK, corresponds to $\lambda^0_{\rm com} \approx 2$ for an initial Maxwell-Boltzmann distribution of atomic energies. This means that, initially, the atoms start near one "edge" of the synthetic dimension (at $\lambda = 0$), and so atoms must move up the synthetic dimension, irrespective of the sign of the detuning, i.e. the direction of the force. The cloud also does not have a Gaussian distribution with respect to the synthetic dimension as the above semiclassical theory implicitly assumes; nevertheless, in section 4.3.3 (analyitical results) it is shown that the prediction in Eq. 4.4 works well once appropriate corrections are included.

Bloch oscillations in λ-space naturally translate into atomic motion along x in real space, as different harmonic oscillator eigenstates have different real-space profiles. The resulting motion can be seen in figure 4.1(c), where the measured dynamics of the real-space COM position under the action of the shaking potential, as a function of time are displayed. It is important to notice that the full dynamics also includes micromotion within each driving period [13]; for the real-space COM, as shown numerically in the inset of Fig. 4.1(c), the micromotion corresponds to large and fast oscillations as the atoms slosh backwards and forwards in the trap, while the stroboscopic Bloch oscillations translate into variations in the envelope of the dynamics. To isolate the latter, we root-mean-square (RMS) average over different experimental runs with suitably chosen different initial driving phases, φ. The raw cloud images in Fig. 4.1(b) have themselves been averaged in this way. This has the effect of making the cloud appear to widen significantly over the oscillation, although in each single

shot the width is approximately constant. Note that this averaging procedure slightly lowers the apparent amplitude of the motion. However, by reducing the micromotion effects, we can then clearly observe the real-space signatures of the synthetic-dimension Bloch oscillations, seen in 4.1(c) for the same parameters as figure 4.1(b) , where the experimental data is fitted by a function motivated by synthetic-dimension Bloch oscillations (see section 4.3.1, Real-space experimental data analysis). As can be seen, this fit captures the behaviour of the data very well, with agreement between the experiment and numerical simulations (*blue curve*) of a non-interacting 2D thermal cloud (see section 4.3.2 Numerical simulations and data analysis). To account for the fact that the true position of the cloud is not measured due to the TOF expansion, a TOF correction to the cloud centre-of-mass position in our numerical simulations is included.

To further characterise our experimental results, we plot in figure 4.2(a) the values of the oscillation frequency obtained by fitting our data for different detunings. As can be seen, for both experiment and numerics, the frequency increases linearly with detuning, as expected from the analytical Bloch-oscillation frequency (*green line*) given by $f_B = |\Delta|/2\pi$ in both real and synthetic space [c.f. Eq. 4.4]. Note that to avoid systematic errors in the experimental determination of the trapping frequency, this is determined by shifting a linear fit to the measured oscillation frequencies to pass through $(|\Delta|, f) = (0, 0)$.

In figure 4.2(b) it is shown how the amplitude of the real-space motion depends on the detuning by plotting the amplitude fitting parameters. As can be seen, the experiment (*orange/black*) and numerics (*blue*) both clearly show the expected growth in the real-space amplitude as the detuning decreases and higher-excited atomic trap states are explored. To make a quantitative comparison with semi-classical Bloch oscil-

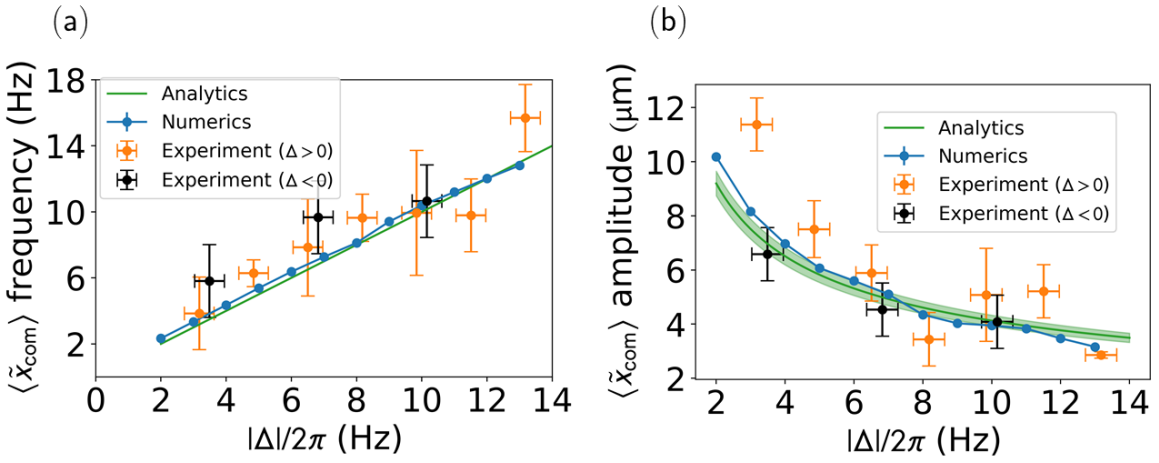


Figure 4.2: **Bloch oscillation frequency and real space amplitude as a function of detuning** (a): Frequency of the Bloch oscillations for the experiment (*orange* for $\Delta > 0$ and *black* for $\Delta < 0$) and for numerics (*blue*). The observed trend is in agreement with the analytical prediction (*green*) of $f_B = |\Delta|/2\pi$ for Bloch oscillations. (b): Amplitude in real space of Bloch oscillations for the same data as plotted in panel (a). The analytical prediction (*green*) shows the expected real-space amplitude as calculated under appropriate approximations from the synthetic-dimension Bloch oscillations, with the green error band calculated from the errors on J and other numerical parameters. The numerical results are obtained by fitting the same function as in experiment to the TOF-corrected, RMS-averaged results like in Fig. 4.1(c). Note that the numerical fit parameters also include error bars, but these are smaller than the data point size. We use the same parameters as Fig. 4.1. Experimental error bars are 1σ statistical errors.

lations (Eq. 4.4), an analytical expression that converts the expected Bloch oscillation amplitude from synthetic space to real space under appropriate assumptions has been derived (seen in a later section), including a correction for the finite fraction of atoms participating in the dynamics, as discussed further below. This analytical prediction is plotted in figure 4.2(b) (*green*), with errors calculated from our numerical parameters. As can be seen, there is agreement between the experiment, numerics and the analytics, demonstrating that good control of the synthetic-dimension Bloch oscillations has been achieved.

Another method of investigation was to look at independently increasing the number of atomic trap states explored (i.e. the Bloch oscillation amplitude) while keeping the oscillation frequency constant, this was done by increasing the shaking power, V_0, and hence the hopping parameter J [c.f. Eq. 4.3]. The dependence of the real-space COM amplitude on V_0 is shown in figure 4.3(a) for a fixed detuning $\Delta = 8.3 \times 2\pi$Hz, while the inset shows the variation of the hopping J, as calculated with Floquet theory. As can be seen, the amplitude in experiment, numerics and analytics all increase as the hopping increases [c.f. Eq. 4.4]. Note that the analytical result is only plotted for $V_0 \leq 4$ nK, as at higher shaking powers, our simple analytical model (Eq. 4.3) breaks down. Despite this, we still observe clear Bloch oscillation dynamics at high power. This is further demonstrated in figure 4.3(b), where we use a very strong potential of $V_0 = 11.96$nK, and still observe the same qualitative trends (i.e. the amplitude decreasing with the detuning and the frequency being equal to the detuning) as in the low power regime.

Finally, the Bloch oscillations can be visualised along the synthetic dimension more directly, by translating our real-space experimental measurements [from figure 4.1(b)] into λ-space, under suitable approximations (see methods section 4.2). These experimental results are plotted in figure 4.4(a) (*orange*), along with numerical simulations (*blue curve*). Note that the latter is not averaged over different initial driving phases; however, in synthetic space, the micromotion is only a fraction of a "lattice spacing" and becomes negligible as the trapping frequency ω_x increases [13].

Comparison of the experimental results with the semi-classical analytical predictions is another source of interest. But can be done by directly comparing the semi-classical analytical predictions [Eq. 4.4] with (*green curve*) and without (*red curve*)

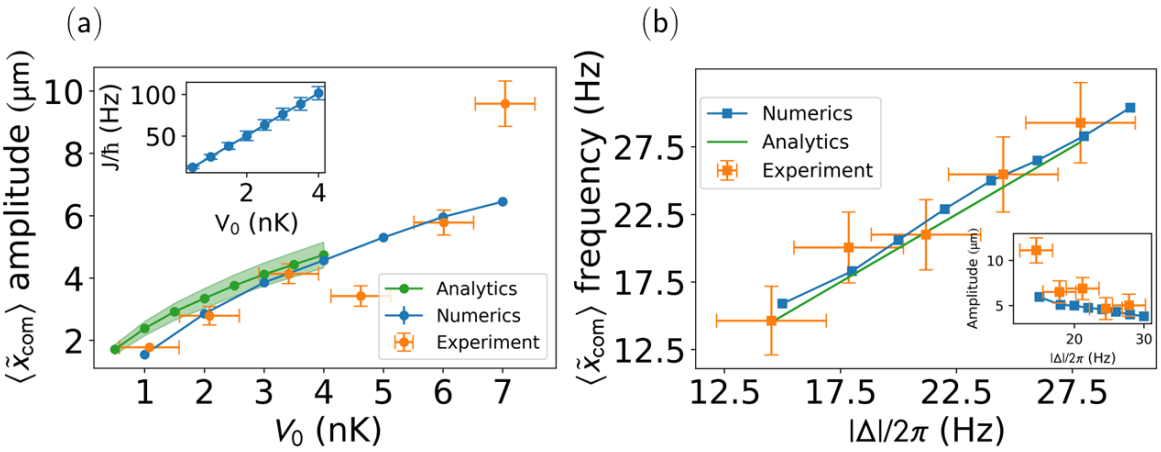


Figure 4.3: **Varying the shaking power to control the dynamics.** (a): The real-space amplitude [c.f figure 4.1(d)] for different shaking powers at a fixed detuning of $\Delta = 8.3 \times 2\pi$Hz, with $\omega_x = 162.6 \times 2\pi$Hz. As can be seen, the experiment (*orange*), numerics (*blue*) and analytics (*green*) increase with the shaking power; this is because, as shown in the inset, the nearest-neighbour hopping amplitude, J, from Floquet theory, increases with V_0 and hence the Bloch-oscillation amplitude along the synthetic dimension increases. Analytics are only shown up to $V_0 = 4$ nK, as at higher shaking potentials the simple nearest-neighbour tight-binding model in Eq. (4.3) is no longer a good description, although the numerics and experiment still appear to exhibit Bloch-oscillation dynamics. This is shown further in (b), where we plot the amplitude fit parameter (inset) and the frequency fit parameter, for $V_0 = 11.96$nK, with $\omega_x = 142.1 \times 2\pi$Hz, $\Delta < 0$, and other parameters as in figure 4.1. Despite the large shaking power, we still observe similar trends to that at low power [c.f. figure 4.1], and still with agreement in panel (b) to the $f_B = |\Delta|/2\pi$ analytical result from the simple tight-binding model. Experimental error bars are 1σ statistical errors. Note that all numerical data points include error bars, but these are smaller than the data points. The green error band on the analytics is calculated from the errors on J and other numerical parameters.

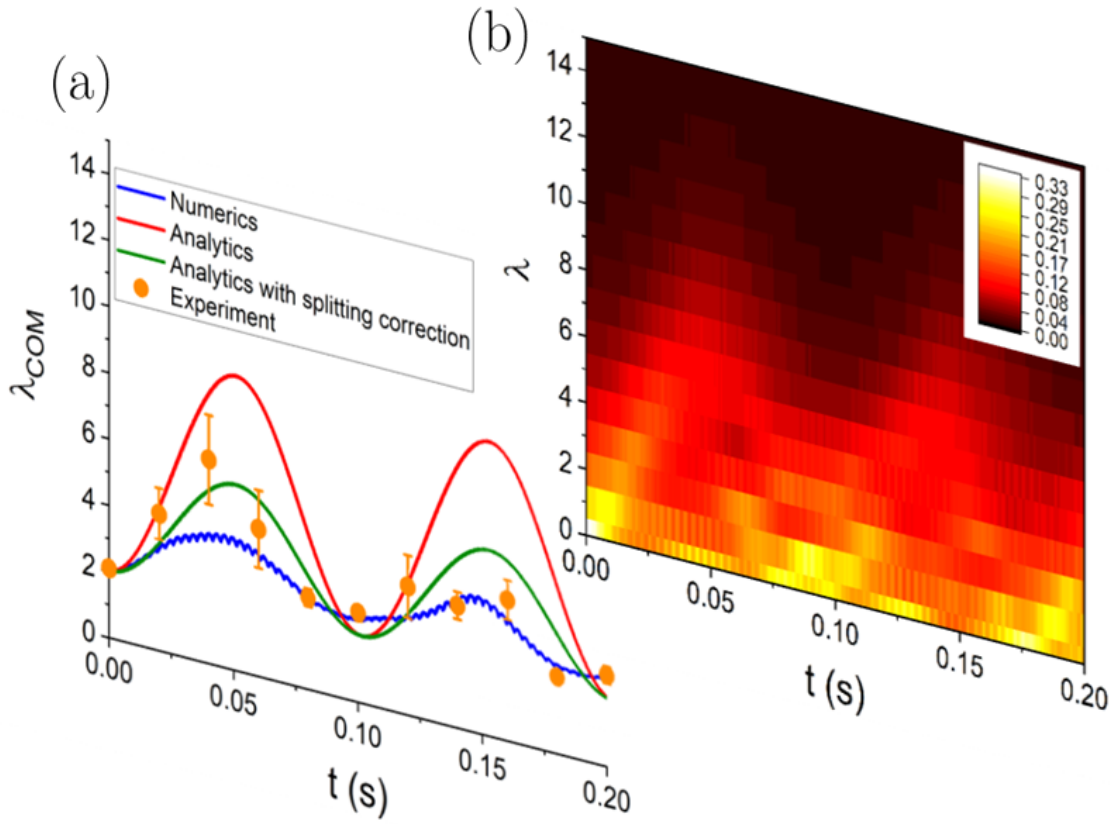


Figure 4.4: **Example Bloch oscillation in synthetic space.** (a): Evolution of the COM, λ_{com}, and the numerical density distribution heatmap along the synthetic dimension (b) for the same data as Fig. 4.1(b), for $\varphi = 0$. Both Bloch oscillations and high-frequency micromotion are visible in the 2D numerics (*blue line*) for a non-interacting thermal cloud. We also convert the corresponding real space experimental data to synthetic space under suitable assumptions (see methods, section 4.2). The observed Bloch oscillation frequency is in good agreement with the 1D analytical semi-classics (Eq. 4.4, *red line*), albeit with a lower amplitude as only around half the atoms from the thermal cloud oscillate along the synthetic dimension [c.f. density distribution heatmap in (b)]. To correct for this, the analytical result is rescaled (*green line*) as discussed in the text. The heatmap shows the numerical atomic density (integrated along the y direction) with respect to λ over the oscillation, showing the cloud-splitting. Both panels use experimental parameters of $\omega_x = 166.5 \times 2\pi$Hz, $\Delta = 2\pi \times 9.84$Hz, $V_0 = 4.16$nK, $T = 20$nK, and $\omega_y = 10 \times 2\pi$Hz. Experimental error bars are 1σ statistical errors.

multiplying by a constant numerical re-scaling factor to account for the fraction of atoms contributing to the dynamics. This correction is used in Fig. 4.1 and 4.3 and is necessary because the COM is skewed downwards by the thermal cloud splitting into two distinct parts, with approximately half of the atoms remaining in low λ-states during the oscillation, as can be seen in the numerical density distribution heat map in Fig. 4.4(b).

Importantly, we can extrapolate how far up λ the oscillating part of the cloud is actually exploring by converting our experimental amplitude fit parameters (Fig. 4.2(b)) to synthetic space and divide by the constant numerical cloud splitting factor. This is plotted in Fig. 4.5 (*orange/black*), where we can see that the fraction of the cloud involved in the Bloch oscillations is moving up several tens of Bloch states, demonstrating that we are creating a very long synthetic dimension. This is supported by our numerical (*blue*) and analytical results (*green*) (see Methods). Note that the number of sites along the synthetic dimension will eventually be limited experimentally by anharmonicities in the trapping potential [13]; however, in this experiment, this does not play an important role.

4.2 Experimental and Theoretical Methods

4.2.1 Real-space Experimental Data Analysis

To reduce micromotion effects, the experimental data for the real-space COM position is RMS-averaged over initial driving phases drawn randomly from $2\pi n/30$, with $n =$

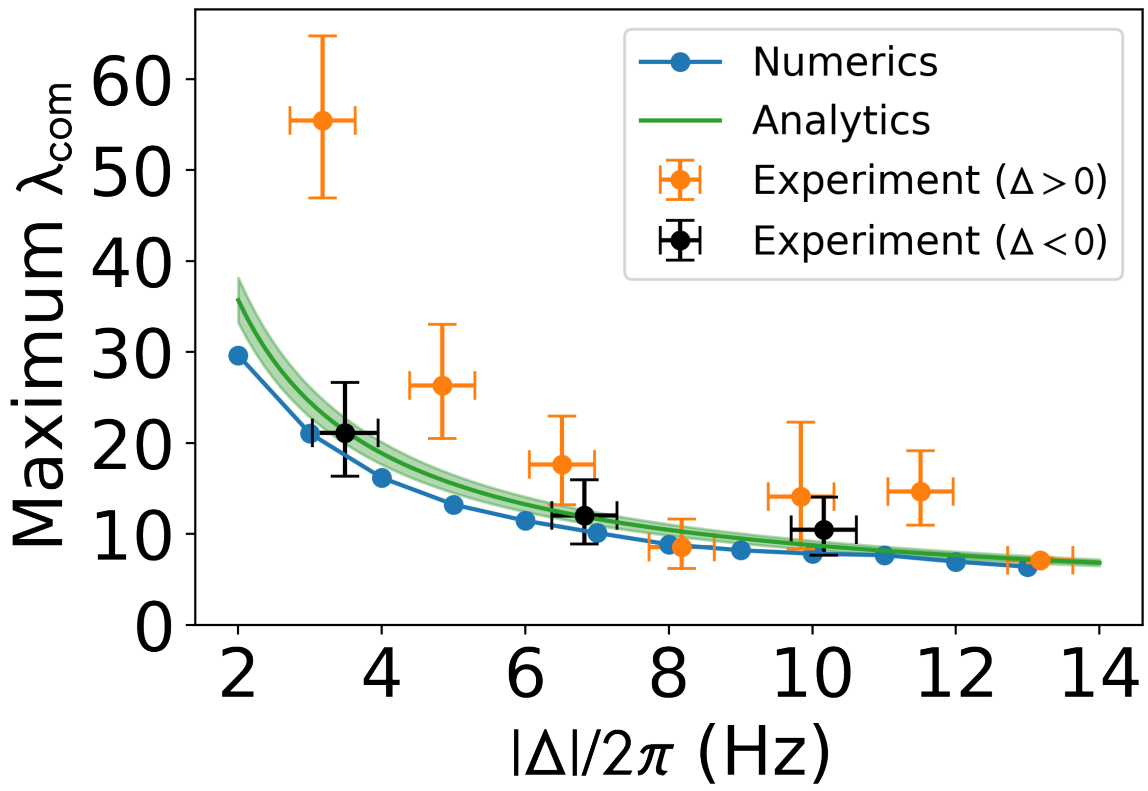


Figure 4.5: **Bloch oscillation amplitude in synthetic space.** The extrapolated maximum value of λ reached by the oscillating part of the cloud as a function of Δ, demonstrating that we have a long, controllable synthetic dimension. We convert the experimental fit parameters in Fig. 4.2(b) to synthetic space (*orange/black*), correcting for cloud splitting. We also plot our numerical maximum λ values (*blue*) for $\varphi = 0$, again corrected for cloud splitting. Furthermore, we derive appropriate analytics (*green*) for comparison. Error bars on experimental points were calculated by converting the real space errors to synthetic space, while the error bars on the analytics were found by propagating errors on J and other numerical parameters. We use experimental parameters of $\omega_x = 166.5 \times 2\pi$Hz, $V_0 = 4.16$nK, $T = 20$nK, and $\omega_y = 10 \times 2\pi$Hz.

$0, 1, ...30$. The resulting data are then fitted to the function:

$$x(t) = A\sqrt{1 - e^{-gt}\cos(2\pi ft + \phi)}, \tag{4.5}$$

where A is the amplitude, f is the frequency, g is a damping factor and ϕ is a phase offset which accounts for random variation in the state preparation. The functional form of this fitting function is motivated by translating the semi-classical prediction for synthetic-dimension Bloch oscillations (Eq. 4.4) into real space. Under certain approximations, this conversion can be achieved by taking:

$$x_{\text{com}} = \sqrt{\lambda_{\text{com}} - \sigma_x^2 + \frac{1}{2}}, \tag{4.6}$$

where x_{com} and σ_x are, respectively, the COM and width of the cloud (in harmonic oscillator lengths) with respect to the real position coordinate, x. Note that in choosing the form of the fitting function, it is assumed that the cloud width σ_x is approximately constant as a function of time, as has also been verified numerically. The fitting parameters f and A are then plotted, for example, in figure 4.1(c) and (d) respectively.

4.2.2 Numerical Simulations and Data Analysis

We perform our simulations by time-evolving an appropriate initial state using the time-dependent Hamiltonian in Eq. 4.2, where we also include weak-trap dynamics (i.e. terms that depend on y). We simulate the dynamics of a non-interacting thermal cloud by using an initial state of the form $|\psi_\theta\rangle = A\sum_{i=0}^{N-1}\sqrt{p_i}\exp(i\theta_i)|\phi_i\rangle$,
where A is a normalisation factor, $p_i = \exp(-\beta E_i)/Z$ is the Boltzmann weight for the i^{th} eigenstate of the 2D harmonic trap $|\phi_i\rangle$ with energy E_i, β is the inverse temperature,

Z is the partition function for the 2D harmonic trap and θ_i is a random phase drawn from a uniform distribution between 0 and 2π. We choose the first N states of the 2D harmonic trap, and we check that the Boltzmann weight is small enough that this is a good approximation. We sequentially generate N' such states, each with a different set of random phases, and then time-evolve each separately. The resulting densities are then averaged together which, reproduces the density of a thermal cloud at $t = 0$.

From numerical simulations that have been done, the cloud density in either synthetic space $\rho(\lambda, y, t)$ or real-space $\rho(x, y, t)$ is obtained. From these densities, calculate the COM position is carried out as a function of time with respect to λ and x respectively. The former is plotted in figure 4.4(a), whilst the latter requires additional processing steps to be compared with experiment. Firstly, to account for the experimental TOF expansion of the cloud, a correction of $x_{\mathrm{com}} \to x_{\mathrm{com}} + v_{\mathrm{com}} t_{\mathrm{tof}}$ is applied, where the COM velocity v_{com} is calculated from the numerical momentum distribution. Secondly, the micromotion is removed by RMS averaging the M different corrected centres-of-mass together: $\langle x_{\mathrm{com}} \rangle = \sqrt{\frac{1}{M} \sum_{i=1}^{M} (x_{\mathrm{com}}^{(i)})^2}$. For the numerics shown in the main text, $M = 2$ is taken with $\varphi = 0$ and $\varphi = \pi/2$. Finally, the data is fit with the experimental fitting function [Eq. 4.5], although now with $\phi = 0$ as numerically there are no random variations in the state preparation. The corresponding fitting parameters f and A for the numerical data are then plotted, for example, in figure 4.1(c) and (d) respectively.

4.2.3 Analytical Results

The semiclassical prediction for synthetic-dimension Bloch oscillations is given by Eq. 4.4. In order to plot this analytical result, the nearest-neighbour hopping $J/\hbar = 106 \pm 8\mathrm{Hz}$ from Floquet theory has been independently calculated. When calculating

this hopping, we observe that the hopping is independent of the detuning, and that each hopping is nearly independent of λ, except for small oscillations. There error bar is therefore calculated by adding the standard deviations of the hopping for each Δ in quadrature. Note that this value applies to our low-power data only; in the high-power case, we have significant long-range hoppings so can no longer use this nearest-neighbour tight binding model. Note also that, in practice, only a fraction of atoms participate in the dynamics, which leads to a significant reduction in the apparent COM position in both synthetic and real space, as shown in Fig. 4.4. To account for this, Eq. 4.4 is modified to $\lambda_{\mathrm{com}}(t) = \lambda^0_{\mathrm{com}} + r\frac{2J}{\hbar\Delta}(1-\cos(\Delta t))$. Here, $r = 0.52 \pm 0.03$ is the average cloud fraction that undergoes the oscillation, as calculated from our numerics for the low power data, where the error bar is the standard deviation of the different r values for different detunings.

To translate the analytical result from synthetic space to real space, the conversion formula [Eq. 4.6] is used under the assumption that the real-space cloud width stays constant as a function of time. This leads to the expression:

$$x_{\mathrm{max}} = \frac{1}{\sqrt{2}}\alpha_{\mathrm{rms}}\alpha_{\mathrm{tof}}\sqrt{\frac{\hbar}{m\omega_x}}\sqrt{\lambda^0_{\mathrm{com}} + r\frac{4J}{\hbar\Delta} - \sigma_x^2 + \frac{1}{2}}. \tag{4.7}$$

where included are corrections for the reduction in amplitude due to RMS averaging, $\alpha_{\mathrm{rms}} = 1/\sqrt{2}$, and for the TOF expansion, $\alpha_{\mathrm{tof}} = 5.25 \pm 0.08$, as calculated from our low-power numerics with an error bar corresponding to the standard deviation across multiple detunings. Note that the cloud width σ_x is here measured in harmonic oscillator lengths $\sqrt{\hbar/m\omega_x}$. This result is then plotted, for example, in figure 4.1(d).

4.2.4 Synthetic-dimension Experimental Data Analysis and Theoretical Results

To convert the real space experimental oscillation into synthetic space (figure 4.4(a)), the conversion formula Eq. 4.6 is used, assuming that the real space width σ_x (measured in harmonic oscillator lengths) remains constant in time and set by the trap frequency and initial temperature. Obtained is:

$$\lambda_{\mathrm{com}}(t) = \left(\frac{x_{\mathrm{com}}(t)}{\alpha_{\mathrm{rms}}\alpha_{tof}}\right)^2 + \sigma_x^2 - \frac{1}{2}, \tag{4.8}$$

where $x_{\mathrm{com}}(t)$ is the experimental real space COM measured in harmonic oscillator lengths. The conversion for the data in figure 4.5 is similar, but here the experimental amplitude fitting parameters are converted, so we use the conversion:

$$\lambda_{\mathrm{com}} = \left(\left(\frac{x_{\mathrm{com}}}{\alpha_{\mathrm{rms}}\alpha_{tof}/\sqrt{2}}\right)^2 + \sigma_x^2 - \frac{1}{2}\right)/r, \tag{4.9}$$

This is then compared against the corresponding numerics, where the maximum value of λ_{com} is extracted and then rescale by $1/r$ to account for the cloud splitting. comparison against an analytical expression, $\lambda_{\mathrm{com}} = \lambda_0 + 4J/\hbar\Delta$, is also done as shown in figure 4.5.

4.3 Creation of Highly-excited Harmonic Oscillator States

Bloch oscillations along the synthetic dimension offer a way to controllably populate highly-excited atomic trap states. Indeed, by stopping the shaking at a certain given

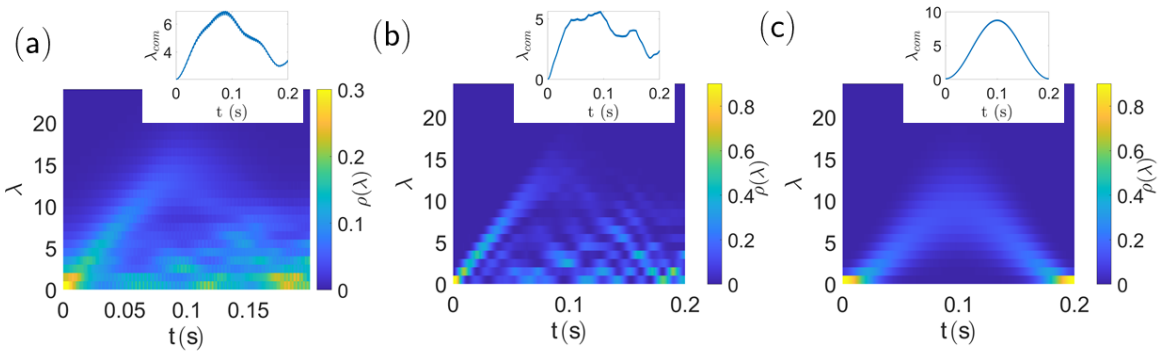


Figure 4.6: **Time evolution of the integrated synthetic space density for a thermal cloud under varying conditions.** (a): Time evolution of the integrated synthetic space density for a thermal cloud under our usual driving potential using typical parameters, for a detuning of $\Delta = 5 \times 2\pi$Hz. We see significant cloud splitting and a relatively wide oscillating component. We use identical parameters to our low-power data elsewhere in this work, with $\varphi = 0$. (b): The result in (a) but with increased trapping frequency and decreased temperature, showing that the oscillating part of the cloud becomes much narrower in synthetic space. Note the different colour scale to (a). We use the same parameters as (a) but with $T = 5$nK and $\omega_x = 2\pi \times 500$Hz. (c): Time evolution of the integrated synthetic space density of a thermal cloud for a modified driving potential, showing that the entire cloud moves, with no split component. Note that the linear driving potential together with parameters as in (a) produces a wide oscillating cloud, so we also increase the trapping frequency and decrease the temperature here to compensate for this. We use: $\kappa x_{\text{qho}} = 1$nK, with $x_{\text{qho}} = \sqrt{\hbar/m\omega_x}$, $\omega_x = 500 \times 2\pi$Hz, $\Delta = 5 \times 2\pi$Hz, $T = 10$nK and $\omega_y = 10 \times 2\pi$Hz. The insets of each panel shows the corresponding λ COM as a function of time. Note that the results for (a) and (b) are not rescaled to take into account cloud splitting.

time it is possible to 'freeze' the dynamics. If this is done when the Bloch oscillation is exploring high λ states, the resulting state will have a considerable admixture of highly-excited harmonic trap states. Figure 4.7 shows an example of states obtained after a 5ms TOF expansion with such a technique with $\Delta/2\pi \simeq 17$Hz, $V_0 \simeq 1.2$nK and stopping the Bloch evolution when the oscillation has reached the peak (40ms) and half way (20ms). By averaging over several different phases of the shaking potential, the whole set of states that can be obtained for a given Bloch evolution time can be reconstructed, this is shown as shaded areas in figure 4.7 (a) and the column density profiles in figure 4.7 (b) and (c). It can be observed that the resulting density pro-

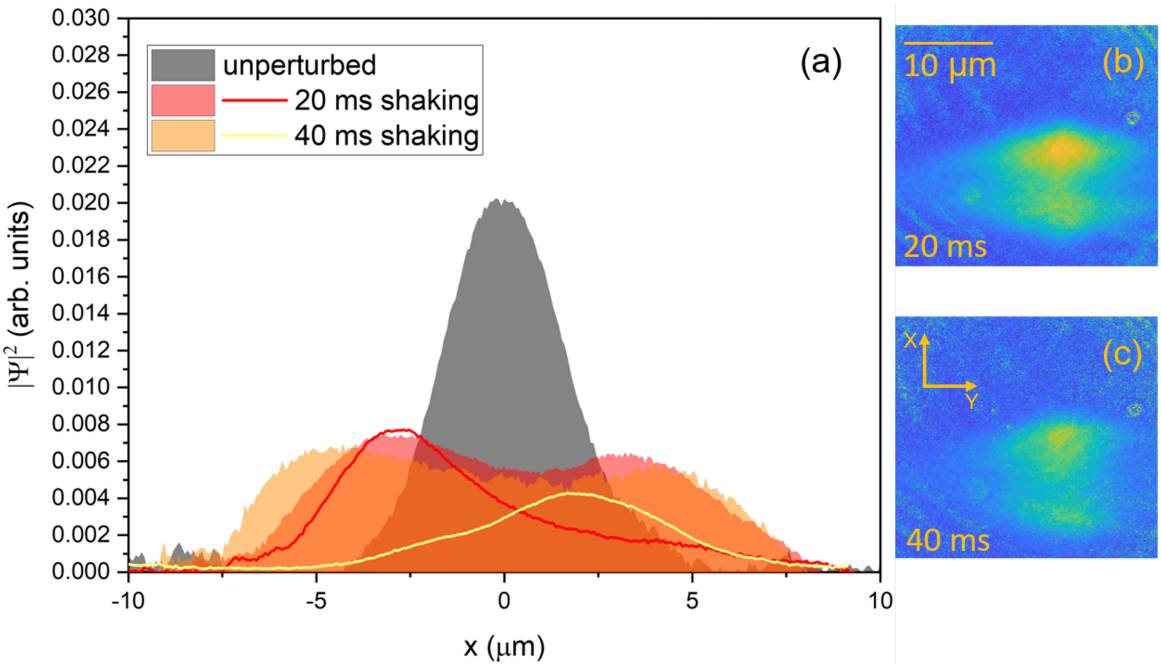


Figure 4.7: **Column density distribution.** (a) Column density distribution integrated along the y direction of our atomic samples after 5 ms of time of flight. The shaded areas correspond to the average of 30 experimental runs where we vary the shaking phase. The solid lines are examples of density distributions that are obtained with fixed phase. The number of atoms is $\simeq 15 \times 10^4$. (b) and (c) are the column densities averaged over 30 runs with different phases in the shaking potential that we observe after 5ms of time of flight and with 20 and 40ms of shaking time respectively.

files acquire the characteristic double-lobe structure typical of highly-excited harmonic trap states. Additionally, as the Bloch dynamics evolve, it can be observed that the distance between the two lobes increases, as expected when populating increasingly higher states. Notably, by controlling the phase of the shaking potential, it is possible to accurately control the shape and position of the final state. This is shown in Fig. 4.7 (a), where the two solid lines correspond to averages over several runs with the same phase both for the 20ms and 40ms cases.

Additionally the lifetime of the states created has been measured by measuring the number of atoms as a function of time after the Bloch evolution is stopped. A decay

time can also be found, setting the lifetime of the state, by performing an exponential decay fit. Concerning the states shown in figure 4.7 in particular, measurements for the lifetime of the states produced after 20ms of shaking potential give a value of $\simeq$1s, while for those produced after 40ms is $\simeq$600ms. Therefore the lifetime of these highly-excited states is sufficiently long to allow one to practically use them. As an example, they would provide a good overlap with a double-well potential enabling new possibilities for trapped atom interferometry [78].

The fidelity of the excited states could be further improved by decreasing the proportion of the cloud that remains in the low-lying λ states, and by decreasing the width with respect to λ of the portion that does oscillate. One approach to achieving this is by a combination of using a stronger trap (i.e. increasing ω_x) and/or a lower temperature, both of which reduce the width of the initial Maxwell-Boltzmann distribution. Figure 4.6(a) and (b) show the synthetic space density profile, with y-dependence integrated out, for a numerical simulation of a thermal cloud with (a) the typical parameters used elsewhere in our work, and (b) a larger trapping frequency and lower temperature, over a single Bloch oscillation period. As can be seen, in panel (b) the part of the cloud that oscillates is narrower with respect to λ than with our more typical parameters in panel (a). Note that, for a small enough temperature, a significant initial condensate fraction may also affect the dynamics. However, we have verified numerically that an initial state with the whole cloud in the $\lambda = 0$ state (i.e. a non-interacting BEC) still undergoes Bloch oscillations under the driving potential.

Also noted is that the width of the oscillating part of the cloud also depends upon the detuning. In figure 4.8, for the low-power parameters used in the previous sections and a detuning of $\Delta/2\pi = 2$Hz (panel (a)) and $\Delta/2\pi = 5$Hz (panel (b)), the density

with respect to λ is shown close to the peak of the oscillation. The oscillating part of the cloud can be seen to have a full-width at half-maximum (FWHM) of around 8 states in (a). This width depends upon the detuning, with larger detunings yielding smaller widths. For example, in panel (b), the FWHM is around 5 states.

Another strategy for improving the fidelity is to optimize the driving potential. As an example, figure 4.6(c) shows the effect of a different driving potential, $V(x,t) = \kappa x \cos(\omega_D t)$, upon a lower-temperature thermal cloud ($T = 10$nK), as calculated numerically using the technique described in Section I. Note that this driving potential is the same as that of [13] (see Eq. 2 therein). As can be seen, the entire cloud undergoes the Bloch oscillation, with no split component. This difference is likely because for the experimental driving potential, there are oscillations in the Floquet Hamiltonian matrix elements at low λ, which include, for example, an effective potential minimum at $\lambda = 0$ which may trap some atoms, leading to the cloud splitting. For the linear driving potential, on the other hand, the Floquet Hamiltonian does not exhibit such oscillations, although there is then a strong λ-dependence in the hopping elements [13]. Going further, quantum control approaches could be used to further numerically optimize the driving potential, in order to improve the fidelity of desired state preparation.

Finally, another possible strategy for improving the fidelity of excited states would be to employ a two-step protocol. Firstly, the cloud could be placed into an excited trap state without using the driving potential [74]. Secondly, the driving potential could be activated, causing Bloch oscillations in the synthetic dimension bulk.

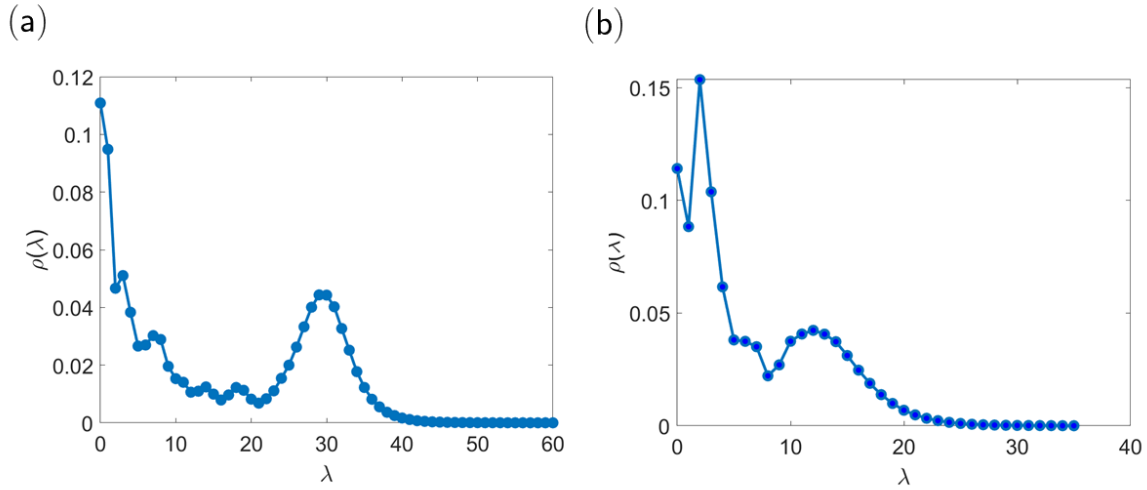


Figure 4.8: **Cloud density** with respect to λ for the low power parameters used in the Main Text and a detuning of $\Delta/2\pi = 2$Hz (panel (a)) and $\Delta/2\pi = 5$Hz (panel (b)). The density is extracted from close to the peak of the oscillation. We clearly see the oscillating part of the cloud, which has a full-width at half-maximum of around 8 states in (a) and around 5 states in (b).

Chapter 5

Conclusion

This thesis starts by presenting introductory material and basic principles relevant to the key work carried out and achieved. Starting with a summary of optical potentials, as potentials are a core part of the experiment for the use in simulations and atom manipulation. Following this, an introduction and motivation for both the work on dynamic high quality optical potentials and synthetic dimensions is presented. Key material included in the first part of this is a comparison of the three light sources, laser, LED and SLD, and how the DMD operates. In the second part a description of key concepts such as what a synthetic dimension is and how we have interpreted it in our system and how this work fits into other work in the field. The following chapter gives an overview of the core experiment, including what has been recently developed. This includes a description of the vacuum and laser systems, in addition to the more specific details including the imaging system, the flat trap, the DMD and an overview of the differences between possible light sources used for the creation of optical potentials. This is subsequently followed by the specific experimental setups and results achieved for both published and pre-published pieces of research carried out. "Generation of optical potentials for ultracold atoms using a superluminescent

diode" and "Bloch Oscillations Along a Synthetic Dimension of Atomic Trap States", the conclusions of which are copied and included in this conclusion.

In the research carried out for "Generation of optical potentials for ultracold atoms using a superluminescent diode" we investigated the use of a SLD in combination with a DMD to produce optical potentials for ultracold atoms. We have compared the ability of a SLD and a laser to produce regular square-wave gratings with different periodicity. We have shown that by using a SLD we consistently obtain images with higher fidelity than and comparable contrast to a laser, resulting in an overall superior quality over the whole range of parameters explored. We have used the patterns generated with the SLD to produce arbitrary 1D disordered potential for our ultracold atoms. This has resulted in patterned atomic densities that nicely retrace the optical potential. We have further demonstrated the implementation of dynamical 1D potentials with our system. Notably, the setup studied here is simple, robust, cost-effective, and as such, can easily find application in many ultracold atoms experiments worldwide. Additionally, SLDs are available in the near infrared and across most of the visible spectrum, making them suitable for a wide range of possible applications in quantum technology.

In the research carried out for "Bloch Oscillations Along a Synthetic Dimension of Atomic Trap States", we investigated the creation of long synthetic dimensions in ultra cold atoms using a combination of laser light and DMD to create the moving potentials. Our experimental results show that we have engineered a synthetic dimension of atomic trap states by projecting a time-dependent shaking potential onto an atomic cloud via a digital micro-mirror device. Through control of the shaking potential's detuning, we induced Bloch oscillations along the synthetic dimension, observing the key characteristics of these dynamics in the real-space motion of the cloud. Our ex-

periment demonstrates that a long and controllable synthetic dimension can be created.

The results in chapter 3 of this thesis can open new avenues in the study of 1D disordered systems and transport phenomena in 1D. The extension to two-dimensional patterns in combination with a flat trap could be relevant for applications in atomtronics, phase imprinting and quantum simulations experiments. The further extension to three-dimensional patterns using two or more DMDs has the potential of enabling more pristine control in quantum simulators. The results in chapter 4 open up the way towards the exploration of topological physics using a synthetic dimension of harmonic trap states [13, 71]. The spatio-temporal control of the shaking potential can also allow for future investigations of phenomena such as magnetic barriers, as well as the controlled population of excited atomic trap states.

The apparatus used creates a very versatile quantum simulation experiment, with a large capacity to grow and change. The experiment for now has immediate goals and long term goals. With regards to the synthetic dimensions project, we are now working to control the number of states accessed with the implementation of a barrier around the sample, with the aim of investigating the Quantum Hall effect.

With regards to the more traditional quantum simulations carried out on this experiment, one active aim is looking into the superfluid fountain effect within a BEC. Initial attempts were carried out to try and replicate the effects of the superfluid fountain within the superfluid that is the BEC. The superfluid fountain effect is typically demonstrated in superfluid helium where the superfluid component part of the fluid flows towards a heat source. It is a unique property of superfluids that has not been observed in a BEC to date, but theoretical works have predicted its existence [99]. Also

a project is ongoing looking at turbulence in BEC with phase imprinted vortices, this is in the simulation stages and should be experimentally realised in the future. Both of these are low energy physics simulations, we also have high energy physics simulations to carry out. Leading on from the implementation of the imprinting of vortices the aim is to study the Andreev Bashkin effect in neutron stars. A key property of superfluids is that they are frictionless, however there is friction/disipationless drag between different types of superfluid. In neutron stars there is a layer of protons and a layer of neutrons, both in superfluid state, this drag gives rise to some of the more extreme properties of neutron stars, such as in pulsars [100]. This drag is very difficult to experimentally measure, and our system could provide a method to do so. In the spinor BEC that the experiment creates, the condensate consists of three states of superfluid (-1, 0, +1 spin states), the components can be separated with a Stern-Gerlach pulse, individually have a vortex imprinted onto at least two of them, and recombined. This dissipationless drag will be observed and measurable by looking at the interaction between the two vortices after recombination of the atom samples. The vortices only interact with one another through this drag, otherwise they would be invisible to each another [101]. Another high energy physics simulation experiment that can be carried out and is also starting to be looked at is studying analogue black holes [102]. This would involve a simple adaption of the current setup, however stability would need to be improved, as seen in [102], as large volumes of data are needed. This experiment involves studying density fluctuations within the BEC whilst moving a light potential through the BEC at faster than the speed of sound. These active and future experiments are some of many that this extremely versatile quantum simulations experiment is potentially capable of investigating.

Bibliography

[1] Andrew D. Ludlow et al. *Optical Atomic Clocks*. 2014. DOI: 10.48550/ARXIV.1407.3493. URL: https://arxiv.org/abs/1407.3493.

[2] E. L. Raab et al. "Trapping of Neutral Sodium Atoms with Radiation Pressure". In: *Phys. Rev. Lett.* 59 (23 Dec. 1987), pp. 2631–2634. DOI: 10.1103/PhysRevLett.59.2631. URL: https://link.aps.org/doi/10.1103/PhysRevLett.59.2631.

[3] M. H. Anderson et al. "Observation of Bose-Einstein Condensation in a Dilute Atomic Vapor". In: *Science* 269.5221 (1995), pp. 198–201. DOI: 10.1126/science.269.5221.198. eprint: https://www.science.org/doi/pdf/10.1126/science.269.5221.198. URL: https://www.science.org/doi/abs/10.1126/science.269.5221.198.

[4] Anand Ramanathan et al. "Superflow in a Toroidal Bose-Einstein Condensate: An Atom Circuit with a Tunable Weak Link". In: *Physical review letters* 106 (Apr. 2011), p. 130401. DOI: 10.1103/PHYSREVLETT.106.130401.

[5] L. Amico et al. "Roadmap on Atomtronics: State of the art and perspective". In: *AVS Quantum Science* 3.039201 (2021). DOI: https://doi.org/10.1116/5.0026178. URL: https://avs.scitation.org/doi/full/10.1116/5.0026178.

[6] Daniel Barredo et al. "An atom-by-atom assembler of defect-free arbitrary two-dimensional atomic arrays". In: *Science* 354.6315 (2016), pp. 1021–1023. DOI: 10.1126/science.aah3778. eprint: https://www.science.org/doi/pdf/10.1126/science.aah3778. URL: https://www.science.org/doi/abs/10.1126/science.aah3778.

[7] Barredo. D., Lienhard. V., and de Léséleuc. S. et al. "Synthetic three-dimensional atomic structures assembled atom by atom." In: *Nature* 561 (2018), pp. 79–82. DOI: https://doi.org/10.1038/s41586-018-0450-2. URL: https://www.nature.com/articles/s41586-018-0450-2.

[8] Daniel Ohl de Mello et al. "Defect-Free Assembly of 2D Clusters of More Than 100 Single-Atom Quantum Systems". In: *Phys. Rev. Lett.* 122 (20 May 2019), p. 203601. DOI: 10.1103/PhysRevLett.122.203601. URL: https://link.aps.org/doi/10.1103/PhysRevLett.122.203601.

[9] Kim. H., W. Lee, and Lee. Hg. et al. "In situ single-atom array synthesis using dynamic holographic optical tweezers." In: *Nature Comm* (7 2016), p. 13317. DOI: https://doi.org/10.1038/ncomms13317. URL: https://www.nature.com/articles/ncomms13317.

[10] D. Barredo et al. "Three-Dimensional Trapping of Individual Rydberg Atoms in Ponderomotive Bottle Beam Traps". In: *Phys. Rev. Lett.* 124 (2 Jan. 2020), p. 023201. DOI: 10.1103/PhysRevLett.124.023201. URL: https://link.aps.org/doi/10.1103/PhysRevLett.124.023201.

[11] Toshiya Kinoshita, Trevor Wenger, and David S. Weiss. "All-optical Bose-Einstein condensation using a compressible crossed dipole trap". In: *Phys. Rev. A* 71 (1 Jan. 2005), p. 011602. DOI: 10.1103/PhysRevA.71.011602. URL: https://link.aps.org/doi/10.1103/PhysRevA.71.011602.

[12] K Henderson et al. "Experimental demonstration of painting arbitrary and dynamic potentials for Bose–Einstein condensates". In: *New Journal of Physics* 11.4 (Apr. 2009), p. 043030. DOI: 10.1088/1367-2630/11/4/043030. URL: https://dx.doi.org/10.1088/1367-2630/11/4/043030.

[13] Hannah M. Price, Tomoki Ozawa, and Nathan Goldman. "Synthetic dimensions for cold atoms from shaking a harmonic trap". In: *Phys. Rev. A* 95 (2 Feb. 2017), p. 023607. DOI: 10.1103/PhysRevA.95.023607. URL: https://link.aps.org/doi/10.1103/PhysRevA.95.023607.

[14] Wang. Y., Shevate. S., and Wintermantel. T.M. et al. "Preparation of hundreds of microscopic atomic ensembles in optical tweezer arrays." In: *npj Quantum Inf* 6.54 (June 2020). DOI: https://doi.org/10.1038/s41534-020-0285-1. URL: https://www.nature.com/articles/s41534-020-0285-1.

[15] Pavel Ruchka et al. "Microscopic 3D printed optical tweezers for atomic quantum technology". In: *Quantum Science and Technology* 7.4 (July 2022), p. 045011. DOI: 10.1088/2058-9565/ac796c. URL: https://dx.doi.org/10.1088/2058-9565/ac796c.

[16] R V Brooks et al. "Preparation of one 87Rb and one 133Cs atom in a single optical tweezer". In: *New Journal of Physics* 23.6 (June 2021), p. 065002. DOI: 10.1088/1367-2630/ac0000. URL: https://dx.doi.org/10.1088/1367-2630/ac0000.

[17] Rudolf Grimm, Matthias Weidemüller, and Yurii B. Ovchinnikov. "Optical Dipole Traps for Neutral Atoms". In: ed. by Benjamin Bederson and Herbert Walther. Vol. 42. Advances In Atomic, Molecular, and Optical Physics. Academic Press, 2000, pp. 95–170. DOI: https://doi.org/10.1016/S1049-250X(08)60186-X. URL: https://www.sciencedirect.com/science/article/pii/S1049250X0860186X.

[18] Leon Karpa. "Optical Dipole Traps for Single Ions". In: *Trapping Single Ions and Coulomb Crystals with Light Fields*. Cham: Springer International Publishing, 2019, pp. 21–29. ISBN: 978-3-030-27716-1. DOI: 10.1007/978-3-030-27716-1_3. URL: https://doi.org/10.1007/978-3-030-27716-1_3.

[19] Avinash Kumar et al. "Minimally destructive, Doppler measurement of a quantized flow in a ring-shaped Bose–Einstein condensate". In: *New Journal of Physics* 18 (Feb. 2016). DOI: 10.1088/1367-2630/18/2/025001.

[20] D. Sheng, J. Zhang, and L. A. Orozco. "Rb atoms in a blue-detuned dipole trap: Coherence and ground-state differential ac Stark shift". In: *Phys. Rev. A* 87 (6 June 2013), p. 063412. DOI: 10.1103/PhysRevA.87.063412. URL: https://link.aps.org/doi/10.1103/PhysRevA.87.063412.

[21] Rudolf Grimm, Matthias Weidemüller, and Yuri Ovchinnikov. "Optical Dipole Traps for Neutral Atoms". In: *Advances in Atomic, Molecular, and Optical Physics* 42 (Dec. 2000), p. 95. DOI: 10.1016/S1049-250X(08)60186-X.

[22] Martin J. Booth et al. "Adaptive aberration correction in a confocal microscope". In: *Proceedings of the National Academy of Sciences* 99.9 (2002), pp. 5788–5792. DOI: 10.1073/pnas.082544799. eprint: https://www.pnas.org/doi/pdf/10.1073/pnas.082544799. URL: https://www.pnas.org/doi/abs/10.1073/pnas.082544799.

[23] A. Jesacher et al. "Wavefront correction of spatial light modulators using an optical vortex image". In: *Opt. Express* 15.9 (Apr. 2007), pp. 5801–5808. DOI: 10.1364/OE.15.005801. URL: https://opg.optica.org/oe/abstract.cfm?URI=oe-15-9-5801.

[24] I.M. Vellekoop and A.P. Mosk. "Phase control algorithms for focusing light through turbid media". In: *Optics Communications* 281.11 (2008), pp. 3071–

3080. ISSN: 0030-4018. DOI: https://doi.org/10.1016/j.optcom.2008.02.022. URL: https://www.sciencedirect.com/science/article/pii/S0030401808001430.

[25] S. M. Popoff et al. "Measuring the Transmission Matrix in Optics: An Approach to the Study and Control of Light Propagation in Disordered Media". In: *Phys. Rev. Lett.* 104 (10 Mar. 2010), p. 100601. DOI: 10.1103/PhysRevLett.104.100601. URL: https://link.aps.org/doi/10.1103/PhysRevLett.104.100601.

[26] Čižmár. T, Mazilu. M, and Dholakia. K. "In situ wavefront correction and its application to micromanipulation." In: *Nature Photon* 4 (May 2010), pp. 388–394. DOI: https://doi.org/10.1038/nphoton.2010.85. URL: https://www.nature.com/articles/nphoton.2010.85.

[27] Mosk. A, Lagendijk. A, and Lerosey. G et al. "controlling waves in space and time for imaging and focusing in complex media." In: *Nature Photon* 4 (May 2012), pp. 283–292. DOI: https://doi.org/10.1038/nphoton.2012.88. URL: https://www.nature.com/articles/nphoton.2012.88.

[28] Roberto Di Leonardo and Silvio Bianchi. "Hologram transmission through multimode optical fibers". In: *Opt. Express* 19.1 (Jan. 2011), pp. 247–254. DOI: 10.1364/OE.19.000247. URL: https://opg.optica.org/oe/abstract.cfm?URI=oe-19-1-247.

[29] Čižmár. T and Dholakia. K. "Exploiting multimode waveguides for pure fibre-based imaging." In: *Nature Photon* 3 (May 2012), p. 1027. DOI: https://doi.org/10.1038/ncomms2024. URL: https://www.nature.com/articles/ncomms2024.

[30] Sergey Turtaev et al. "Comparison of nematic liquid-crystal and DMD based spatial light modulation in complex photonics". In: *Opt. Express* 25.24 (Nov. 2017), pp. 29874–29884. DOI: 10.1364/OE.25.029874. URL: https://opg.optica.org/oe/abstract.cfm?URI=oe-25-24-29874.

[31] Immanuel Bloch, Jean Dalibard, and Wilhelm Zwerger. "Many-body physics with ultracold gases". In: *Rev. Mod. Phys.* 80 (3 July 2008), pp. 885–964. DOI: 10.1103/RevModPhys.80.885. URL: https://link.aps.org/doi/10.1103/RevModPhys.80.885.

[32] I. M. Georgescu, S. Ashhab, and Franco Nori. "Quantum simulation". In: *Rev. Mod. Phys.* 86 (1 Mar. 2014), pp. 153–185. DOI: 10.1103/RevModPhys.86.153. URL: https://link.aps.org/doi/10.1103/RevModPhys.86.153.

[33] Juliette Billy et al. "Direct observation of Anderson localization of matter waves in a controlled disorder". In: *Nature* 453.7197 (2008), pp. 891–894. DOI: 10.1038/nature07000.

[34] G. Roati, C. D'Errico, L. Fallani, et al. "Anderson localization of a non-interacting Bose–Einstein condensate." In: *Nature* 453 (2008), pp. 895–898. DOI: https://doi.org/10.1038/nature07071.

[35] B. Paredes, A. Widera, V. Murg, et al. "Tonks–Girardeau gas of ultracold atoms in an optical lattice." In: *Nature* 429 (May 2004), pp. 277–281. DOI: 10.1038/nature02530. URL: https://www.nature.com/articles/nature02530.

[36] Y.J. Lin, R. Compton, K. Jiménez-García, et al. "Synthetic magnetic fields for ultracold neutral atoms." In: *Nature* 462 (Dec. 2009), pp. 628–632. DOI: 10.1038/nature08609. URL: https://www.nature.com/articles/nature08609.

[37] M. Mancini et al. "Observation of chiral edge states with neutral fermions in synthetic Hall ribbons". In: *Science* 349.6255 (2015), pp. 1510–1513. ISSN: 0036-8075. DOI: 10.1126/science.aaa8736.

[38] Manuel Endres et al. "The 'Higgs' amplitude mode at the two-dimensional superfluid/Mott insulator transition". In: *Nature* 487.7408 (2012), pp. 454–458. DOI: 10.1038/nature11255.

[39] J. Steinhauer. "Observation of self-amplifying Hawking radiation in an analogue black-hole laser." In: *Nature Phys* 10 (Oct. 2014), pp. 864–869. DOI: 10.1038/nphys3104. URL: https://www.nature.com/articles/nphys3104.

[40] N. R. Cooper, J. Dalibard, and I. B. Spielman. "Topological bands for ultracold atoms". In: *Rev. Mod. Phys.* 91 (1 Mar. 2019), p. 015005. DOI: 10.1103/RevModPhys.91.015005. URL: https://link.aps.org/doi/10.1103/RevModPhys.91.015005.

[41] I. Bloch, J. Dalibard, and S. Nascimbene. "Quantum simulations with ultracold quantum gases". In: *Nature Physics* 8 (2012), pp. 267–276. DOI: https://doi.org/10.1038/nphys2259.

[42] C. Gross and I. Bloch. "Quantum simulations with ultracold atoms in optical lattices". In: *Science* 357 (2017), pp. 995–1001. DOI: 10.1126/science.aal3837.

[43] F. Schaefer, T. Fukuhara, S. Sugawa, et al. "Tools for quantum simulations with ultracold atoms in optical lattices". In: *Nature Reviews Physics* 2 (2020), pp. 411–425. DOI: https://doi.org/10.1038/s42254-020-0195-3.

[44] Alexander L. Gaunt et al. "Bose-Einstein Condensation of Atoms in a Uniform Potential". In: *Phys. Rev. Lett.* 110 (20 May 2013), p. 200406. DOI: 10.1103/PhysRevLett.110.200406. URL: https://link.aps.org/doi/10.1103/PhysRevLett.110.200406.

[45] K Henderson et al. "Experimental demonstration of painting arbitrary and dynamic potentials for Bose–Einstein condensates". In: *New Journal of Physics* 11.4 (Apr. 2009), p. 043030. DOI: 10.1088/1367-2630/11/4/043030. URL: https://doi.org/10.1088/1367-2630/11/4/043030.

[46] G. Gauthier et al. "Direct imaging of a digital-micromirror device for configurable microscopic optical potentials". In: *Optica* 3.10 (Oct. 2016), pp. 1136–1143. DOI: 10.1364/OPTICA.3.001136. URL: http://www.osapublishing.org/optica/abstract.cfm?URI=optica-3-10-1136.

[47] Philip Zupancic et al. "Ultra-precise holographic beam shaping for microscopic quantum control". In: *Opt. Express* 24.13 (June 2016), pp. 13881–13893. DOI: 10.1364/OE.24.013881. URL: http://www.opticsexpress.org/abstract.cfm?URI=oe-24-13-13881.

[48] Nadine Meyer et al. "Observation of Two-Dimensional Localized Jones-Roberts Solitons in Bose-Einstein Condensates". In: *Physical Review Letters* 119.15 (2017). DOI: 10.1103/physrevlett.119.150403.

[49] H. Rubinsztein-Dunlop et al. "Roadmap on structured light." In: *J. Opt.* 19 (2017), p. 013001. DOI: http://dx.doi.org/10.1088/2040-8978/19/1/013001.

[50] L.Amico et al. "Roadmap on Atomtronics: State of the art and perspective". In: *arXiv:2008.04439* (2020).

[51] W. J. Kwon et al. "Strongly correlated superfluid order parameters from dc Josephson supercurrents". In: *Science* 369.6499 (2020), pp. 84–88. DOI: 10.1126/science.aaz2463.

[52] N.K. Dutta and P.P. Deimel. "Optical Properties of a GaAlAs Superluminescent Diode." In: *IEEE J. quantum Electron* 19 (1983), pp. 496–498. DOI: 10.1109/JQE.1983.1071888.

[53] G.A. Alphonse et al. "High-power superluminescent diodes." In: *J. Opt.* 24 (1988), pp. 2454–2457. DOI: http://dx.doi.org/10.1109/3.14376.

[54] C. K. Hitzenberger et al. "Measurement of the spatial coherence of superluminescent diodes". In: *Journal of Modern Optics* 46.12 (1999), pp. 1763–1774. DOI: 10.1080/09500349908231370.

[55] M. R. Matthews et al. "Vortices in a Bose-Einstein Condensate". In: *Phys. Rev. Lett.* 83 (13 Sept. 1999), pp. 2498–2501. DOI: 10.1103/PhysRevLett.83.2498. URL: https://link.aps.org/doi/10.1103/PhysRevLett.83.2498.

[56] G. Cappellini M. Mancini G. Pagano et al. "Observation of chiral edge states with neutral fermions in synthetic Hall ribbons". In: *Science* 349 (6255 Sept. 2015), pp. 1510–1513. DOI: 10.1126/science.aaa8736. URL: https://www.science.org/doi/abs/10.1126/science.aaa8736.

[57] B. K. Stuhl et al. "Visualizing edge states with an atomic Bose gas in the quantum Hall regime". In: *Science* 349 (6255 Sept. 2015), pp. 1514–1518. DOI: 10.1126/science.aaa8515. URL: https://www.science.org/doi/abs/10.1126/science.aaa8515.

[58] F. An E. Meier and B. Gadway. "Observation of the topological soliton state in the Su–Schrieffer–Heeger model". In: *Nature Communications* y (13986 Dec. 2016), pp. 1017–1021. DOI: https://doi.org/10.1038/ncomms13986. URL: https://www.nature.com/articles/ncomms13986.

[59] Kai Wang et al. "Generating arbitrary topological windings of a non-Hermitian band". In: *Science* 371.6535 (2021), pp. 1240–1245. DOI: 10.1126/science.abf6568. eprint: https://www.science.org/doi/pdf/10.1126/science.abf6568. URL: https://www.science.org/doi/abs/10.1126/science.abf6568.

[60] Eric J. Meier et al. "Observation of the topological Anderson insulator in disordered atomic wires". In: *Science* 362.6417 (2018), pp. 929–933. DOI: 10.1126/science.aat3406. eprint: https://www.science.org/doi/pdf/10.1126/science.aat3406. URL: https://www.science.org/doi/abs/10.1126/science.aat3406.

[61] Konrad Viebahn et al. "Matter-Wave Diffraction from a Quasicrystalline Optical Lattice". In: *Phys. Rev. Lett.* 122 (11 Mar. 2019), p. 110404. DOI: 10.1103/PhysRevLett.122.110404. URL: https://link.aps.org/doi/10.1103/PhysRevLett.122.110404.

[62] O. Boada et al. "Quantum Simulation of an Extra Dimension". In: *Phys. Rev. Lett.* 108 (13 Mar. 2012), p. 133001. DOI: 10.1103/PhysRevLett.108.133001. URL: https://link.aps.org/doi/10.1103/PhysRevLett.108.133001.

[63] H. M. Price et al. "Four-Dimensional Quantum Hall Effect with Ultracold Atoms". In: *Phys. Rev. Lett.* 115 (19 Nov. 2015), p. 195303. DOI: 10.1103/PhysRevLett.115.195303. URL: https://link.aps.org/doi/10.1103/PhysRevLett.115.195303.

[64] T. Chalopin et al. "Probing chiral edge dynamics and bulk topology of a synthetic Hall system". In: *Nature physics* 16 (June 2020), pp. 1017–1021. DOI: https://doi.org/10.1038/s41567-020-0942-5. URL: https://www.nature.com/articles/s41567-020-0942-5.

[65] Vincent Lienhard et al. "Realization of a Density-Dependent Peierls Phase in a Synthetic, Spin-Orbit Coupled Rydberg System". In: *Phys. Rev. X* 10 (2 May 2020), p. 021031. DOI: 10.1103/PhysRevX.10.021031. URL: https://link.aps.org/doi/10.1103/PhysRevX.10.021031.

[66] S. K. Kanungo et al. "Realizing Su-Schrieffer-Heeger topological edge states in Rydberg-atom synthetic dimensions". In: *arXiv:2101.02871* (Jan. 2021). DOI: https://doi.org/10.48550/arXiv.2101.02871. URL: https://arxiv.org/abs/2101.02871.

[67] L. F. Livi et al. "Synthetic Dimensions and Spin-Orbit Coupling with an Optical Clock Transition". In: *Phys. Rev. Lett.* 117 (22 Nov. 2016), p. 220401. DOI: 10.1103/PhysRevLett.117.220401. URL: https://link.aps.org/doi/10.1103/PhysRevLett.117.220401.

[68] S. Kolkowitz et al. "Spin–orbit-coupled fermions in an optical lattice clock". In: *Nature* 542 (Dec. 2017), pp. 66–70. DOI: https://doi.org/10.1038/nature20811. URL: https://www.nature.com/articles/nature20811#citeas.

[69] Jin Hyoun Kang, Jeong Ho Han, and Y Shin. "Creutz ladder in a resonantly shaken 1D optical lattice". In: *New Journal of Physics* 22.1 (Jan. 2020), p. 013023. DOI: 10.1088/1367-2630/ab61d7. URL: https://dx.doi.org/10.1088/1367-2630/ab61d7.

[70] Han Cai et al. "Experimental Observation of Momentum-Space Chiral Edge Currents in Room-Temperature Atoms". In: *Phys. Rev. Lett.* 122 (2 Jan. 2019), p. 023601. DOI: 10.1103/PhysRevLett.122.023601. URL: https://link.aps.org/doi/10.1103/PhysRevLett.122.023601.

[71] G. Salerno et al. "Quantized Hall Conductance of a Single Atomic Wire: A Proposal Based on Synthetic Dimensions". In: *Phys. Rev. X* 9 (4 Oct. 2019), p. 041001. DOI: 10.1103/PhysRevX.9.041001. URL: https://link.aps.org/doi/10.1103/PhysRevX.9.041001.

[72] E. Lustig et al. "Photonic topological insulator in synthetic dimensions". In: *Nature* 567 (7748 Mar. 2019), pp. 356–360. DOI: 10.1038/s41586-019-0943-7. URL: https://doi.org/10.1038/s41586-019-0943-7.

[73] Wirth. G., Ölschläger. M, and Hemmerich. A. "Evidence for orbital superfluidity in the P-band of a bipartite optical square lattice". In: *Nature Phys* 7 (Dec. 2011), pp. 147–153. DOI: https://doi.org/10.1038/nphys1857. URL: https://www.nature.com/articles/nphys1857#citeas.

[74] Torben Müller et al. "State Preparation and Dynamics of Ultracold Atoms in Higher Lattice Orbitals". In: *Phys. Rev. Lett.* 99 (20 Nov. 2007), p. 200405. DOI: 10.1103/PhysRevLett.99.200405. URL: https://link.aps.org/doi/10.1103/PhysRevLett.99.200405.

[75] Xiaopeng Li and W Vincent Liu. "Physics of higher orbital bands in optical lattices: a review". In: *Reports on Progress in Physics* 79.11 (Sept. 2016), p. 116401. DOI: 10.1088/0034-4885/79/11/116401. URL: https://dx.doi.org/10.1088/0034-4885/79/11/116401.

[76] D. Hu et al. "Ramsey interferometry with trapped motional quantum states". In: *Communications Physics* 1 (29 June 2018). DOI: https://doi.org/10.1038/s42005-018-0030-7. URL: https://www.nature.com/articles/s42005-018-0030-7.

[77] S. van Frank et al. "Interferometry with non-classical motional states of a Bose–Einstein condensate". In: *Nature Communications* 5 (4009 June 2014).

DOI: https://doi.org/10.1038/ncomms5009. URL: https://www.nature.com/articles/ncomms5009.

[78] V Guarrera et al. "Microwave-dressed state-selective potentials for atom interferometry". In: *New Journal of Physics* 17.8 (Aug. 2015), p. 083022. DOI: 10.1088/1367-2630/17/8/083022. URL: https://dx.doi.org/10.1088/1367-2630/17/8/083022.

[79] Sai Vinjanampathy and Janet Anders. "Quantum thermodynamics". In: *Contemporary Physics* 57.4 (2016), pp. 545–579. DOI: 10.1080/00107514.2016.1201896. eprint: https://doi.org/10.1080/00107514.2016.1201896. URL: https://doi.org/10.1080/00107514.2016.1201896.

[80] H. T. Quan et al. "Quantum thermodynamic cycles and quantum heat engines". In: *Phys. Rev. E* 76 (3 Sept. 2007), p. 031105. DOI: 10.1103/PhysRevE.76.031105. URL: https://link.aps.org/doi/10.1103/PhysRevE.76.031105.

[81] Raam Uzdin, Amikam Levy, and Ronnie Kosloff. "Equivalence of Quantum Heat Machines, and Quantum-Thermodynamic Signatures". In: *Phys. Rev. X* 5 (3 Sept. 2015), p. 031044. DOI: 10.1103/PhysRevX.5.031044. URL: https://link.aps.org/doi/10.1103/PhysRevX.5.031044.

[82] Maxime Ben Dahan et al. "Bloch Oscillations of Atoms in an Optical Potential". In: *Phys. Rev. Lett.* 76 (24 June 1996), pp. 4508–4511. DOI: 10.1103/PhysRevLett.76.4508. URL: https://link.aps.org/doi/10.1103/PhysRevLett.76.4508.

[83] Christoph Bersch, Georgy Onishchukov, and Ulf Peschel. "Experimental observation of spectral Bloch oscillations". In: *Opt. Lett.* 34.15 (Aug. 2009), pp. 2372–2374. DOI: 10.1364/OL.34.002372. URL: https://opg.optica.org/ol/abstract.cfm?URI=ol-34-15-2372.

[84] Johannes Floß et al. "Observation of Bloch Oscillations in Molecular Rotation". In: *Phys. Rev. Lett.* 115 (20 Nov. 2015), p. 203002. DOI: 10.1103/PhysRevLett.115.203002. URL: https://link.aps.org/doi/10.1103/PhysRevLett.115.203002.

[85] Daniel Benedicto-Orenes. "Realization of a spin-1 Bose-Einstien condensation experiment". PhD thesis. 2017.

[86] Ole Mussmann. "A Versatile Atom Transport Apparatus for Photonics". PhD thesis. Sept. 2016. DOI: 10.13140/RG.2.2.26498.43208.

[87] W. Ketterle, D. S. Durfee, and D. M. Stamper-Kurn. *Making, probing and understanding Bose-Einstein condensates*. 1999. DOI: 10.48550/ARXIV.COND-MAT/9904034. URL: https://arxiv.org/abs/cond-mat/9904034.

[88] *Visual Analysis of a Texas Instruments Digital Micromirror Device*. http://www2.optics.rochester.edu/workgroups/cml/opt307/spr05/john/. Accessed: 28-11-2022.

[89] Franco Dalfovo et al. "Theory of Bose-Einstein condensation in trapped gases". In: *Rev. Mod. Phys.* 71 (3 Apr. 1999), pp. 463–512. DOI: 10.1103/RevModPhys.71.463. URL: https://link.aps.org/doi/10.1103/RevModPhys.71.463.

[90] Daniel Benedicto Orenes et al. "Exploring the thermodynamics of spin-1 Bose gases with synthetic magnetization". In: *New Journal of Physics* 21.4 (Apr. 2019), p. 043024. DOI: 10.1088/1367-2630/ab14b4. URL: https://doi.org/10.1088/1367-2630/ab14b4.

[91] Y. Deng and D. Chu. "Coherence properties of different light sources and their effect on the image sharpness and speckle of holographic displays". In: *Scientific Reports* 7 (2017), p. 5893.

[92] B. Gadway B. Sundar and K.R.A. Hazzard. "Synthetic dimensions in ultracold polar molecules". In: *Sci. Rep.* 8 (3422 Jan. 2018). DOI: https://doi.org/10.1038/s41598-018-21699-x. URL: https://www.nature.com/articles/s41598-018-21699-x.

[93] A. Celi et al. "Synthetic Gauge Fields in Synthetic Dimensions". In: *Phys. Rev. Lett.* 112 (4 Jan. 2014), p. 043001. DOI: 10.1103/PhysRevLett.112.043001. URL: https://link.aps.org/doi/10.1103/PhysRevLett.112.043001.

[94] Avik Dutt et al. "A single photonic cavity with two independent physical synthetic dimensions". In: *Science* 367.6473 (2020), pp. 59–64. DOI: 10.1126/science.aaz3071. eprint: https://www.science.org/doi/pdf/10.1126/science.aaz3071. URL: https://www.science.org/doi/abs/10.1126/science.aaz3071.

[95] A. Balˇcytis et al. "synthetic dimension band structures on a Si CMOS photonic platform". In: *arXiv:2105.13742* (May 2021). DOI: 10.1038/s41586-019-0943-7. URL: https://doi.org/10.1038/s41586-019-0943-7.

[96] H. Chen et al. "Real-time observation of frequency Bloch oscillations with fibre loop modulation." In: *Light Sci. App.* 10 (48 May 2021). DOI: https://doi.org/10.1038/s41377-021-00494-w. URL: https://www.nature.com/articles/s41377-021-00494-w.

[97] Daniel Benedicto Orenes et al. "Exploring the thermodynamics of spin-1 Bose gases with synthetic magnetization". In: *New Journal of Physics* 21.4 (Apr. 2019), p. 043024. DOI: 10.1088/1367-2630/ab14b4. URL: https://dx.doi.org/10.1088/1367-2630/ab14b4.

[98] Aaron Smith et al. "Generation of optical potentials for ultracold atoms using a superluminescent diode". In: *Phys. Rev. Research* 3 (3 Sept. 2021), p. 033241.

DOI: 10.1103/PhysRevResearch.3.033241. URL: https://link.aps.org/doi/10.1103/PhysRevResearch.3.033241.

[99] Tomasz Karpiuk et al. "Superfluid fountain effect in a Bose-Einstein condensate". In: *Phys. Rev. A* 86 (3 Sept. 2012), p. 033619. DOI: 10.1103/PhysRevA.86.033619. URL: https://link.aps.org/doi/10.1103/PhysRevA.86.033619.

[100] M. A. Alpar, S. A. Langer, and J. A. Sauls. "Rapid postglitch spin-up of the superfluid core in pulsars." In: 282 (July 1984), pp. 533–541. DOI: 10.1086/162232.

[101] Jacopo Nespolo, Grigori E Astrakharchik, and Alessio Recati. "Andreev–Bashkin effect in superfluid cold gases mixtures". In: *New Journal of Physics* 19.12 (Dec. 2017), p. 125005. DOI: 10.1088/1367-2630/aa93a0. URL: https://dx.doi.org/10.1088/1367-2630/aa93a0.

[102] Victor I. Kolobov et al. "Observation of stationary spontaneous Hawking radiation and the time evolution of an analogue black hole". In: *Nature Physics* 17.3 (Jan. 2021), pp. 362–367. DOI: 10.1038/s41567-020-01076-0. URL: https://doi.org/10.1038%2Fs41567-020-01076-0.